The Dissertation Committee for Gregory William Doppmann
Certifies that this is the approved version of the following dissertation:

Measuring Physical Properties of Pre–Main Sequence Stars Using High Resolution Infrared Spectroscopy

Committee:

Dan Jaffe, Supervisor

Neal J. Evans

John H. Lacy

Christopher Sneden

Elizabeth A. Lada

Christopher M. Johns-Krull

Measuring Physical Properties of Pre–Main Sequence Stars Using High Resolution Infrared Spectroscopy

by

Gregory William Doppmann, B.A., M.A.

DISSERTATION
Presented to the Faculty of the Graduate School of
The University of Texas at Austin
in Partial Fulfillment
of the Requirements
for the Degree of

DOCTOR OF PHILOSOPHY

THE UNIVERSITY OF TEXAS AT AUSTIN
August 2002

Dedicated to my father, William G. Doppmann.

Acknowledgments

It is a pleasure to thank my advisor, Dan Jaffe, who had faith in my abilities, and gave me important responsibilities that were key to my growth as a scientist, observer, and instrument builder. I am grateful to John Lacy for numerous discussions (especially while cycling along the backroads of Central Texas) about infrared instruments and their quirks. I also thank Chris Sneden for his advice and support in adapting MOOG for use with young stellar objects, Tom Greene for providing us with his data on MK standards, Ken Hinkle for help with our Phoenix observations, and Carlos Allende-Prieto, Russel White, and Chris Sneden for helpful comments.

It has been a thoroughly rewarding experience working with the mountain staff at McDonald Observatory during numerous NIRSHELL and Dizzy runs. The are many folks who gave generously of their time who have become a second family away from Austin. Dave Doss was exceptionally helpful in getting me up to speed with all the subtle details involved in installing the instruments I designed and improved for the 2.7-meter throughout my tenure as a graduate student. I'll truely miss his stories and warm hearted way.

It is a great pleasure to thank Russel White for his help and support especially during numerous Nirshell runs, pushing the limits like never before at McDonald Observatory. I am rewarded by his friendship and look forward to more scientific collaborations with him in the future.

I thank Chris Johns-Krull who was able to join the committee on short notice.

Measuring Physical Properties of Pre–Main Sequence Stars Using High Resolution Infrared Spectroscopy

Publication No. ____________________

Gregory William Doppmann, Ph.D.
The University of Texas at Austin, 2002

Supervisor: Dan Jaffe

Physical properties of pre–main sequence stars and their disks are measured from high resolution near–infrared spectra. A new fitting technique using spectral synthesis models has been developed to find the best fit to fully resolved K band absorption lines, allowing measurements of the stellar effective temperature, rate of rotation, and amount of non–stellar continuum excess from infrared emission by the circumstellar disk. An IDL fitting routine selects the best spectral synthesis model by the RMS minimum to the residuals of the fits, and has been validated by observations of MK standards. This new technique has been applied to a sample of pre–main sequence stars in the ρ Ophiuchi dark cloud to obtain accurate effective temperatures, continuum veilings, and some of the first measurements of $v \sin i$ rotations in highly extincted young stars from 2.2 μm spectra. In two sources, a new spectroscopic technique to measure surface gravity has been applied using line

flux ratios in high resolution spectra at 2.2 μm and 2.3 μm, leading to the first luminosity measurements that are independent of extinction and only weakly dependent on continuum excess. Previous assumptions of no continuum excess at J (1.2 μm) upon which the photometrically determined luminosities are based, are called into question with these new results. In the absence of strong magnetic fields, the ages of these objects inferred from stellar evolutionary model tracks on the HR diagram reveals an older age (6–9 Myr) from spectroscopically determined luminosities than from the photometry of the same objects.

Another useful application of high resolution spectroscopy is the detection of binary systems. Characterization of binary systems offers a direct way to obtain mass and relative mass information. With a sensitivity down to $\sim$0.5 km s^{-1}, we have measured precision radial velocities of the sources in our Ophiuchus sample, resulting in the discovery of one short period ($P < 1$ yr) pre–main sequence binary (GSS29). This system has been subsequently monitored to determine its orbital characteristics (P = 145 d, v_2 = 29 km s^{-1}) and constrain the mass ($M_1 + M_2 \sim 1.8$ $M_\odot$). We find the dominant spectral line component to be the less massive (and cooler) star. The more massive star is mostly featureless because it is hotter and rotating fast. More observations are required to better constrain these preliminary results.

Table of Contents

List of Tables

List of Figures

Chapter 1

Introduction

1.1 Infrared Advantage in Observations of Young Stars

Our understanding of how stars form has been greatly aided by the technological advances of near–infrared imaging on telescopes. Increases in the sensitivity and size of infrared detector arrays have allowed us to see through more obscuring dust and gas to be able to make observations of young stars still enshrouded within their natal clouds. While observations in the optical have been made of less extinguished young stellar objects (YSOs) (i.e. T–Tauri stars) in regions of Taurus–Auriga (Kenyon & Hartmann 1995; Herbst et al. 1994; Herbig & Goodrich 1986; Cohen & Kuhi 1979), and the extended region of ρ Ophiuchi (Wilking et al. 1987; Dolidze & Arakelyan 1959; Struve & Rudkjøbing 1949; Haro 1949), the stars within the cores of these and other star forming regions (SFRs) remain hidden to us except at longer wavelengths (i.e. the infrared and submillimeter). These cores harbor numerous young stars and are sites of on–going star formation, highlighting their importance to our understanding of the star formation process. Pioneering imaging surveys in the near–IR of the nearby embedded cluster core, ρ Ophiuchi, have resulted in hundreds of cataloged young stellar objects (YSOs), (Grasdalen et al. 1973; Vrba et al. 1975; Elias 1978a; Wilking & Lada 1983; Wilking et al. 1989; Barsony et al. 1989; Rieke et al. 1989; Greene & Young 1992; Comeron et al. 1993;

Strom et al. 1995; Barsony et al. 1997; Allen et al. 2002).

1.2 IR Spectroscopy

With continuing improvements in the performance of IR detectors, spectroscopic techniques developed to measure stellar properties in the optical have now been extended to the infrared. For example, spectral typing in the near–IR is now feasible through an analysis of absorption lines from neutral atomic species and molecular bands present in the photospheres of cooler stars (Kleinmann & Hall 1986). For our near–infrared study of the properties of pre–main sequence (PMS) stars, we have chosen a particular wavelength region in the K band at 2.200–2.210 μm that is rich with photospheric lines from which to measure PMS stellar properties.

With infrared photometry and low resolution spectroscopy, measurements of the luminosities and temperatures of PMS stars have been made (Greene & Meyer 1995; Luhman & Rieke 1999). Uncertainties in the amount of extinction and non–stellar continuum emission (veiling) by a warm circumstellar disk has made the placement of these objects on the Hertzsprung–Russell diagram uncertain. A number of near–IR spectroscopic surveys at low resolution (R = 300–1200) have been carried out over the last decade to measure spectral types, luminosities, and continuum veilings of PMS stars with limited success (Casali & Matthews 1992; Greene & Meyer 1995; Greene & Lada 1996; Luhman & Rieke 1998; Luhman et al. 1998; Luhman & Rieke 1999), but uncertainties in these derived physical properties remain large due to unresolved photospheric lines and to problems with the photometrically derived luminosities.

1.2.1 High Resolution Spectroscopy

High resolution infrared spectroscopy offers a better way to measure stellar properties by making use of the information encoded in the intrinsic *shapes* of photospheric lines. Fully resolved absorption lines originating in the PMS stellar photosphere can contain detailed information about the star's effective temperature, surface gravity, rate of rotation, precise radial velocity, magnetic field strength, as well as the amount of continuum emission due to the presence of a warm circumstellar disk. The presence of extinction does not affect either the shapes or equivalent widths of these lines. Continuum emission alters only the equivalent widths of the lines while the shapes are preserved. A detailed quantitative analysis using the depths and shapes of photospheric absorption lines to measure physical properties in stellar spectra has been developed in this dissertation and applied to PMS stars to characterize their stellar properties.

In chapter 2, I describe a new spectroscopic technique that I've developed for the analysis of physical parameters in stars based on high resolution ($\lambda/\Delta\lambda \geq 15,000$) near–infrared (2.0–2.4 μm) spectra. Initially, a grid of spectral synthesis models is generated by `MOOG` (Sneden 1973) based on NextGen stellar atmospheres (Hauschildt et al. 1999). Using the interactive data language (IDL) I have developed a fitting routine that alters the original synthesis grid (based on effective temperature and surface gravity) to account for changes caused by stellar rotation, continuum veiling, and radial velocity shifts. The IDL routine selects the best model fit by the minimum RMS of the residuals over selected wavelength intervals where there is line flux from the stellar photosphere. This technique has been validated by its successful application to observations of late spectral type MK standard stars.

1.3 Measuring PMS Luminosities

Photometrically determined luminosities are extremely problematic in SFRs where there is variable extinction and where many stars have non–stellar continuum flux. It is often assumed that excess emission at near–infrared wavelengths is negligible in the J and H bands (Luhman & Rieke 1999; Greene & Meyer 1995). By estimating the effective temperature from spectroscopy, and adopting intrinsic dwarf colors, the amount of reddening becomes simply the difference between the observed and intrinsic colors. Using an extinction power law (e.g. Martin & Whittet 1990), and knowing the amount of reddening, the extinction at J (A_J) is computed and applied to the photometry which is then converted to a bolometric flux. However, if there is excess emission at J, then the derived luminosities will be systematically too high.

I present a new spectroscopic technique for determining surface gravities in stars based on the ratio of line flux from two absorption line regions in the K band (appendix A).

1.4 Spectral Energy Distributions of PMS stars

The shape of the spectral energy distribution (SED) in the infrared has been used to probe the nature and distribution of the material surrounding YSOs (Wilking et al. 1994). Current theoretical evolutionary scenarios describing protostellar collapse and circumstellar disk evolution (Adams & Shu 1986), are placed the context of SED morphology by Adams, Lada, & Shu (1987). They define a spectral index, $n \equiv d\log(\nu F_\nu)/d\log\nu$, which links the SED slope to a specific stage (Class 0–III) of YSO evolution in the following way: Steeply rising SEDs that peak in the far infrared or submillimeter are associated with the earlier stages of protostellar evolution, where nebular material is infalling onto the YSO ($n < 0$; Class 0 or I). Flat or decreasing SEDs which peak in the optical or near infrared represent more evolved YSOs that have stellar photospheres which dominate the spectrum ($n > 0$; Class II or III).

Linking the SEDs of PMS stars to their derived stellar properties is an important step toward understanding the physical stages young stars move through as they evolve toward the main sequence. The more accurate measurements of PMS stellar properties and continuum veiling in this dissertation contribute to our understanding of how young stars and their disks evolve.

In chapter 3, I apply my spectral synthesis fitting routine to a sample of PMS stars in the ρ Ophiuchi dark cloud to measure stellar effective temperatures, $v\sin i$ rotations and continuum veiling by circumstellar disk emission. I derive luminosities for all the sources using the photometric method described above. For two sources, I have high resolution spectra at both 2.2 and 2.3 μm enabling me to determine their luminosities spectroscopically using stellar evolutionary models to convert from derived surface gravities. A comparison of luminosities determined by spectroscopy with photometrically derived luminosities in two sources shows evidence of significant J band continuum emission that is unaccounted for by the photometric technique.

1.5 Rotation of PMS stars

Only a few studies at high resolution ($R \geq 17,000$) have begun to address $v \sin i$ rotation in YSOs by analysis of fully resolved photospheric lines (Casali & Matthews 1992; Greene & Lada 1997, 2000; **?**). These high resolution studies suggest that flat spectrum protostars in ρ Ophiuchi rotate more rapidly ($v \sin i \sim 26$ km s^{-1}) than Class II sources ($v \sin i \simeq 12$ km s^{-1}) (Greene & Lada 1997, 2000). ASCA satellite measurements of YSOS in Ophiuchus have permitted detection of rotational velocities of embedded sources (Class I) from the modulation of flaring in the observed X–ray flux. From these observations, Montmerle et al. (2000) find IRS43 to be rapidly rotating at near breakup velocities ($P = 20$ hours), while WL 6 rotates with a much longer period ($P = 3$ days; $v \sin i = 40$ km s^{-1} for $0.5 M_{\odot}$ star on the birth–line) consistent with findings by Greene & Lada (2000). They suggest that the braking times are relatively short ($\sim 10^5$ yrs) and are due to dynamo generated torques upon the infalling accreting material. They conclude that stars may be able to spin down while still within the embedded class I stage. They assert that mass plays an important role on when the rotation begins to couple to the disk, implying that fast rotators (IRS 43) are less evolved and more massive than slower ones (WL 6) within the class I embedded phase. With our high resolution observations of Class II protostars, we are able to determine $v \sin i$ for a modest sample. These results can add to the current picture of the evolution of stellar rotation as stars descend toward the main sequence.

1.5.1 PMS Binaries

In Chapter 4, I describe the importance of binary systems to our understanding of PMS stellar evolution. Since direct mass measurements of PMS stars are important to validating theoretical evolutionary model tracks, I have conducted a search for binary systems in Ophiuchus using precision (< 1 km s^{-1}) radial velocity measurements from high resolution spectra at 2.2 μm. Given the likelihood that PMS stars have orbital companions ($\geq 50\%$ are multiples), and the low velocity dispersion of the stars in the ρ Ophiuchus dark cloud (< 2 km s^{-1}), it is not surprising that we have detected a binary system (GSS29) in our sample during the first epoch. Through subsequent observations at later epochs, I have determined the period of the system and the velocity amplitude of the dominant spectral component in GSS29, and have been able to set constraints on the mass from Kepler's 3rd Law. Using two component spectral synthesis models ranging in temperature and $v \sin i$ for each component, I have found a preliminary best fit for both spectral components that is consistant with the mass limits derived from the orbital properties and loosely agrees with the observed spectra in the different epochs. In order to characterize the almost featureless 2nd component, more observations are needed at high S/N an epoch where the two components are well separated.

1.5.2 Pre–Main Sequence IMF

Measurements of stellar mass inside star forming regions can set direct constraints on the initial mass function (IMF). The product of cloud fragmentation and the efficiency with which star formation converts material into stars is fundamental to our picture of how stars form. With direct measurements of PMS stellar masses from characterization of binary systems, we can begin to sample the mass distribution of newly formed stars in clusters and start to address the details of how clouds fragment and form stars.

Chapter 2

A Spectroscopic Technique for Measuring Stellar Properties of Pre–Main Sequence Stars

2.1 Introduction

Our understanding of main sequence and post main sequence stellar evolution is a triumph of collaboration between theorists building physical models and observers making precise observations. For young stellar objects (YSOs), however, the link between theory and observation is much more tenuous. Comparison of model tracks with observational HR diagrams has been possible for visible T–Tauri stars (White et al. 1999; Webb et al. 1999; White & Ghez 2001), but much more difficult for YSOs heavily extincted by their natal clouds. The difficulties involved in comparing the tracks with observations leave our understanding of the physics of YSOs much less solid than our understanding of more evolved objects.

In studying YSOs, our main goal is to understand the history of these objects from their formation to their arrival on the main sequence. We also wish to use the ensemble of such objects to characterize forming clusters and associations, their initial mass functions and star formation histories. To meet these goals, we need to determine parameters of the stars and relate them to other properties of protostellar disks and of the surrounding cloud. The most important stellar parameters to obtain are the effective temperature and the luminosity or surface gravity since this pair permits us to place the YSOs into a theoretical Hertzsprung–Russell diagram for comparison with theoretical pre–main sequence (PMS) evolution models. Other useful parameters include the amount of reddening or extinction, the amount of non–photospheric emission as a function of wavelength, and the stellar rotation rate.

Observers have used a wide range of approaches to investigate the nature of stellar sources in very young embedded clusters. In well–studied regions like the ρ Oph core, previous investigators have used photometric surveys in the near–IR (Wilking & Lada 1983; Greene & Young 1992; Barsony et al. 1997), and low to moderate resolution ($R = \lambda/\Delta\lambda$ =500–1000) near–IR spectroscopy to estimate temperatures, luminosities, and amount of excess infrared emission for the sources (Greene & Lada 1996; Greene & Meyer 1995; Luhman & Rieke 1999; Kenyon et al. 1998; Casali & Matthews 1992; Greene & Lada 2000, 1997; Bontemps et al. 2001). These techniques are particularly powerful for studies of clusters because of their efficient use of observing time. In embedded clusters, however, photometry and low resolution spectroscopy suffer under a number of disadvantages not inflicted upon these techniques when applied to main sequence stars or to less heavily extincted young stars. Problems include extremely high extinction (e.g. the central part of the ρ Ophiuchi molecular cloud where $A_{\mathrm{v}} = 40 \pm 10.9$ magnitudes, Luhman & Rieke 1999), and excess emission in the UV/blue (presumably from accretion shocks, Gullbring et al. 2000) and in the near and mid–IR (from warm dust in the circumstellar disks, Strom et al. 1995; Greene et al. 1994).

Spectroscopy of young stars in the near–IR has advantages over measurements made at optical wavelengths. Young stars are brighter in the infrared because it is easier for the stellar infrared emission to penetrate through the dust within the star forming cloud or along the line–of–sight. Also, the photospheric flux relative to the UV excess is higher in the infrared than at shorter wavelengths, permitting better detections of photospheric lines (i.e. Na, Si, & Sc at 2.2 μm) that are diagnostic of effective temperature, surface gravity, and stellar rotation.

At present, there is no well–developed scheme from near–IR spectra that allows precise measurements of effective temperatures or surface gravities that goes beyond simple arguments that the sources lie between giants and dwarfs. The twin problems of reddening and excess emission make comparison of line strengths or equivalent widths across any sizable range of wavelengths extremely problematic.

We present here a technique for deriving some of the properties of PMS stars from high resolution near–IR spectra. High resolution spectra are particularly useful because the closely spaced lines in late–type stars are observable separately and because it is possible to use the spectra to glean information from the shapes of the absorption lines. The stellar parameters we derive include the effective temperature ($T_{\rm eff}$), the surface gravity ($\log g$), the rotation rate ($v \sin i$), and the amount stellar/circumstellar emission in excess of the photospheric emission (r_λ). The method is largely independent of photometric data and offers the promise of improved accuracy.

Stars in the mass range from 0.1 to 0.9 $M_\odot$ will lie within the spectral type range from M6 to G5 from the time they become visible in the near–IR until they reach the main sequence (Siess et al. 2000; Palla & Stahler 1999; Baraffe et al. 1998). For such late–type stars, the near–IR spectra are rich in lines of neutral metals and hardy molecules. It is worth asking whether analysis of high resolution spectra from a limited spectral range in the near–infrared can provide sufficient information to permit us to derive many of the important physical properties of the stars.

We present a first attempt at a quantitative approach to the problem of deriving physical properties of PMS stars from high resolution spectra taken in the K–band (2.0–2.4 μm). We compare synthetic spectrum calculations to observed high resolution spectra. In §2.2, we describe the basic spectral analysis technique with particular emphasis on the features of our method necessary to deal with the peculiarities of pre–main sequence objects. In §2.3, we analyze the internal errors and investigate inherent systematic uncertainties. We compare results for standard stars from optical spectroscopy to the results we obtain through the analysis of high resolution near–IR spectra, in §2.4, and discuss the ways in which our derived properties supplement or improve upon properties measured with other techniques.

2.2 Method

Ideally, we would like to be able to derive stellar parameters across the whole range of masses and ages present in clusters or associations of newly forming stars. The actual range of surface gravities and effective temperatures for which we can derive parameters from high resolution spectroscopic observations is constrained by both observations and theory. On the observational side, we are limited to objects that are evolved enough to permit near–IR radiation from the stellar photosphere to escape through the surrounding disk and envelope. In general, photometric studies of YSOs imply that the lowest surface gravities for which objects become visible in the near–IR are $\log g \lesssim 3.0$ (Comeron et al. 1993; Siess et al. 2000). On the theoretical side, our technique requires that the stellar photospheres have a sufficient number of reasonably strong lines and that these lines be sensitive to variations in temperature and surface gravity. Further, it requires that the stellar models and available line lists be adequate to permit us to make accurate high resolution spectral syntheses for comparison with the observed spectra. With the stellar atmospheres and synthesis program we are using, our analysis technique works well within the range $3000 \leq T_{\rm eff} \leq 5800$ K, and $3.5 \leq \log g \leq 5.5$. Since HR diagram evolutionary tracks for PMS objects are largely vertical, the temperature constraint implies a range of masses for which we can position objects in the HR diagram of 0.1 to 1.6 $M_{\odot}$

Technique Overview

The basis for our technique is a grid of synthetic high resolution spectra in the K window (2.0–2.4 μm). The grid spans the relevant ranges of the important stellar parameters for YSOs: $T_{\rm eff}$, surface gravity, veiling, and $v\sin i$ rotation. The best model fit is chosen by an RMS minimization of the residuals across the photospheric absorption lines in our spectral window.

The 2.0–2.4 μm atmospheric window contains features that are sensitive to both the temperature and pressure in the stellar photosphere. It is also the longest wavelength band where the photospheric emission from the youngest stars is comparable in flux to the thermal emission from dust in the circumstellar disk. At the same time, the dust is considerably more transparent at K than at shorter infrared wavelengths and the sensitivity of ground–based spectrometers with large resolving powers is not yet compromised by thermal emission from the telescope and sky. This wavelength band is also well–matched to the maximum in the photospheric emission from late–type stars.

For the purposes of our spectral matching program, high spectral resolution means sufficient resolution to permit us to resolve most stellar lines (resolving powers $R = (\lambda/\Delta\lambda) \geq 20,000$). No existing high resolution spectrometer covers the entire 2.0–2.4 μm atmospheric window with a single exposure. The instrument with the most coverage (Nirspec, McLean et al. 1995) gives cross–dispersed spectra covering about 1/3 of the window in disconnected segments. Other existing instruments cover only individual 50–200 Angstrom bands (PHOENIX, Hinkle et al. 1998), (CSHELL, Greene et al. 1993), (CGS4, Mountain et al. 1990; Wright et al. 1993). In order to be generally applicable without enormous expenditure of telescope time, our technique should therefore use only a limited part of the spectrum available within the atmospheric window.

We have used spectral synthesis models to explore the K window to find the spectral intervals that have strong lines that vary significantly with variations in the stellar parameters. Based on this investigation, we chose the region at 2.207±0.0015 μm (hereafter “the Na interval”) which includes two strong neutral sodium lines ($4s^2S_{1/2}$–$4p^2P^0_{3/2}$), and several prominent lines of neutral Si and Sc (the upper spectrum in

Figure 2.1) and the region at 2.2935 μm where the dominant feature is the 2–0 bandhead of ^{12}CO (“the ^{12}CO interval”, (the lower spectrum in Figure 2.1) for our analysis. Figure 2.2 presents a sequence of spectral syntheses for the Na interval that illustrates the sensitivity of the line ratios and line shapes in this wavelength band to the photospheric temperature.

We produced a grid of spectra covering the appropriate range in $T_{\rm eff}$ and $\log g$ using the NextGen non–grey atmosphere models (Hauschildt et al. 1999). These models include TiO and H_2O opacities, critical for cooler atmospheres. We synthesized a high resolution ($R = 120,000$) K band spectrum at 2.2 μm and 2.3 μm using the `MOOG` spectral synthesis code (Sneden 1973). Atomic and CO line lists came from Kurucz (1994) and Goorvitch & Chackerian (1994), respectively. We have computed all models with solar metallicity. The critical relative abundance in our analysis is [Sc/Si]. Stellar abundances of [Si/Fe] in the local neighborhood are solar (Edvardsson et al. 1993), and we assume the same for [Sc/Fe].

The strongest spectral features at 2.2 μm are the Na lines over the range of surface gravities we have available from the models ($\log g = 3.5 - 5.5$). At cooler temperatures (i.e. $T_{\rm eff} < 4000$K), the wings of these lines are noticeably pressure broadened due to collisions of the emitters with neighboring particles. The synthesis code, `MOOG`, allows for the van der Waals damping parameter to be easily adjusted in creating the artificial spectra. We have tuned the amount of damping present in the Na lines to give the best fit to an observed spectrum of the sun (Livingston & Wallace 1991). The best fit was the “Unsold approximation.” The wings of the Na lines at low temperatures change by less than 4% with changes in the

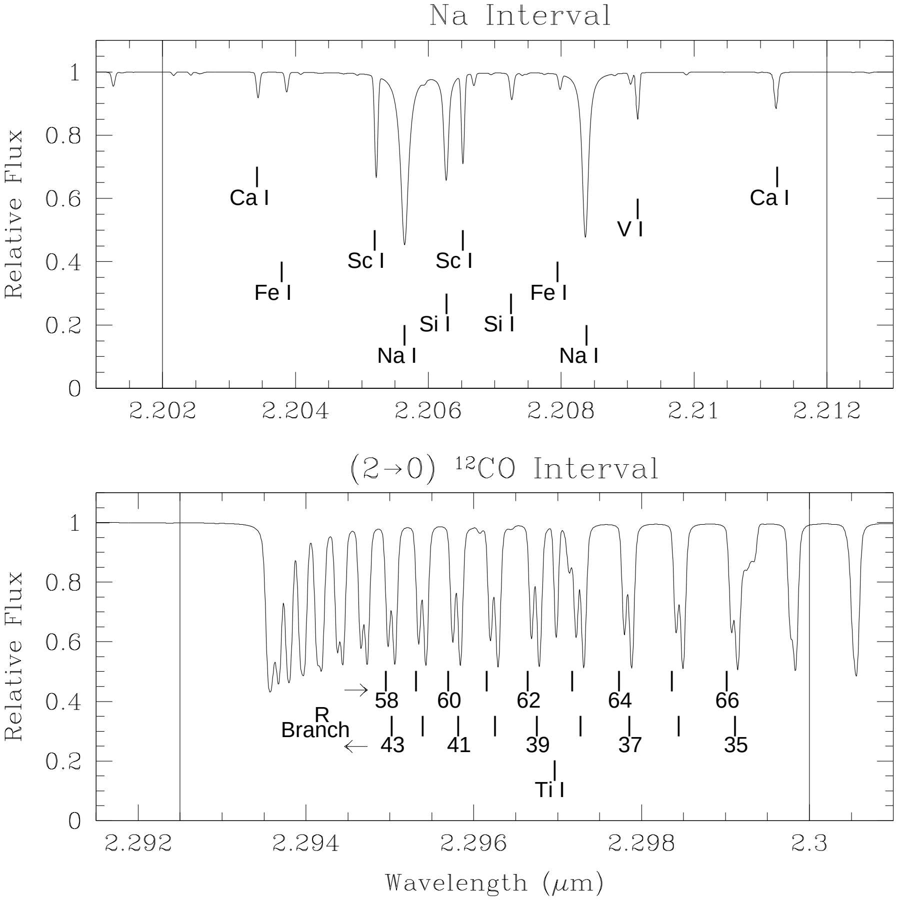

Figure 2.1 The intervals within the 2.0–2.4 μm K window used for spectral synthesis analysis of high resolution data. The spectra are from a synthesis of a $T_{\rm eff} = 4000$ K, $\log g = 3.5$ NextGen atmosphere model assuming a resolving power $\lambda/\Delta\lambda = 50,000$. The intensity is normalized to the photospheric continuum. (a) The Na interval is defined as 2.202–2.212 μm (b) The ^{12}CO interval is defined as 2.2925–2.3000 μm. The numbers below the spectra refer to $J_{\rm lower}$ for the different $v = 2$–0 transitions of ^{12}CO. The vertical lines show the boundaries for the intervals used to compute the equivalent width ratios plotted in Figure 2.5.

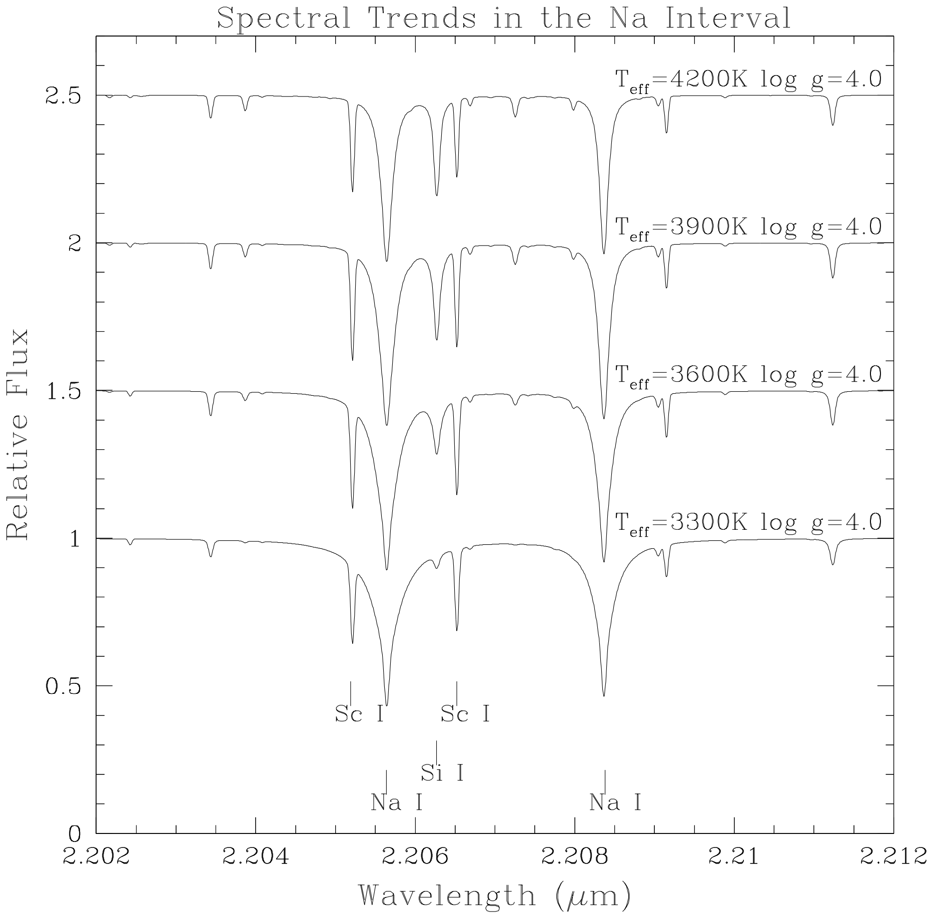

Figure 2.2 A grid of Moog spectral syntheses based on NextGen atmosphere models. These spectra illustrate the change in Na line shape and depth and the variations in Si/Sc across 3300 K–4200 K for log *g* fixed at 4.0

Unsold approximation of order a factor of 6.3.

We also wish to derive the rotation rate ($v \sin i$), and the amount of excess (non–photospheric or "veiling") emission at the wavelength where we observe. $r_{\rm Na} = (F_{\rm source} - F_{\rm phot})/F_{\rm phot}$, where $F_{\rm source}$ and $F_{\rm phot}$ are the observed flux and the photospheric flux, respectively. Therefore, we extend the grid of synthetic spectra into a hypercube containing all four parameters. We added rotation to the spectra by convolving a semi–circle function with a base twice the model $v \sin i$ rotation value that was modified by a limb darkening coefficient of 0.6 and normalized to conserve flux (Gray 1992, the standard Gray rotation profile,). The intensity of the non–photospheric emission over the individual narrow spectral intervals has at most a slope of a few percent so we can treat it with a single parameter. In the presence of such an excess, resolved lines have lower equivalent widths but retain the shapes imparted to them by line transfer in the stellar atmosphere and by rotation. We have taken the original grid of `MOOG` synthetic spectra and created our hypercube by adding rotation to them at rates ranging from $v \sin i = 1$ to 40 km $\rm s^{-1}$ and an excess $r_{\rm Na}$ ranging from 0 to 8.

2.2.1 Previous Derivations of Stellar Parameters in the Near–IR

Observers recognized long ago that spectral classification in the near–IR was a potentially valuable tool for deriving the properties of obscured stars in the Galactic Plane and young stars obscured by their natal clouds (Merrill & Ridgway 1979). The strength of the CO overtone bands at 2.3 μm was recognized early–on as a useful indicator of luminosity, albeit with additional sensitivity to temperature

(Baldwin et al. 1973; Kleinmann & Hall 1986; Lancon & Rocca-Volmerange 1992). Ramirez et al. (1997) find that an index formed from the equivalent widths of the strong near–IR lines of neutral calcium and sodium and the CO 2–0 bandhead is a good luminosity indicator, independent of temperature, for giants in the range K0 to M6.

Accurate estimates of spectral type are also possible from near–IR spectra. Kleinmann & Hall (1986) calculated equivalent widths of key features from their K–band spectra of MK standards and derived the dependence of these equivalent widths on $T_{\rm eff}$ and luminosity class. Meyer et al. (1998) derived line ratio relations from H band spectra of MK standards and found that the relations predicted spectral type correctly to within ± 2 subclasses. They argue that using line ratios makes the $T_{\rm eff}$ determination less sensitive to the presence of continuum excesses in PMS objects. While most of the efforts to derive spectral type from the IR spectra have focused on empirical equivalent width–$T_{\rm eff}$ relations, there have also been a number of efforts to match low resolution H and K band spectra to synthetic spectra (Kirkpatrick et al. 1993; Ali et al. 1995; Leggett et al. 1996). Ali et al. (1995) find that they can match the temperatures of dwarfs with an error of ± 350 K using this technique.

All of the studies we have described so far were carried out with resolving powers ≤ 3000, where the unsaturated photospheric features are unresolved. At these resolving powers, not only can the equivalent widths of the lines get quite small in the presence of excess continuum emission but there can also be problems due to line blending. Many of these studies use the equivalent width of the Na features at 2.2 μm in the determination of spectral type and luminosity class. At $R = 1,000$, the typical resolving power for the studies, however, the Na lines are blended with weaker but significant lines of Sc and Si that have very different dependences on $T_{\rm eff}$ and $\log g$. Existing spectra of the Na interval at greater resolving power have shown that the relative strengths of the Sc, Si, and Na lines plus the shape of the Na features could potentially be sensitive indicators of effective temperature for dwarfs (Wallace & Hinkle 1996; Greene & Lada 1997).

2.2.2 Actual technique

The way we proceed depends on the data available. With data from the Na interval alone, it is possible to determine rotation velocity and veiling and to obtain a quite well constrained measure of the stellar effective temperature that is independent of any stellar photometry. With the addition of observations of the ^{12}CO interval, it is possible to further improve the precision of the $T_{\rm eff}$ determination and to determine the surface gravity of the emitting star, even in the presence of significant veiling and reddening.

Obtaining $T_{\rm eff}$, $v \sin i$, and $r_{\rm Na}$ from the Na Interval Alone

The interval around the 2.2 μm sodium lines is particularly rich in diagnostic power. Since it is often possible to obtain high resolution spectra of a single band, we first discuss the derivation of stellar parameters from the Na interval alone. In the section following this one, we will explain how the availability of ^{12}CO interval spectra can refine the results.

We begin the spectral matching for the Na interval by using pattern recognition to constrain the effective temperature to a 1000 K range. For YSOs, we fix the value of $\log g$ =3.5–4.0, which corresponds to $\sim$1–2 Myr old objects in stellar evolutionary models (Baraffe et al. 1998; Siess et al. 2000; Palla & Stahler 2000), consistant with age estimates of the central embedded cluster in Ophiuchus (Wilking et al. 1989; Greene & Meyer 1995; Luhman & Rieke 1999; Bontemps et al. 2001). §2.3.2 below describes in detail how the choice of a particular value of $\log g$ affects the T_{eff} determination and how to correct T_{eff} should $\log g$ have a different value.

Once we have the grid of spectral syntheses in place, we need to choose spectral subintervals over which to compare the spectra synthesized from the atmosphere models to the observed spectra. Based on our experience with both MK standards and YSOs, we restrict the subintervals to the regions within the observed spectra where there is measurable line flux. The actual size of the intervals varies with the amount of broadening caused by stellar rotation or by damping of the line wings.

The next step is to take the continuum normalized observed spectrum and compare it to each synthesized model spectrum calculating the RMS difference over the subintervals chosen in the previous step. Figure 2.3 illustrates this process by showing an artificial noisy spectrum and how the differences between this spectrum and the noiseless synthetic spectra vary as the search routine steps through the correct value of T_{eff}. We then find the location of the minimum RMS difference on the parameter–space hypersurface by interpolation.

Figure 2.4 shows the principal sections through the RMS errorspace of the best fits for an artificial noisy spectrum with synthesis models as a function of the search parameters, showing the shape of the minimum in the $T_{\rm eff} - v \sin i$ plane, in the $T_{\rm eff}$–$r_{\rm Na}$ plane, and in the $T_{\rm eff}$–$\log g$ plane. In all three planes, there are well–determined minima in the fits to the spectrum of the Na interval for all variables except $\log g$. The minimum in the $T_{\rm eff} - \log g$ plane is very shallow. It is the one plane where we do not usually recover the input model. The grid in the $\log g$ direction is fairly coarse ($\Delta \log g = 0.5$) and some noise seeds for the artificial spectrum at $\log g = 4.0$ even find the lowest RMS value at the edge of the grid, at $\log g = 3.5$ leaving the exact location of the minimum uncertain. This cut illustrates that an incorrect guess of $\log g$ for real target spectra can lead to systematic errors in the derived value of $T_{\rm eff}$ (see § 2.3.2)

Solving Simultaneously for $T_{\rm eff}$ and $\log g$

There is a strong inverse dependence of the ^{12}CO 2–0 bandhead equivalent width on $\log g$. There is also a weaker but noticeable scaling of the line equivalent width for the Na interval with $\log g$. Figure 2.5 plots the ratio of ^{12}CO 2–0 to Na interval photospheric equivalent width as a function of $T_{\rm eff}$ for $\log g$ values ranging from 3.5 to 5.0. We derived this ratio from the NextGen photospheric models by creating synthetic spectra for the relevant intervals and calculating the equivalent widths over the bands marked in Figure 2.1. For $T_{\rm eff} >$3700 K, the ratio varies strongly with $\log g$ and is almost independent of temperature. For lower temperatures, the ratio still varies strongly with $\log g$ but $T_{\rm eff}$ must also be known fairly

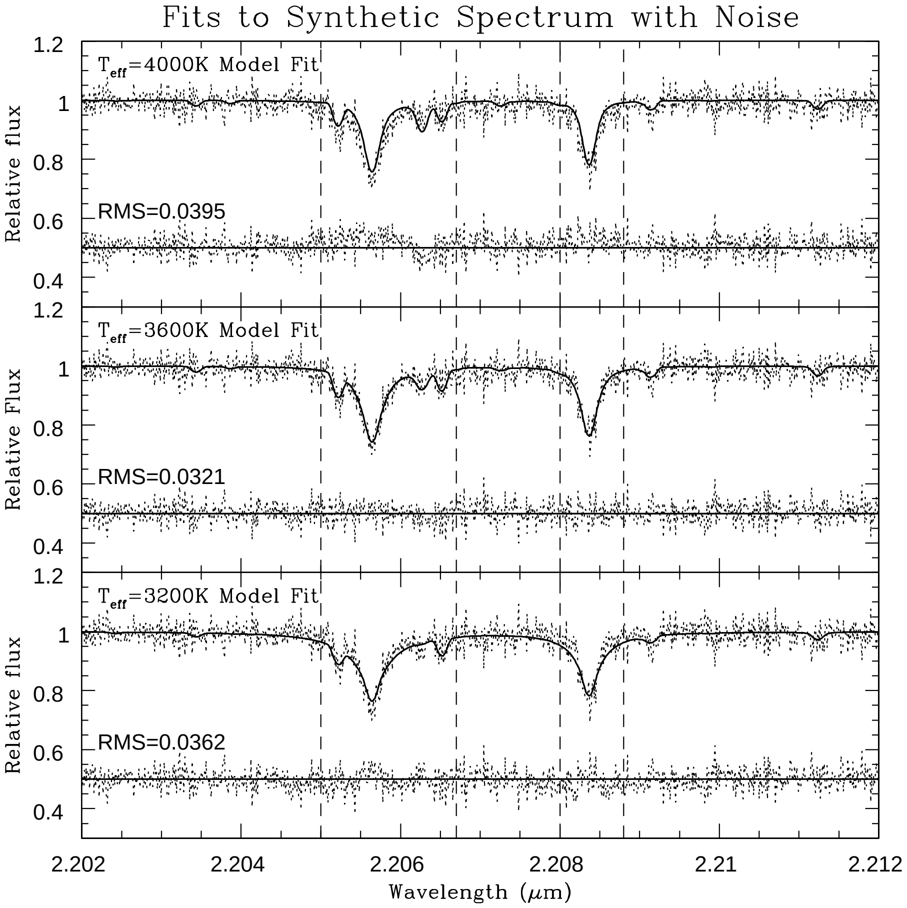

Figure 2.3 Fits to a noisy artificial spectrum of the Na interval. The light dotted line shows an artificial spectrum for $T_{\rm eff} = 3600$ K, $\log g = 4.0$, $v \sin i = 15$ km s^{-1}, and $r_{Na} = 1.0$. We have smoothed this spectrum to $R = 50,000$ and added Gaussian random noise to the spectrum to produce a $S/N = 30$ (per pixel with $R = 240,000$ pixels). Overlaid on each of the 3 panels is a noiseless synthetic spectrum (bold lines) for $\log g = 4.0$, $T_{\rm eff} = 4000$ (top), $T_{\rm eff} = 3600$ (middle), and $T_{\rm eff} = 3200$ (bottom). The difference between the noisy artificial and noiseless spectra is displayed at the bottom of each panel. The dashed lines are the subintervals chosen in this case to enclose regions with significant line flux over which we will compute the RMS difference between the noisy artificial spectrum and the grid of noiseless synthetic spectra. In the lower left of each panel is the RMS difference between the noisy and noiseless spectrum, measured over the intervals marked by the vertical dashed lines and normalized to the number of points in these intervals.

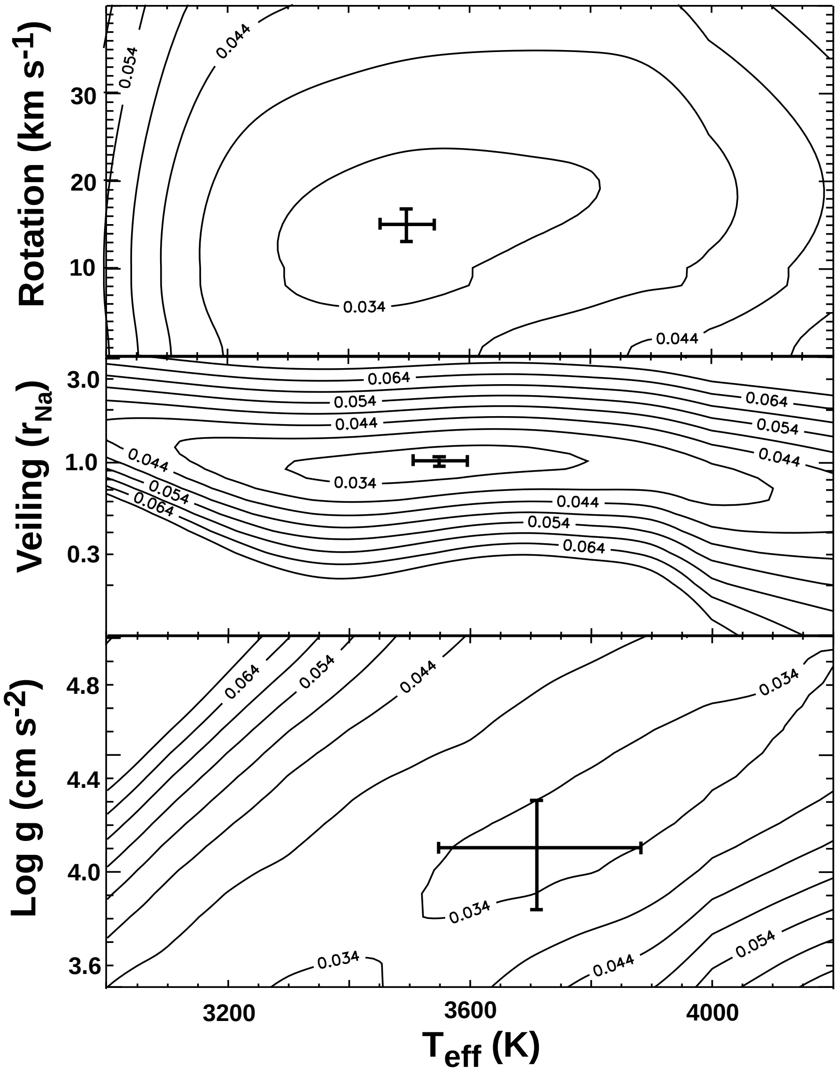

Figure 2.4 Sections through the error hypersurface comparing the noisy artificial spectrum from Figure 2.3 (where fluxes are normalized to one) to synthetic spectra with other parameters. The contours show the RMS deviation of the noisy spectrum from the model at each point in the parameter space. We produced each two–parameter plot while holding the other two variables fixed at the values matching the correct values for the target spectrum. The error bar at the RMS minimum in each plot represents the standard deviation of the best fit value for $S/N = 30$ spectra with different noise seeds. Variation of the RMS difference between the noisy artificial spectrum and different synthetic models as the $T_{\rm eff}$ and $v \sin i$ of the models is varied (top). Variation of the RMS difference as $T_{\rm eff}$ and $r_{\rm Na}$ are varied (middle). Variation with $T_{\rm eff}$ and $\log g$ (bottom).

accurately to correct for the sensitivity of the equivalent ratio to temperature.

When we have data available for both the Na and the ^{12}CO intervals, we are able to solve for $\log g$ rather than just assume its value. We begin by assuming $\log g = 3.5$ and follow the procedure outlined in the previous subsection. We take the values of $T_{\rm eff}$ and r_{Na} that this process produces and use them to compute the ratio of photospheric equivalent widths in the ^{12}CO and Na intervals. Photospheric equivalent width is the equivalent width of a line in a spectrum from which additional non–photospheric continuum has been removed (Appendix A). With the photospheric equivalent width ratio and $T_{\rm eff}$, we can use the relations plotted in Figure 2.5 to estimate $\log g$ and use this new value of $\log g$ in an iteration of the procedure for deriving $T_{\rm eff}$, $v \sin i$ and r_{Na} from the observed spectrum of the Na interval. Note that at low temperatures and high surface gravities, the Na line wings extend beyond the spectral interval over which we compute the equivalent width for the Na interval. When data with broader spectral coverage are available, the measured equivalent width should be computed only over the marked 100 Å interval for comparison to Figure 2.5. When the data cover a similar or narrower spectral interval, observations of cool and/or high surface gravity stars must be corrected for the fact that the intensity at the edges of the band is not fully at the level of the photospheric continuum. Typically, the iterative procedure converges quickly on a value for $\log g$. The first two panels of Figure 2.6 illustrate how the derivation of parameters from the Na interval plus the use of the ^{12}CO interval photospheric equivalent width work together to produce the correct value for all four parameters.

In the youngest YSOs, the excess non–photospheric emission can be many

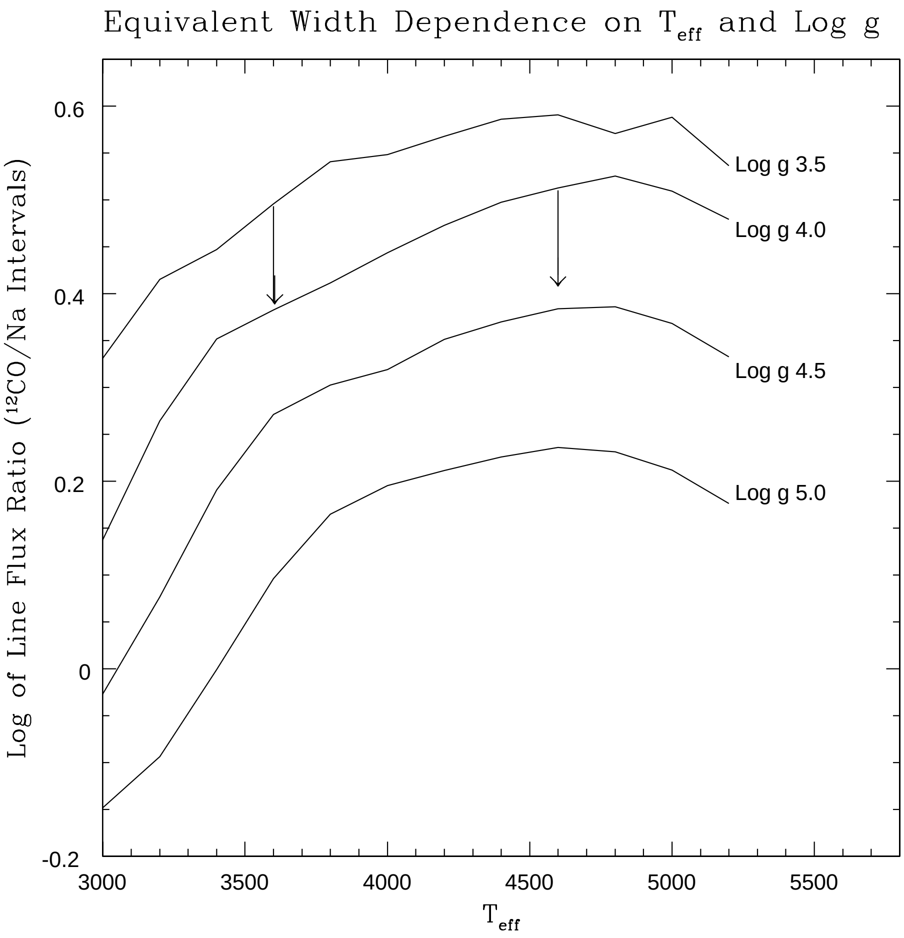

Figure 2.5 The ratio of CO interval equivalent width to Na interval equivalent width as a function of temperature, plotted for surface gravities between $\log g = 3.5$ and $\log g = 5.0$. Equivalent widths were computed over the Na and ^{12}CO intervals as defined in Figure 2.1. The relatively flat shape of these isogravity lines with temperature illustrates the value of the ^{12}CO/Na line flux ratio as a good diagnostic of surface gravity. The vertical arrows indicate the amount of vertical shift in these isogravity contours that will occur in the presence of a 2.5 kG magnetic field. The equivalent widths of the Na interval increase by 20 – 25% causing objects plotted on this figure to have lower derived derived surface gravities (lower by $\sim$0.4 - 0.5 log g) when magnetic fields are taken into account.

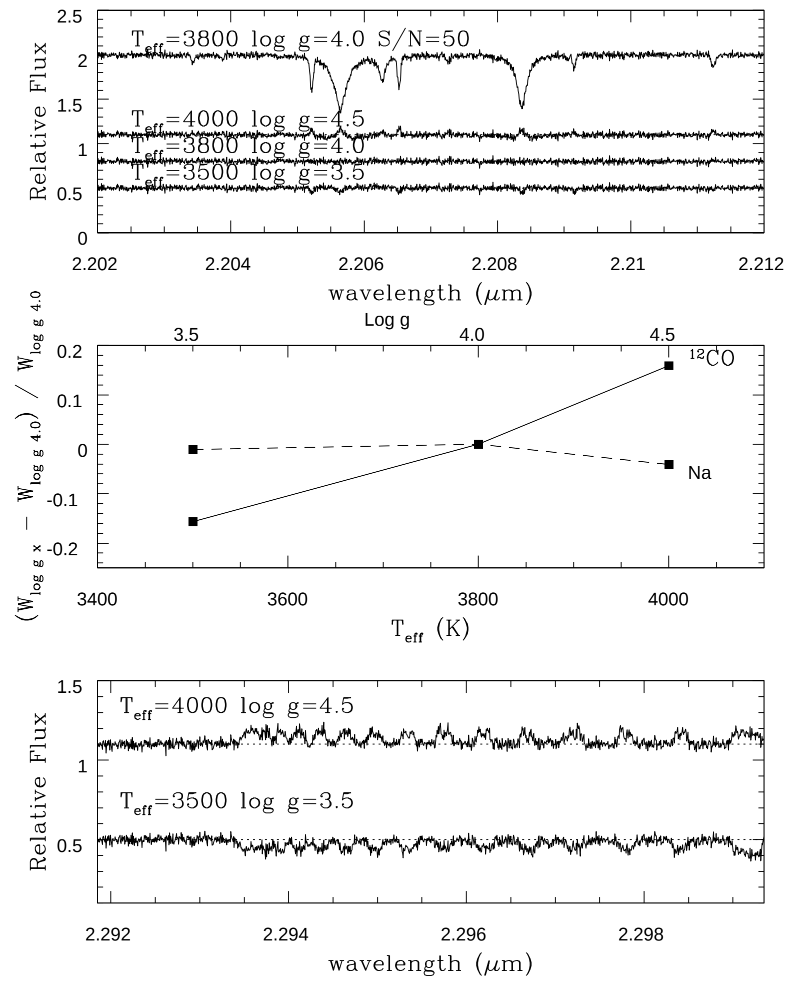

Figure 2.6 Demonstration of simultaneous derivation of $T_{\rm eff}$ and $\log g$. Error space for determinations from Na interval alone has a broad minimum in direction of increasing temperature and increasing $\log g$ simultaneously. The top panel shows a $S/N = 50$ synthetic spectrum for ($T_{\rm eff}$, $\log g$)= (3800 K, 4.0). Below that we show differences between this spectrum and models for $(T_{\rm eff}, \log g)$ = (4000 K, 4.5), (3800 K, 4.0), and (3600 K, 3.5). Residuals in each case are small. The middle panel shows the difference between the equivalent width of the Na and CO interval for these $(T_{\rm eff}, \log g)$ pairs and $(T_{\rm eff}, \log g)$ = (3800 K, 4.0), normalized to the equivalent width of the (3800 K, 4.0) spectrum. The strong variation in this quantity for the CO interval (bottom panel) shows that iterating between $T_{\rm eff}$ derived from spectra of the Na interval and $\log g$ derived from the CO/Na photospheric equivalent width ratio (Figure 2.5) can break the temperature–gravity degeneracy.

times the magnitude of the emission from the photosphere itself. In such cases, the equivalent widths of the lines not only fail to represent the conditions in the stellar atmosphere but also can be extremely hard to measure. In low resolution spectra, the combination of dilution by non–photospheric emission and dilution because the features are unresolved can make reliable measures of equivalent widths very problematic if the continuum is not flat and extremely well defined. Problems with defining the continuum arise both because of instrumental problems and because of the inherent messiness both of the stellar and the telluric spectrum in the region of the ^{12}CO 2–0 bandhead. Higher resolution spectra improve the situation because they make it easier to cancel telluric lines and because line to continuum ratios are larger.

At high resolution, where we can resolve the CO bandhead and also the adjacent features in the ascending and descending R branch, and where effective telluric line cancellation is possible, we can match the depth and shape of a CO bandhead to obtain useful information about both $T_{\rm eff}$ and $\log g$ that does not depend strongly on precise determination of the continuum level. The third panel in Figure 2.6 illustrates the dependencies of $\log g$ and $\rm T_{eff}$ with wavelength at high spectral resolution and demonstrates the potential for using detailed spectral shapes in the ^{12}CO interval to improve the robustness of the stellar parameter derivation scheme. It shows the difference between the synthetic spectrum for the CO interval for ($T_{\rm eff}$, $\log g$)=(3800 K, 4.0) and (4000 K, 4.5) and (3600 K, 3.5). We see that, in addition to the equivalent width changes, there is a change in the individual line depths and in the shape of the envelope at this resolving power ($R = 50,000$). In the current work, however, we restrict ourselves to analyzing the results of detailed spectral synthesis matching for the Na interval combined with use of the Na/^{12}CO photospheric equivalent width ratio to arrive at accurate values for T_{eff}, $v\sin i$, r_{Na} and $\log g$.

2.2.3 Behavior of Spectral Lines

The Na line doublet at 2.2 μm is sensitive to temperature and gravity. Strong damping wings are apparent in these lines. (see fig. 2.2) For collision dominated gas, the strength of these Na lines will depend on the number of absorbers, which is governed by the balance between neutral and ionized species. Neutral sodium has a relatively low ionization potential (5.1 eV), making the population balance between neutral and first ionized state sensitive to changes in T_{eff} at cooler temperatures ($<$ 5000K). These lines get stronger as the effective temperature decreases from 5000K. This can be explained by the increase in the population of the neutral species (N_0) relative to the population in the first ionized state (N_1) from the Saha equation (eqn. 2.1).

$$\frac{N_1}{N_0} = 0.665\frac{u_1}{u_0}T^{\frac{5}{2}}10^{-\frac{5040I}{kT}}\frac{1}{P_e} \tag{2.1}$$

These sodium lines are also sensitive to changes in the surface gravity. For a collision dominated gas, a decrease in surface gravity corresponds to a decrease in electron pressure (P_e). Therefore, the strength of Na lines should increase with increasing P_e, according to eqn. 2.1 above, as the population of neutrals increases by pressure recombination.

The decrease in strength of (2–0)^{12}CO absorption with increasing gravity can be explained in part by the increase in the continuous opacity with increasing P_e. The dominant source of continuum opacity for cooler stars is H^- (Gray 1992). As the gravity increases, the increase in P_e results in a greater H^- column density. This effectively brings the CO line formation region closer to the surface of the star, making the strength of the absorption decrease. In general, line strength increases with broadening. For example, larger microturbulence in giants vs. dwarfs broadens the line opacity of CO across a greater wavelength range causing the line to get stronger as the gravity decreases, in this case. The decrease in (2–0)^{12}CO strength with increasing temperature is explained by an increase in photo dissociation that lowers the number of CO absorbers.

2.3 Analysis of Errors

Now that we have developed a procedure for determining stellar parameters from high resolution spectra, we would like to know how well it works, both the sensitivity of the fitting routine and the uniqueness of the derived solutions. We discuss here four classes of uncertainty: (1) The sensitivity of the model fitting to random noise in the spectra. (2) Internal systematic uncertainties arising from the optimization scheme and from degeneracies between various stellar parameters. (3) External systematic errors introduced by transformations from one theoretical framework to another. (4) Errors arising from non–random effects present in the data. We evaluate the effects of these problems on derived parameters using simulations, real data, and modifications of real data. We first analyze the errors in parameters derived using only the Na interval and then discuss changes in these errors and the uncertainty in the determination of $\log g$ when observations of both the Na and ^{12}CO intervals are available.

2.3.1 Magnetic Fields

The role of magnetic fields in the evolution of young stars may be significant. Strong magnetic fields have been measured in a small number of T–Tauri stars (Johns-Krull et al. 1999), by modeling the shape of stellar absorption lines that have been broadened by Zeeman splitting. The evidence suggests that magnetic fields may be quite strong in at least some T–Tauri stars. A typical field strength of 2.5 kG is found from magentic field measurements in six T–Tauri sources (Johns-Krull et al. 2001).

We calibrate the effects of magnetic fields on our results by comparing model spectra with a 2.5 kG magnetic field to one that has no magnetic field, while keeping the other parameters (i.e $T_{\rm eff}$, $\log g$, $v\sin i$) fixed (fig. 2.7).

Lines that are broadened due to Zeeman splitting can cause errors in the derived $v\sin i$ broadening, if the effects of magnetic fields are ignored. Since our spectral synthesis models do not have magnetic field strength as a free parameter, we investigate how Zeeman broadening affects the derived rotation using synthesis models that do account for the effects of magnetic fields on the shapes and depths of the lines in the Na interval (Johns-Krull, private communication). Unaccounted magnetic fields with strengths up to 2.0 kG causes line broadening that results in overestimates of $v\sin i$ broadening of $\leq$ 10% and $\leq$ 15% in stars with temperatures

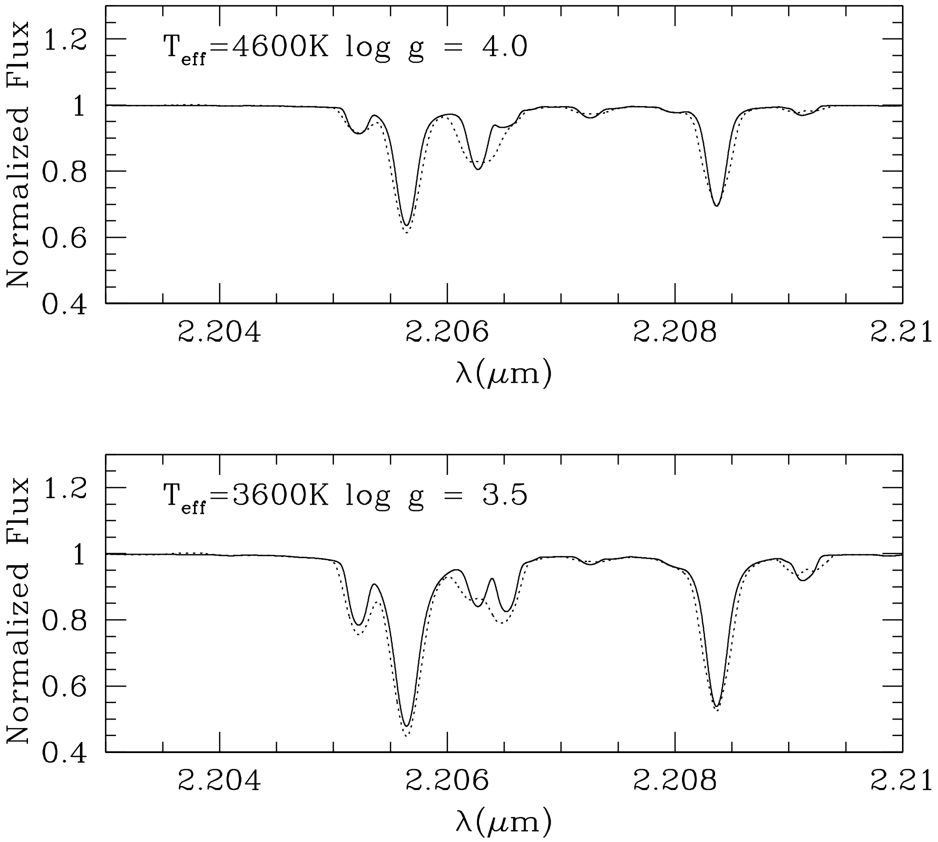

Figure 2.7 Using a synthetic spectrum that takes into account the effect of magnetic fields on the shapes of photospheric lines, two cases are shown. In both panels, synthetic spectra with no magnetic fields (solid line) are compared with one that has significant field strength of 2.5 kG (dotted line). In this strong magentic field case, the effects of Zeeman splitting are clearly evident in this Na interval region. The increase in equivalent widths is ~20% and ~25% for these two temperature cases: 4600 K (top panel) and 3600 K (bottom panel),

of 3600 K and 4600 K, respectively.

2.3.2 Random Errors

A generalized assessment of the sensitivity of our fitting routines to random errors is not possible. The sensitivity of the $T_{\rm eff}$, $v\sin i$, and r_{Na} determinations will be not only a function of the signal–to–noise ratio of the spectra but also will depend on the widths of the lines and on their strengths relative to the continuum (that is, effectively on $v\sin i$ and r_{Na}). By working with a typical spectrum, however, we can get a rough idea of what signal–to–noise ratio we require to reach the point where random noise in the spectra no longer dominates the uncertainty in determining stellar parameters. We illustrate the sensitivity to random errors by taking a synthetic spectrum for the model shown in Figure 2.1a and adding more and more Gaussian random noise to it. We take each artificially noisy spectrum and map its RMS deviation from the points in our hypercube of synthesis models and compute the location of the minimum by interpolation. At each signal–to–noise level, we re–seed the noisy spectrum 30 times and repeat the minimization procedure. The standard deviation about the mean value of each derived parameter for this ensemble of noisy spectra then reflects the uncertainty due to random noise at a given signal–to–noise level. Figure 2.8 shows how the standard deviation about the mean derived $T_{\rm eff}$ varies for noisy versions of the Na interval spectrum in Figure 2.1a (with continuum added to make $r_{Na} = 1$) as the signal–to–noise increases. For this particular case, the uncertainty in the $T_{\rm eff}$ due to random errors is less than 100 K for $S/N > 50$.

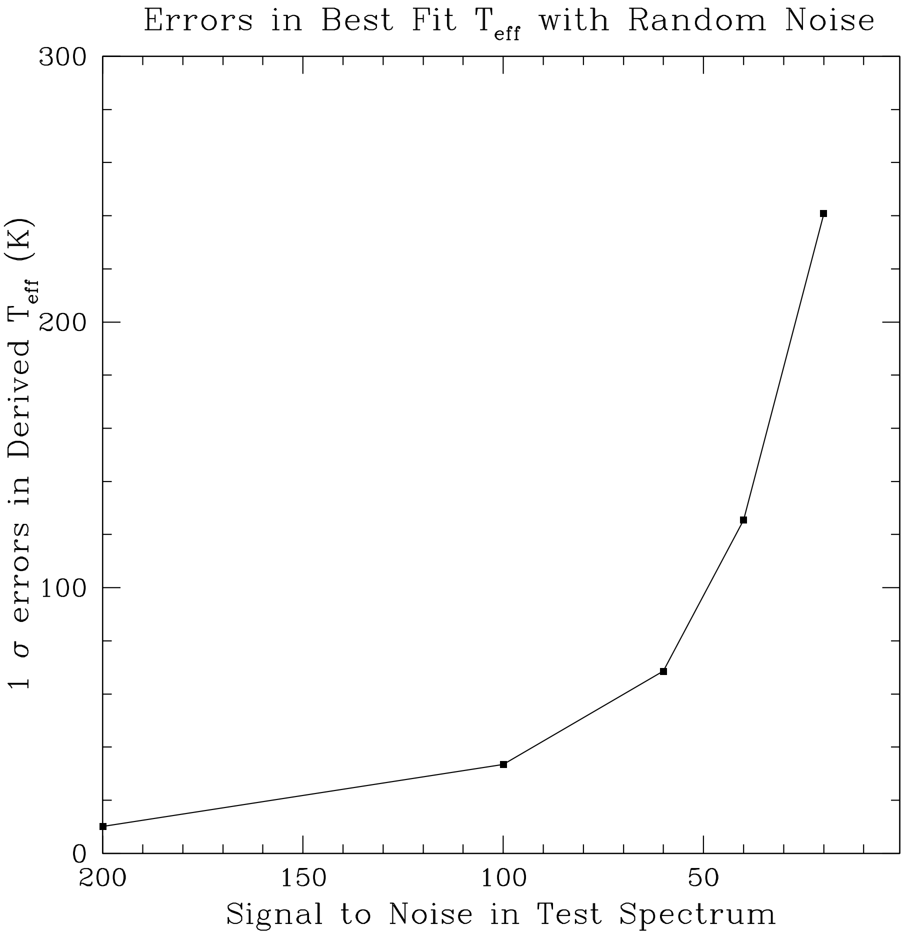

Figure 2.8 Standard deviation of the derived value of $T_{\rm eff}$ (derived using the Na interval only) as a function of S/N. To construct this plot, we used a noisy artificial spectrum with ($T_{\rm eff}$, $\log g$)= (4200 K, 4.0), $v\sin i$=15 km s^{-1},r$_{Na}$=1.0) as the target and fit for the best temperature allowing all parameters except $\log g$ to vary. We compared the target and model spectra at sampling points spaced every $\Delta\lambda/\lambda$=(1/240,000) along spectra smoothed to a resolving power of 50,000. The signal–to–nose ratio is that appropriate to data binned to channels $\Delta\lambda/\lambda$=(1/50,000) wide.

The model results in Figure 2.6 indicate that random errors result in uncertainties of less than one spectral subclass as soon as the signal–to–noise ratio is greater than 35 at $R = 50,000$. For sources with excess continuum emission, the signal to noise must be higher by a factor of (1+r_{Na})/2 before this statement is correct. Once the signal–to–noise ratio exceeds $\sim$35$\times$(1+r_{Na}), other forms of errors begin to dominate the uncertainty in the derivation of stellar parameters from the K band spectra fitting technique.

2.3.3 Uncertainties Arising from Internal Systematics

Partial degeneracies in the output lineshapes between different groupings of stellar parameters have the effect of exaggerating the uncertainties caused by random errors along certain directions in the parameter hypercube. For minimizations of model–observed spectral differences in the Na interval, this effect is most evident in the broadness of the minimum RMS error along a diagonal in the $T_{\rm eff} - \log g$ plane (Figure 2.4, bottom). When the spectra are noisy or imperfect, there is a range of temperature–gravity pairs with very similar RMS values.

The partial degeneracy in the temperature–gravity plane of the error space means that we can introduce systematic errors in the derived $T_{\rm eff}$ when we assume a value of $\log g$ and then derive the temperature. By finding the best fit temperature for synthetic target spectra with $\log g = 4.0$ using temperature grids of synthetic spectra at $\log g = 3.5$ and 4.5, we can assess the effects of the $T_{\rm eff} - \log g$ degeneracy. Figure 2.11 illustrates these effects by showing how the derived temperatures deviate from the target spectrum temperature at different target values of $T_{\rm eff}$. Typically, a mis–estimate of the surface gravity of 0.5 in the log results in a derived temperature that differs from the temperature one derives with the correct value of $\log g$ by about 7%. This difference is approximately 1–2 spectral subclasses over the range of $T_{\rm eff}$ relevant to our study. If we later obtain an independent estimate of $\log g$, we can correct the derived $T_{\rm eff}$. For data where we derive an effective temperature from the Na interval assuming some value of $\log g$, correcting the derived $\log T_{\rm eff}$ by 0.06 for every $\log g = 1$ difference between the assumed and the correct values, we recover the actual value of $T_{\rm eff}$ to within better than 4%.

The way in which we create the error space from comparisons of observed target spectra and synthesized model spectra may have a systematic effect on the derived parameters. The error space shown in Figure 2.4 represents the RMS deviation of the target spectrum from the models over selected intervals where line flux was present (see Figure 2.3). This scheme allows for variations of feature depths and shapes. Because it is a straight RMS, it weights the stronger features, in particular the Na features, more heavily. One might ask if this is the best scheme, i.e. does it make the uncertainties in the derived parameters larger than they need to be? In its favor is the ability of the Na line depths to distinguish the value of r_{Na} and the sensitivity of the depth and shape of these lines to $T_{\rm eff}$ and $\log g$. On the other side of the ledger is the low weight a straight RMS gives to the weaker Sc and Si lines. The ratio of these lines is the most sensitive temperature indicator in the Na interval. More complex schemes that make better use of the information content of the weaker lines and the subtleties of the lineshapes are certainly possible. The simple RMS scheme, however, has the great advantage that it finds the right parameters robustly over our whole temperature range at various values of r_{Na} and $v\sin i$ and that its level of complexity is appropriate to signal to noise ratios of 30–50 where random errors are just beginning to give way to systematics.

2.3.4 Accuracy of Derived $v\sin i$ Values with Effective Temperature

We assess how accurately we can measure $v\sin i$ as a function of spectral type using models with stellar rotation (25 km s^{-1}), instrumental smoothing ($R = 50,000$) and Gaussian noise ($S/N = 30$ per $R = 240,000$ channel) added to simulate real data. We fit the modified synthetic spectra to a set of noiseless models keeping the temperature fixed at the correct value and allowing the RMS minimization algorithm to select the best $v\sin i$ value. This was repeated with different noise seeds (30) for each selected temperature model giving a mean and 1 σ error $v\sin i$ fit for temperatures between 3200K and 4400K.

Figure 2.9 shows our ability to detect rotational broadening in spectra with moderate noise is better than 2 km s^{-1} and insensitive to spectral type.

2.3.5 Errors in the Radial Velocity Determination

The best radial velocity shift of the observed program stars relative to synthesis models was determined within the RMS minimization algorithm along with the best–fit stellar parameters. A narrow search range in radial velocity space was selected by inspection. The data spectra were first interpolated to a higher dispersion ($\mathrm{R_{pix}} = 360,000$), consistant with the wavelength binning of the models. The minimum RMS of the residuals to the fit selected the best sub–pixel radial velocity

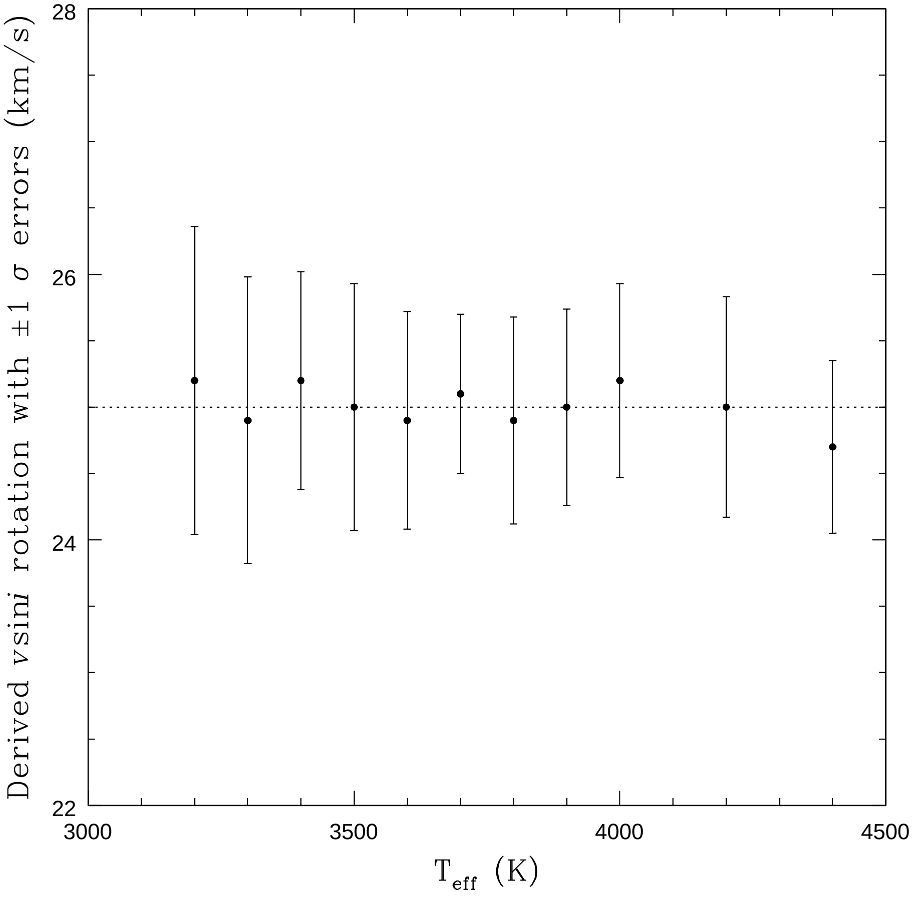

Figure 2.9 The recovered $v\sin i$ rotation and 1 σ errors as a function of effective temperature. The dotted line shows the initial $v\sin i$ broadening added to the synthesis models (25 km s^{-1}), along with Gaussian noise (S/N = 30 per R_{pix} = 240,000) and for each temperature case shown. With the temperature fixed at the correct value, the best $v\sin i$ value was determined by the RMS minimum. Using 30 independent noise seeds, the mean and 1 σ errors in the recovered $v\sin i$ values are plotted with vertical error bars. The mean $v\sin i$ recovered from the fits is flat with temperature, indicating no dependence of derived rotational broadening on late spectral types. The errors get smaller as the temperature increases from 3200K to 4400K, consistent with the decrease in the intrinsic widths of the stellar lines. The errors increase as $v\sin i$ gets smaller. At $v\sin i$ of 10 km s^{-1} the errors are $\sim$25% larger.

shift.

We examine how errors in the radial velocity fit affect our determination of the stellar parameters ($v \sin i$ stellar rotation and effective temperature) in Fig. 2.10. Stellar parameters determined from line widths (i.e $v \sin i$ rotation) are artificially elevated with mis–matches in radial velocity, while stellar parameters determined from line depths (i.e effective temperature and veiling), are not sensitive to radial velocity errors at the 5 km s^{-1} level.

Random errors in the radial velocity determination due to noise in the spectrum are small (< 0.5 km s^{-1}) for spectra with S/N > 30 per pixel ($R_{\rm pix} = 240,000$). The errors in $v \sin i$ are dominated by mis–matches in the line widths ($1\,\sigma = 0.6 - 1.2$ km s^{-1}) caused by noise in the spectrum (Fig. 2.9), and are not dominated by errors in the determination radial velocity offset.

2.4 Comparison with Standards and External Systematics

A test of the applicability of our use of synthetic spectra and observations of the narrow interval around the sodium lines at 2.2 μm for accurate determinations of effective temperature is needed. We have therefore compared $T_{\rm eff}$ for MK standard stars derived using our technique with determinations made by analysis of optical spectra of the same targets. In this section, we present high resolution near–IR observations of MK standards and quantify the accuracy of our near–IR technique. Table 2.1 presents the list of MK standards used in our comparison. It lists the optically derived spectral types and luminosity classes, the effective temperature derived from the optical spectral type, $T_{\rm eff}$ from our analysis of the Na

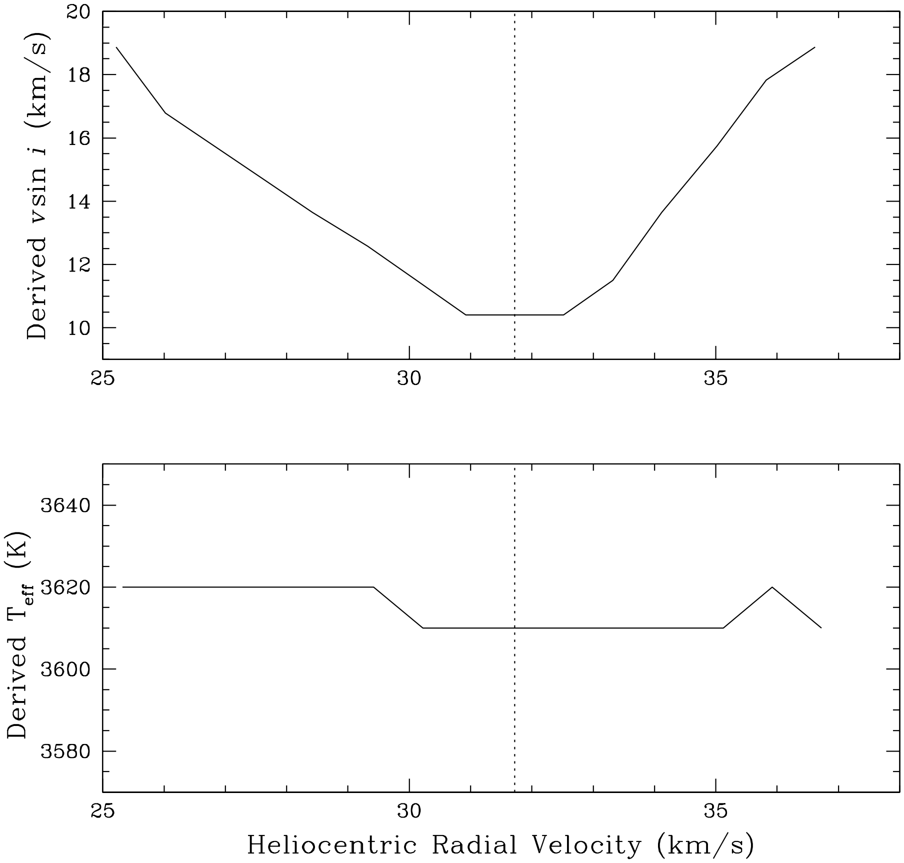

Figure 2.10 The effect of errors in the radial velocity determination upon the derived $v\sin i$ rotational broadening and stellar effective temperature. The dotted line indicates the best radial velocity fit for MK standard, HD131976 along with the corresponding best fits for $v\sin i$ and $T_{\rm eff}$ (y axis in both panels), as listed in Table 2.1. The top panel shows how the derived fits for $v\sin i$ grow as the radial velocity is fixed at other values away from the best fit value. A minimum in the derived $v\sin i$ expected for the correct radial velocity. The bottom panel shows that the derived $T_{\rm eff}$ is insensitive to errors in the radial velocity.

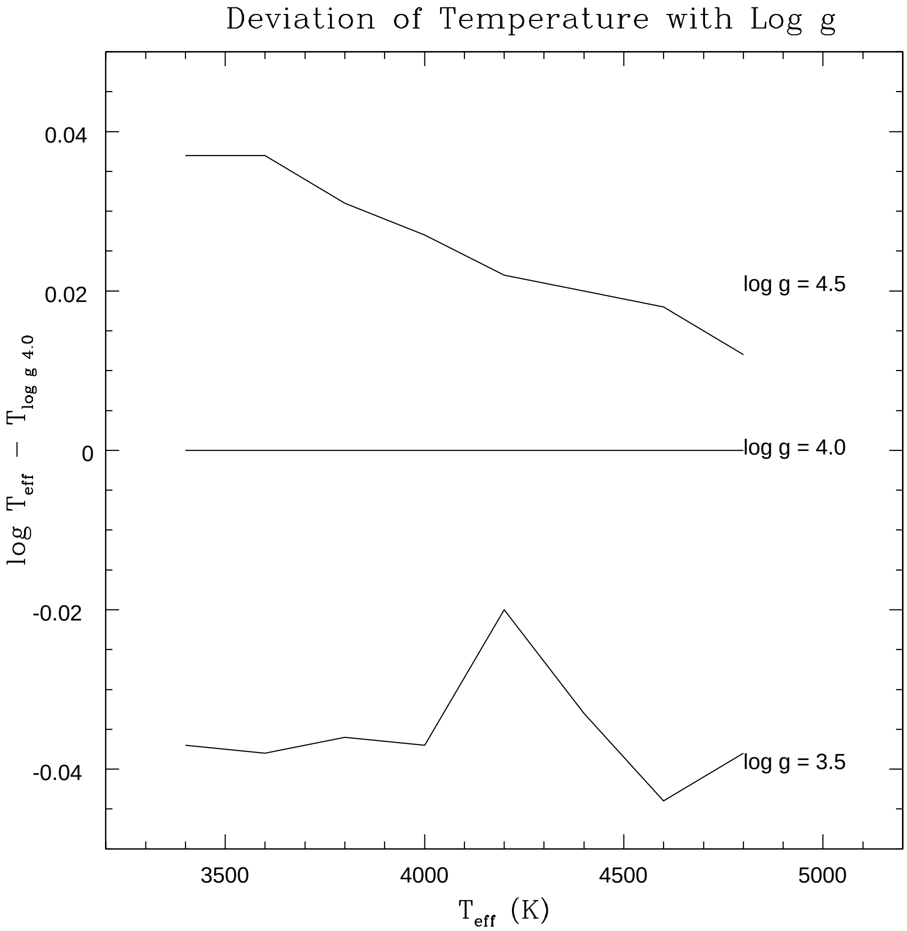

Figure 2.11 The effect on the best-fit value of $T_{\rm eff}$ of assuming an incorrect value for $\log g$. At each temperature, a synthetic target spectrum with $\log g$=4.0 and two grids of `MOOG` models with $\log g$=3.5 and $\log g$=4.5 were created. We then fit for the temperature of the target spectrum using each of the grids with the different values of $\log g$. The solid lines show the difference between the logarithm of the best–fit $T_{\rm eff}$ to the target spectrum derived by using the $\log g$=3.5 or 4.5 grids and the logarithm of the target spectrum $T_{\rm eff}$. The top line shows the results for the $\log g$=4.5 grid while the bottom line shows the results for the $\log g$=3.5 grid.

TABLE 2.1
OBSERVED MK STANDARDS

Standard Star	Spectral Type	Optical T_{eff}[c] (K)	Near–IR T_{eff}[d] (K)	Optical $v \sin i$ (km s^{-1})	Near–IR $v \sin i$ (km s^{-1})	Metal-licity [Fe/H]
HD 117176[a]	G4V[1]	5636	5980	10[8]	$<$3	–0.11[3]
HR 4496[b]	G8V[1]	5439	5400	$<$15[8]	$<$9	–0.14[4]
HR 4496[a]	G8V[1]	5439	5460	$<$15[8]	$<$3	–0.14[4]
HD 185144[a]	K0V[1]	5152	5260	$<$15[8]	$<$3	–0.23[3]
GL 28[b]	K2V[1]	4838	4880	2.5[9]	$<$9	–0.05[6]
HR 5568[b]	K4V[1]	4539	4580	$<$12[8]	$<$9	0.016[7]
GL 338A[b]	M0V[2]	3837	3660	2.9[10]	$<$9	
GL 338A[a]	M0V[2]	3837	3650	2.9[10]	$<$3	
HD 131976[a]	M1.5V[1]	3589	3610	1.4[11]	10	
GL 15A[b]	M2V[1]	3523	3630	$<$2.9[10]	$<$9	
GL 402[b]	M4V[2]	3289	3290	$<$2.3[10]	$<$9	
HD 188512[a]	G8IV[1]	5100[5]	4700	1.8[13]	$<$3	–0.30[5]
HD 142091[a]	K1IVa[1]	4800[5]	4680	1.9[14]	$<$3	–0.04[5]

[a] Observations made using PHOENIX on the KPNO 4–meter

[b] Observations made using Nirspec on Keck

[c] Using T_{eff}–spectral type relation of de Jager & Nieuwenhuijzen (1987) for luminosity class V sources unless otherwise noted

[d] Assumed $\log g$=4.5 for dwarfs and $\log g$=3.5 for the two sub–giants sources (McWilliam 1990).

REFERENCES.—(1) Keenan & McNeil (1989) (2) Kirkpatrick et al. (1991) (3) Hearnshaw (1974b) (4) Hearnshaw (1974a) (5) McWilliam (1990) (6) Marsakov & Shevelev (1988) (7) Taylor (1995) (8)Glebocki & Stawikowski (2000) (9) Strassmeier et al. (2000) (10) Delfosse et al. (1998) (11) Duquennoy & Mayor (1988) (12) Vogt et al. (1983) (13) de Medeiros & Mayor (1999) (14) Fekel (1997)

TABLE 2.2

RECOVERED PARAMETERS WITH ROTATION ($v \sin i = 25$ km s^{-1}) AND VEILING ($r_K = 2.0$) ADDED TO MK STANDARDS

MK Standard	Best Fit $T_{\rm eff}$ (K)	Recovered $T_{\rm eff}$ (K)	Recovered $v \sin i$ (km s^{-1})	Recovered Veiling (r_K)	RMS
HD 117176	5980	5240	27.0	3.8	0.00271
HR 4496	5400	5230	29.0	2.6	0.00152
HD 185144	5240	5000	29.0	2.7	0.00189
GL 338A	3650	3765	25.0	3.0	0.00333
HD 131976	3610	3580	30.0	2.5	0.00244
HD 188512	4700	4620	30.0	2.3	0.00165
HD 142091	4680	4620	29.0	2.5	0.00209

interval, the stellar metallicity, and the instrument used to take the data. The formal signal–to–noise ratio of these sources was typically 130. Most of the sources were observed on a single run in 2000 May with the PHOENIX spectrograph (Hinkle et al. 1998) on the KPNO 4m telescope. The 4 pixel slit used for these observations yielded a resolving power of 50,000 with a $\lambda/\Delta\lambda$ per pixel of 240,000. The observations covered a wavelength range of 0.01 μm centered on the Na features at 2.207 μm. Additional observations made with Nirspec on the Keck telescope were kindly made available to us by T. Greene. For these observations, the resolving power was 16,500 with individual pixels covering $\lambda/\Delta\lambda = 66,000$. The order containing the Na interval covered a total of 0.034 μm.

The comparison of effective temperatures derived from optical spectral types and the $T_{\rm eff}$ values we derive from the spectra of the Na interval reflects the sum of the internal errors in our determination of $T_{\rm eff}$, errors in spectral typing from optical observations, and errors in converting from spectral types to effective temperatures. This last error can be substantial. de Jager & Nieuwenhuijzen (1987) estimate errors of 0.021 in $\log T_{\rm eff}$ in their spectral type–$T_{\rm eff}$ conversion for dwarfs corresponding to $\pm$200 K at $T_{\rm eff}$=4000 K. Errors in the assumed cosmic abundance also cause external systematic differences in the $T_{\rm eff}$ scale. At 3600 K, lowering the metallicity by 0.25 dex [Fe/H] lowers the best fit temperature by 150 K. While the metallicities of individual embedded pre–main sequence stars will not be available to us, the small deviations from solar metallicity for young stars makes metallicity less of an issue for these objects. Typically Δ[Fe/H] $<$ 0.1 (Padgett 1996).

Eight of the MK standards we have observed as a test sample have measured abundances ranging from +0.02 dex above solar to -0.30 dex below (Table 2.1). In analyzing the remaining stars, we assume solar metallicity. For MK standards with measured non–solar metallicities, we computed separate grids of synthetic spectra for comparison with the observed spectra. The table also contains temperatures derived from optical spectral types. In comparing our own IR derivations to the optical results, we find a mean value of $\Delta T_{opt-IR}/T_{IR}$ of 0.0018 with a dispersion of 0.036 for the luminosity class V objects using the spectral type–$T_{\rm eff}$ relation of de Jager & Nieuwenhuijzen (1987). This difference corresponds to 140 K at $T_{\rm eff} = 4000$ K or less than the quoted error in the spectral type–temperature conversion relation (de Jager & Nieuwenhuijzen 1987). Figure 2.12 plots the temperatures derived from our analysis of the Na interval against temperatures derived by converting the observed spectral type to T_{eff} using a variety of relations from the literature. For a given target, the spread of different symbols along the horizontal axis illustrates differences in the conversion between spectral type and temperature (Allen 2000; Alonso et al. 1996; Ali et al. 1995; de Jager & Nieuwenhuijzen 1987). We include temperatures derived using B–V colors and the conversion relation of Kenyon & Hartmann (1995). The small vertical error bars (placed on the de Jager $\mathrm{T_{eff}}$ points) show our estimate of the 1σ uncertainty due to random noise in the data. These values were derived by carrying out an analysis similar to that used to create Figure 2.8 at the temperature and signal–to–noise ratio appropriate to each MK standard. The size of these errors indicates that systematic effects must dominate any differences between the optical and infrared results.

For observations of embedded young stars, uncertainties in metallicity are probably small, but systematic differences between the models and the data at the correct metallicity could affect our determination of the infrared excess as well as of the temperature. For the comparison with MK standards in Figure 2.12, we fixed $\mathrm{r_{Na}}$=0 and used the metallicities listed in Table 2.1 or solar metallicities when no measurements were available. Since the stellar atmosphere models available to us differed in metallicity by 0.5 dex we constructed the spectral synthesis grids for mildly metal–poor stars ($0.3 \leq [\mathrm{Fe/H}] \leq 0$) using solar metallicity model atmospheres but synthesizing the spectra using the appropriately lower abundances. If we constrain the search grid to a fixed veiling ($\mathrm{r_{Na}} = 0$) and metallicity determined from the literature the best fit model (as determined by the minimum RMS difference) has a noticeably non-zero residual equivalent width when compared to the

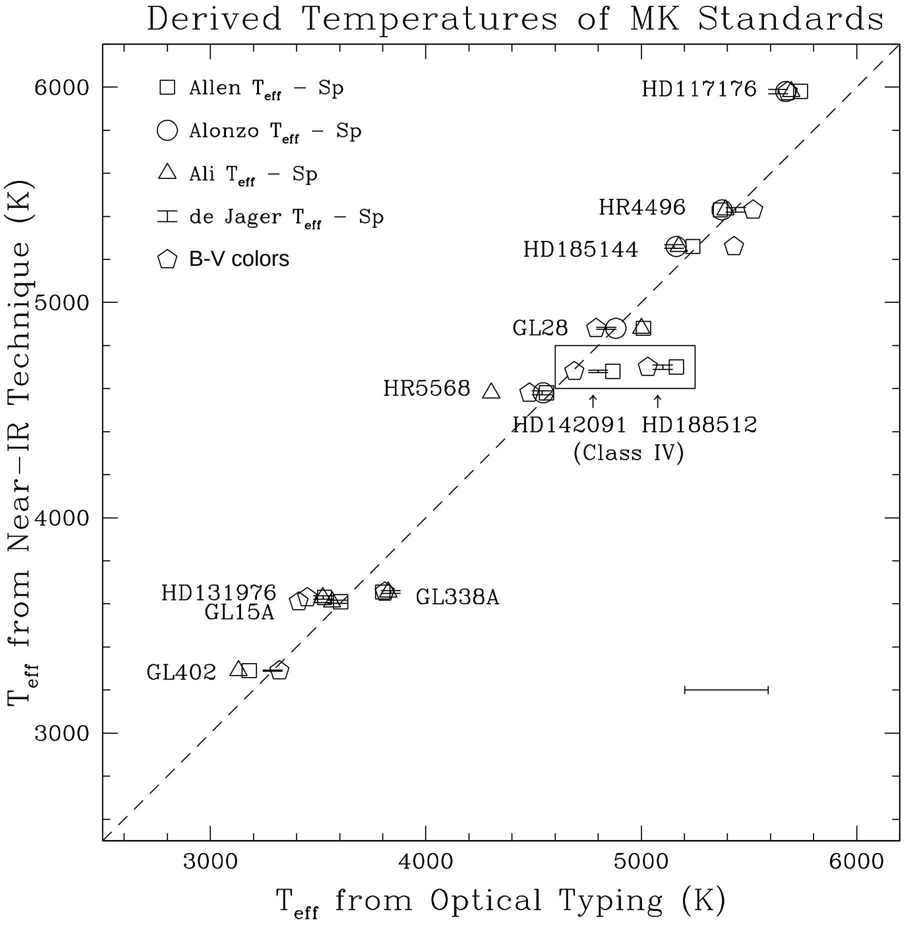

Figure 2.12 Test of our effective temperature determinations (vertical axis) against temperature determinations available in the literature for MK standards (horizontal axis). The vertical error bars represent ±1σ uncertainties due to the noise in the observed spectra, determined by calculations similar to those used in Figure 2.8 at each temperature and at a signal to noise ratio comparable to that of the data. The horizontal error bar in the lower right corner of the Figure shows the 1 σ uncertainty in the spectral type to T_{eff} conversion at 4000 K (de Jager & Nieuwenhuijzen 1987). We placed the symbols in the x direction by converting the spectral types (Table 2.1) to T_{eff} using various spectral type–T_{eff} relations: open circles (Alonso et al. 1996), open triangles (Ali et al. 1995), open squares (Allen 2000) vertical error bars (de Jager & Nieuwenhuijzen 1987). Unless otherwise marked, all sources are dwarfs, luminosity class V. The open pentagons show the T_{eff} derived from the reported B–V colors using the conversion relation of Kenyon & Hartmann (1995).

observed spectrum of the MK standard.

If we allow r_{Na} to be a free parameter in the fits for the MK standards, as we do for the embedded protostars, the best fit models have a lower RMS than they did for the fits constrained to r_{Na}=0 and a near–zero equivalent width residual. Typically, r_{Na}= 0.2 for the standards in our sample. If such an offset between the fit value of r_{Na} and its true value were present for the analysis of the target stars, it would imply a systematic overestimate, $\Delta r_{Na}=0.2 \times (1+r_{Na})$. Further analysis with a better sample of MK standards will be needed to understand this effect more fully.

2.4.1 Systematic Problems with the Data

The high resolution spectra we use to derive stellar parameters are imperfect representations of the source spectra. Systematic problems with the data include imperfect flat–fielding, defects in the cancellation of telluric features and the presence of scattered light or leaked out–of–order stellar radiation. By choosing restricted wavelength intervals over which to match the synthetic models to the data, we minimize flat–fielding effects since mismatches in the shapes of the synthetic and observed lines then play a bigger role in influencing the RMS difference. At high spectral resolution, the residuals of telluric lines cover a limited and known part of wavelength space. We simply exclude these regions from our fitting spectral matching intervals. Scattered light is usually removed in the data analysis if the source and sky have been switched regularly between two positions along the slit.

In particular for the cooler stars and stars with higher surface gravities, the extended wings on the Na lines, coupled with the limited instantaneous spectral coverage of the spectrometers makes it hard to set the continuum level in the spectra correctly. In our analysis, we have chosen to minimize the RMS difference between the target and synthetic spectra without considering the value of the integral of the residuals. The value of this integral could be used, however, to re–set the continuum level within the observed band.

All of the tests of our analysis technique to this point have used synthesized model spectra with artificial noise as the targets. In order to test the ability of our fitting routine to derive stellar parameters from data containing realistic amounts of systematic deviation from ideal spectra, we have altered our PHOENIX observations of MK standards (§2.4). We began with MK standards with very small rotation velocities ($v\sin i \leq 10$ km s^{-1}). These main sequence objects also had no intrinsic veiling (r$_K$=0). We first used the fitting routine to show that we could recover very close to the published value of $T_{\rm eff}$ for these stars. We then added a known amount of rotation ($v\sin i$ = 25 km s^{-1}) and veiling ($r_K = 2.0$). The Na interval spectra of these doctored stars were then analyzed using our standard procedure. For 6 of the 7 objects, we recovered effective temperatures close to those derived from the unaltered stellar spectra (Table 2.2). Generally, the recovered temperatures were within $\sim$1 spectral subclass, but systematically lower and with corresponding higher recovered veiling values, consistent with the degeneracy along this error axis, recovered $v\sin i$ was closer to its initial value (within 5 km s^{-1})

2.4.2 Demonstrations

Figure 2.13 shows an application of our technique to an $R = 50,000$ spectrum of the embedded YSO IRS2 in the ρ Ophiuchi molecular cloud. The figure shows the observed spectrum of the Na interval (Chapter 3), with the best–fit synthesis model overlaid. Above and below are comparisons with the best models at temperatures 400 K above and below the best–fit $T_{\rm eff}$. For this source, the derived value of $T_{\rm eff}$ from an analysis of the Na interval alone was 4600 K with a formal uncertainty of 30 K, well below the systemic uncertainty of 140 K. Greene & Lada (1997) had previously published a spectrum of the ^{12}CO interval toward IRS 2 and we were able to use this spectrum, together with our spectrum of the Na interval to derive $T_{\rm eff}$ and $\log g$ iteratively. In the complete analysis, the derived value of $T_{\rm eff}$ was 4640 K and $\log g$=4.3.

2.5 Conclusions

We have described, demonstrated and evaluated a technique for deriving effective temperatures, surface gravities, rotation rates, and infrared excesses from high resolution of PMS stars in the near–IR. Using the Na interval at 2.2 μm, we can recover the effective temperatures of dwarf MK standards at a level well below the uncertainty in the spectral type–temperature conversion. The spectra also give us a good measure of the rotation velocity and infrared excess. With the addition of a good measurement of the relative flux between the CO 2–0 bandhead and the Na interval, it is possible to determine the surface gravity of YSOs and to remove uncertainties in the temperature caused by a partial degeneracy with $\log g$.

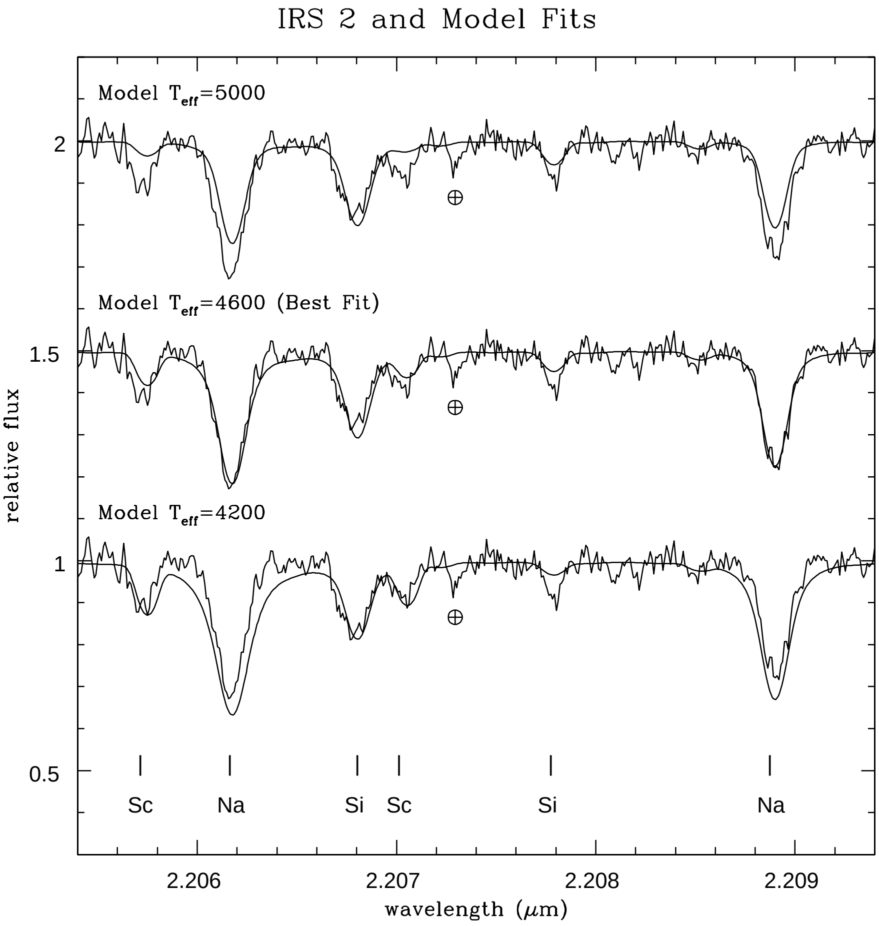

Figure 2.13 The observed spectrum of IRS2 in the ρ Oph molecular cloud compared to some synthesis models. The best fit is the middle panel.

It is clear from the results that the ability to work with weak features and to measure line shapes as well as equivalent widths can make near–IR spectroscopy a valuable tool for studies of highly obscured stars and of young objects with strong excess infrared emission. The technique we develop here is robust enough to deal with sources with a range of different signal–to–noise ratios and excess near–IR emission.

In the future, it will be worthwhile to investigate whether high resolution spectra of other near–IR intervals could add useful information about the stellar parameters. We would also like to investigate more sophisticated matching routines that might make better use of the sensitivity of individual weak features to various stellar parameters. For studies of cooler, lower mass YSOs, it would be useful to produce models and line syntheses for lower temperature objects.

Chapter 3

Stellar Properties of Pre–Main Sequence Stars from High Resolution Near IR Spectra

3.1 Introduction

High resolution spectroscopy in the near–infrared (NIR) can be a valuable tool for extracting stellar properties of highly extincted young stellar objects (YSOs). Observations at optical wavelengths are plagued by heavy extinction in the cores of star forming regions, such as in ρ Ophiuchi (Wilking & Lada 1983). Additionally, large continuum excesses from shocks due to accretion of disk material onto the YSO surface often overwhelm the stellar flux in the optical and UV (Gullbring et al. 2000). In the mid–infrared, the thermal emission from the surrounding disk can also substantially exceed the flux from the photosphere (Fazio et al. 1976; Lada & Wilking 1984; Bontemps et al. 2001). The standard model of a young star surrounded by a circumstellar disk suggests that the photospheric emission should dominate the observed emission at NIR wavelengths. (Strom et al. 1988; Kenyon & Hartmann 1990). Consequently, the NIR is the best wavelength region to observe photospheric flux from YSOs, giving us a crucial wavelength window through which to observe their physical properties, and allowing us to study earlier stages of star formation and disk accretion than are possible at optical wavelengths.

Spectroscopy offers a more direct method than photometry for measuring properties of obscured young stars. Absorption line equivalent widths and ratios are not dependent on extinction. Furthermore, the intrinsic shapes of photospheric absorption lines contain stellar kinematic and temperature information which can be fully resolved in cool stars ($T < 5500$) by high spectral resolution ($R = \lambda/\Delta\lambda \geq 10{,}000$) observations. In short, observations of photospheric lines in obscured stars at high spectral resolution can permit us to measure (1) precise radial velocities from line shifts, (2) $v \sin i$ rotational velocities from line widths, (3) effective temperatures and surface gravities from line shapes and line ratios, and (4) the veiling by hot dust from the line depths.

Stars form from the collapse of dense cores within molecular clouds (Hartmann et al. 1997; Evans 1999). This process occurs within a small range in time ($\sim 10^5$ yr, Shu, Adams, & Lizano 1987) relative to the evolution time onto the main sequence ($\sim 10^7$ yr, Palla & Stahler 2000; Hartmann 2001). Embedded clusters are sites of on–going star formation (Wilking & Lada 1983; Lada et al. 1991), so there will be a spread in age of the stars contained within. This age spread cannot be larger than the age of the cluster itself, which sets an upper limit to the difference in age of any two stars observed there. Therefore, young (embedded) clusters present a homogeneous sample of stars at similar (though not necessarily equal) ages. Clusters themselves are important since they are the dominant mode of star formation.

The nearest example of a young star forming cluster is the dark cloud in the ρ Ophiuchus region (D = 145 pc, de Zeeuw et al. 1999). The core of the cloud is compact ($d < 1$ pc), and is the site of low and higher mass stars embedded within the cloud. Because the region is rich with young stars it has been well studied. The first infrared surveys of the Ophiuchus complex resulted in the discovery of dozens of embedded YSOs within the more extincted regions of the cloud (Grasdalen et al. 1973; Vrba et al. 1975; Elias 1978a,b). Wilking & Lada (1983), surveyed the densest parts of the cloud within $10\,'$ of the $A_v = 50$ boundary in the ρ Ophiuchi cloud core. With the development of infrared detector arrays, large surveys have been carried out to verify cluster membership, detect the presence of disks, and make estimates of the star formation efficiency (Greene & Young 1992; Comeron et al. 1993; Strom et al. 1995). Mid–IR photometry has been employed to characterize the circumstellar disks around PMS stars (Greene et al. 1994; Bontemps et al. 2001). A magnitude limited ($K \leq 14.0$) NIR imaging survey of a 2.2 pc^2 region of ρ Oph was carried out by Barsony et al. (1997).

Measuring the physical characteristics of young stars is key to understanding how they evolve. Luminosity and effective temperature are crucial observational quantities that place YSOs on the Hertzsprung–Russell diagram, a fundamental tool for our understanding of stellar evolution. By using theoretical evolutionary model tracks in conjunction with observed YSO positions on the H–R diagram, we can constrain the most important stellar characteristics, mass and age. Linking the physical characteristics of young stars to their pre–main sequence evolutionary (PMS) stage is therefore a primary goal.

We use high resolution spectra of PMS stars to measure the following physical characteristics. The $v\sin i$ rotation of PMS stars will give us insights into the relationship between the young stars and their circumstellar disks. Quantifying the amount of infrared continuum excess allows us to probe the conditions of the disk. We need observational techniques uncompromised by heavy extinction or excess emission that enable direct measurements of T_{eff}, disk excess, rotation, and $\log g$ or luminosity. By comparing these physical parameters to evolutionary model tracks on the HR diagram, we can obtain fits for YSO masses and ages.

The HR diagram can be a powerful tool for obtaining masses and ages in single sources where masses cannot be measured by reflex orbital motion. Successfully combining observations with PMS stellar evolution theory relies on precise measurements of stellar parameters and detailed theoretical evolutionary model tracks. Obtaining mass information is fundamental to our understanding how single stars will evolve and how to characterize an ensemble of stars born from in a given star forming region.

Accurate spectroscopic measurements of a small sample of YSOs in a well studied cluster can serve as a check of mass determinations on larger samples made using photometric techniques. Validations of these photometric studies are critical since they are the source of our current understanding of cluster initial mass functions (IMFs).

The first estimates of the IMF in nearby star forming regions, ρ Oph (Strom & Strom 1994) and Taurus (Strom et al. 1995) were established by color photometry and fitting model tracks of D'Antona & Mazzitelli (1994). The cluster IMF is consistent to that of the solar neighborhood for stars with masses $< 1M_{\odot}$. Comeron et al. (1993) find a monotonically increasing IMF to sub–stellar masses in ρ Oph, also consistent with the solar neighborhood. An alternate method for deriving the distribution of masses in an embedded cluster involves measuring the distribution of stellar luminosities in a statistically significant sample, usually at near infrared wavelengths. Comparisons of the observed K band luminosity function (KLF) to synthesis models that depend on the star formation rate and cluster age can reveal the underlying mass function and star formation history. Lada & Lada (1995) and Greene & Young (1992) model a varying K luminosity function within the ρ Ophiuchi cloud core implying different IMFs or ages throughout this star forming region.

Uncertainties in the extinction and infrared excess within embedded clusters demand a photometrically independent method that can confirm these results, as is available through high resolution spectroscopy.

3.2 Observations and Data Reduction

3.2.1 Selection of the Sample

The observational goal of this study was to observe a sample of YSOs within the A_v = 50 boundary in the ρ Ophiuchi cloud core (Wilking & Lada 1983) . We imposed the following selection criteria to determine our sample: (1) We selected only PMS stars that were labeled as Class I, 1.5, or II by Luhman & Rieke (1999) or Greene & Lada (1996) based on the 2.2–10 μm spectral index using photometry of Greene et al. (1994). (2) We required S/N $>$ 20 within one hour to obtain high resolution spectra (R = 50,000). This resulted in a sample of 18 YSOs with K $\leq$ 8.4 (Table 3.1). Two sources in this magnitude limited sample were excluded because there were no nearby optical stars required for guiding on the KPNO 4–meter.

3.2.2 Spectroscopic Observations

We obtained near infrared spectra of 16 YSOs in Ophiuchus in 2000 May. The positions and alternate source names for the Ophiuchus targets can be found in Barsony et al. (1997). The observations were taken using the PHOENIX spectrograph on the Kitt Peak 4 meter (Hinkle et al. 1998). Spectra were imaged on an Aladdin II InSb detector, 1024 × 256 (used) with 27 μm pixels. We chose the spectral region at 2.21 μm to measure stellar features in low mass stars since this wavelength region has strong photospheric lines in late type stars whose shapes and depths are sensitive to changes in temperature (Kleinmann & Hall 1986).

Centered at 2.207 μm, we obtain 95 Å of spectral coverage. With a $1''$ slit we achieve a resolving power of R $\sim$50,000. $15''$ nods east–west along the length of slit allowed sequential spectra to be taken in two beam positions on the array for removal of background sky. Targets were kept in the slit by guiding on optical stars within the $5'$ field of the CCD off–axis guider. Single on–chip integrations with PHOENIX were 5–25 minutes, resulting in signal–to–noise (S/N) $\sim$40–70 obtained in a single beam subtracted pair. We estimated the S/N in our spectra from variations in the photospherically featureless continuum short–ward of 2.206 μm. Hot stars were observed at the same airmass throughout each night for telluric line cancellation. MK spectral type standards were also observed for comparison in our spectroscopic analysis (§2.4).

Supplementary high resolution spectra (R $\sim$ 21,000) at the (2–0)^{12}CO band-

TABLE 3.1
OPHIUCHUS SURVEY SAMPLE

Source[a]	SED Class	m_J[b]	m_H[b]	m_K[b]	Obs. Date (UT)	approx. S/N
GY20A	II	8.9	7.4	6.4	5/20/00	35
EL24	II	10.2	8.2	6.8	5/20/00	45
GY167	II	9.8	8.3	7.1	5/22/00	25
GY23	II	10.8	8.7	7.2	5/22/00	25
GY319	II	8.5	7.7	7.2	5/20/00	50
SR4	II	9.0	8.0	7.3	5/21/00	55
GY168[c]	II	10.3	8.6	7.4	...	...
GY214	I	17.2	12.0	7.5	5/20/00	75
GY292	II	11.3	9.3	7.9	5/21/00	60
GY110[c]	II	10.7	8.9	8.0	...	...
GSS28	II	9.7	8.7	8.1	5/21/00	45
GSS29[d]	II	11.1	9.2	8.2	5/21 & 22/00	55 & 50
GY6	I	13.9	10.8	8.3	5/22/00	30
GY308	II	11.5	9.6	8.3	5/21/00	35
GY182	1.5	14.1	10.6	7.9	5/20/00	30
GY252	1.5	15.2	11.3	8.4	5/20/00	35
GY314	II	10.8	9.3	8.4	5/21/00	40
IRS2	II	10.5	9.1	8.4	5/22/00	45

[a] Cross reference source names and coordinates are listed Barsony et al. (1997)

[b] Photometry from Barsony et al. (1997)

[c] Not observed due to lack of nearby guide stars

[d] Two observations were made of this source

head (2.2935 μm) of two sources (IRS2 and GY314) were generously provided by Tom Greene, fully reduced from previously published results (Greene & Lada 1997) using the CSHELL spectrograph (Greene et al. 1993) on the IRTF 3–meter. The combination of these two data sets allowed us to make measurements of surface gravities using the combined spectral windows (see §3.4.2).

3.2.3 Data Reduction

All data were reduced using `IRAF`. Source frames at different slit positions were differenced, and then divided by flat fields. The flat field source for PHOENIX was a continuum lamp that fully illuminated the slit. Bad pixels were removed by interpolation. All spectra were optimally extracted using the `apall` package in `IRAF`. Telluric absorption lines (H_2O & CH_4) were used for wavelength calibration, and were removed by division of spectra from hot, early–type stars at the same airmass (within 5° of the target) at each slit position. Final spectra were obtained by combining the extracted, wavelength calibrated pairs from the two beam positions weighted by the differences in the signal.

3.3 Spectroscopic Analysis

We have developed a spectral fitting technique that provides measurements of physical parameters in PMS stars (Doppmann & Jaffe 2002). We utilize information about the line shapes and relative strengths to obtain precise fits of effective temperature, $v \sin i$ rotational broadening, and continuum veiling to spectral synthesis models, and are able to measure surface gravities from the equivalent width ratios between the Na lines at 2.2 μm and ^{12}CO lines at 2.3 μm. Since we compare our spectra to photospheric models with different effective temperatures, we measure $T_{\rm eff}$ directly without introducing uncertainty due to conversion from spectral type. Our best–fit stellar parameters are determined by the position of the minimum in the error space of residuals to the model fits (Fig. 3.2).

3.3.1 Effective Temperature, Rotation, and Veiling

We outline briefly here the technique we have developed for obtaining stellar parameters from high resolution near–IR spectra. Doppmann & Jaffe (2002) discuss details of the technique, its accuracies, and its susceptibility to systematic errors. We utilize a wavelength region in the K band at 2.200–2.210 μm to analyze stellar properties by the behavior of strong temperature sensitive photospheric absorption lines (e.g. Na I, Si I, & Sc I). Generally speaking, as $T_{\rm eff}$ decreases, the Na I lines become broadened and Sc I lines grow deeper, while the Si lines decrease in strength.

For this given wavelength region, we develop a grid of synthetic spectra to compare our data to and determine stellar properties. The synthetic spectra are generated using NextGen stellar atmosphere models (Hauschildt et al. 1999) using the spectral synthesis program `MOOG` (Sneden 1973). The grid of synthesis models covers a range in cool effective temperatures ($T_{\rm eff}$ = 3000–5000K) and PMS surface gravities ($\log g$ = 3.5–5.0). We assume solar metallicity in generating the synthetic spectra for PMS stars, consistant with the results of Padgett (1996), who measures [Fe/H]$= +0.08 \pm 0.07$ for a sample in Ophiuchus (see also the results of Balachandran & Carr 1994). We have therefore computed all models used in analysis of our pre–main sequence target stars with solar metallicity.

An IDL program adds rotational broadening ($v \sin i$ = 4–40 km s^{-1} in steps of 1 km s^{-1}) and near–IR continuum excess (r_K = 0–4.0 in steps of 0.1) to these model spectra and compares each case to the observed spectrum. We assume the IR excess is uniform in intensity across our wavelength interval at 2.2 μm. The best model spectrum is selected by the minimum RMS of the residuals to the fit from selected wavelength sub–intervals that are centered on the Na I lines (see the vertical dashed lines Fig. 3.1).

We start with an assumed gravity of $\log g$ = 3.5, which corresponds to $\sim$1–2 Myr old objects in stellar evolutionary models (Baraffe et al. 1998; Siess et al. 2000; Palla & Stahler 2000), consistant with age estimates of the central embedded cluster in Ophiuchus (Wilking et al. 1989; Greene & Meyer 1995; Luhman & Rieke 1999; Bontemps et al. 2001). We measure effective temperature, $v \sin i$ rotation, and continuum veiling by the best model fit. Finally, the best fit stellar values are found by interpolation within the RMS plane of the parameter space (Fig. 3.2). Figure 3.1 illustrates our spectral fitting technique as it applies to one of the PMS sources in our sample.

3.3.2 Quality of the Model Fits

The random errors in the model fits are small. We estimate these errors based on synthesis models with many independent Gaussian noise seeds (S/N = 30 per pixel, R_{pix} = 240,000) to be ($\pm 1\ \sigma$) T_{eff} = 45K, r_K = 0.04, and $v \sin\ i$ = 1.9 km

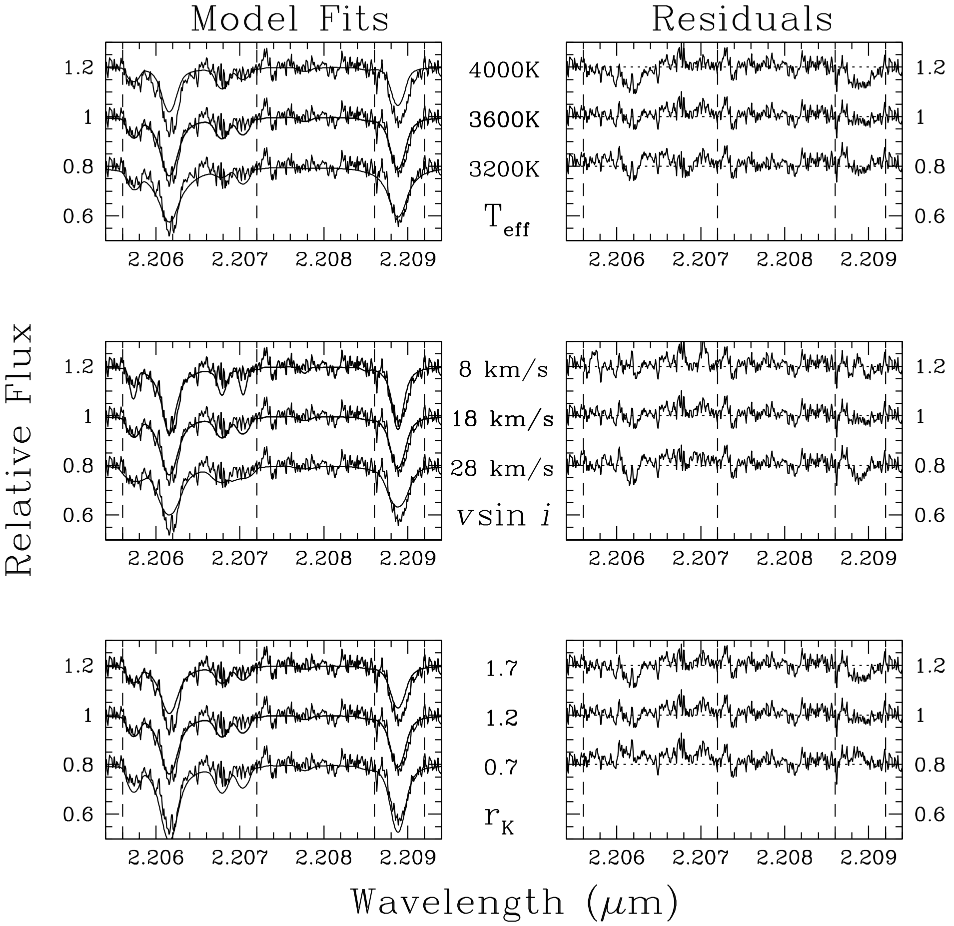

Figure 3.1 Spectral synthesis fits to the observed spectrum of GSS28. The variation of line shapes with different effective temperatures (top left panel), different $v\sin i$ rotations (middle left panel), and different veilings (bottom left panel) is visible. The best fit to each stellar parameter (holding the other parameters constant) is the middle spectrum in each of the three panels. The best fit model corresponds to $v\sin i$ rotation of 18 km s^{-1}, veiling of 1.2, and effective temperature of 3600K. The second set of vertical panels on the right shows the residuals to each fit. The dashed lines indicate the two regions where the RMS of the residuals was computed in each plot.

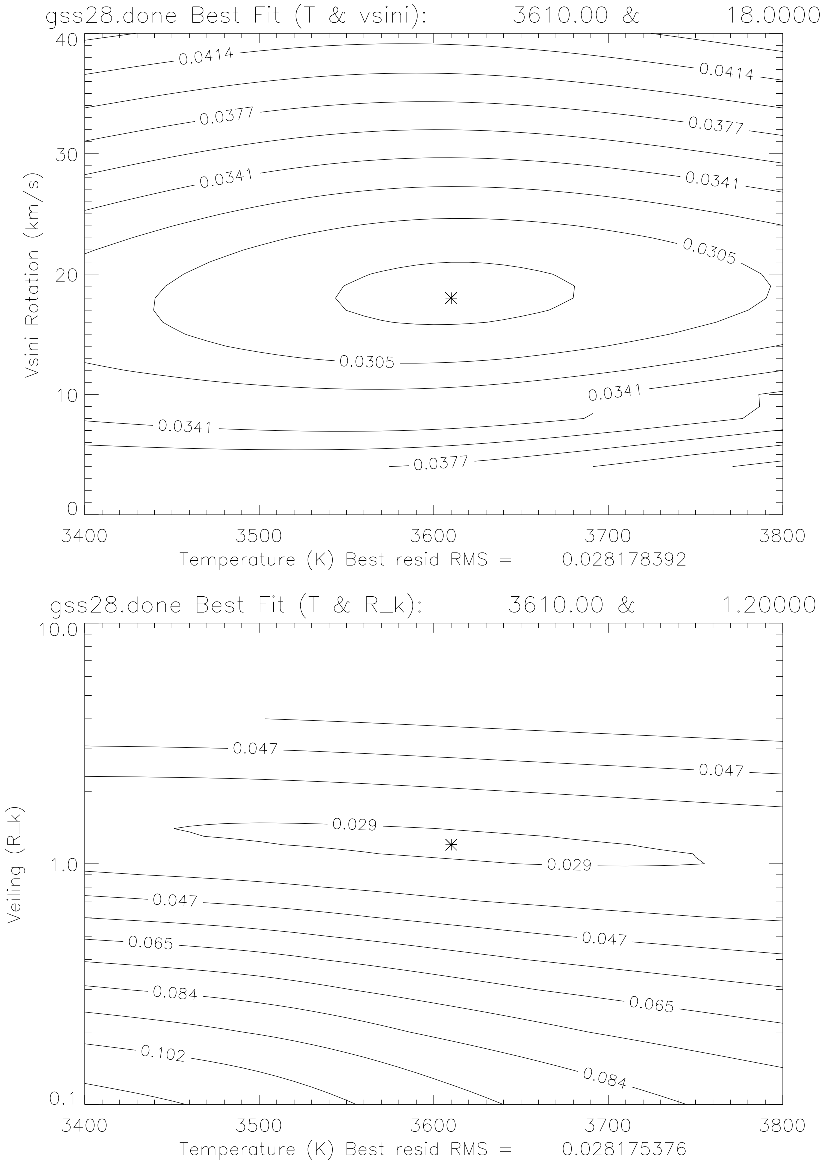

Figure 3.2 We show 2 cuts through the error space illustrating the minimum RMS of the residuals between the observed spectrum of GSS28 and synthesis models varying in $v\sin i$ rotation and T_{eff} only (top) and r_{K} and T_{eff} only (bottom). while $\log g$ is fixed at 3.5. The best fit of the three parameters is found by interpolation to the minimum in each of these two plots. The contours represent the RMS per pixel calculated in the regions of the spectrum where there is significant line flux (see vertical dashed lines in Fig. 3.1).

s^{-1}. At this signal–to–noise, errors in temperature are dominated by systematics effects. Fully resolved photospheric lines in high resolution spectra contain intrinsic line shape information that can minimize degeneracies between the effects of different stellar parameters on the equivalent widths of lines. The minimum RMS values as a function of different combinations of parameters ($T_{\rm eff}$, $v\sin i$, and r_K) defines a solution vector in the parameter search cube that is not always along the principal axes of the cube and indicates the presence of non–orthogonal degeneracies. A degeneracy introduces an uncertainty in temperature with the best fit pairs of $v\sin i$ and veiling in the RMS error space of the residuals to these best fit models, and is accounted for in the errors mentioned above.

There are several ways to minimize these errors. The straightforward solution is to obtain higher signal to noise (S/N) spectra. In practice, a S/N of 60 per pixel will reduce the formal errors above by a factor of $\sim$2.

An alternative is to find techniques that allow independent measurements of the $v\sin\ i$ rotational broadening, such as cross correlation. The width of the correlation function contains the amount of $v\sin\ i$ broadening and magnetic field strength convolved with the intrinsic line width. Therefore, numerous lines that are intrinsically narrow increases the precision for measuring stellar rotation.

For example, the (2–0)^{12}CO line region at 2.2935 μm would be a sensitive diagnostic for rotation using cross correlation because of the the many ascending and descending R–branch transitions, particularly in places where the R branch lines are closely spaced near the bandhead.

If spectral coverage is limited, there is an atomic absorption line of Ti I close to the Na I doublet at 2.2 μm that can be used as a diagnostic of rotation since its shape is insensitive to temperatures between 3000–4000K.

3.3.3 Spectroscopic Determination of Log G

We observe a degeneracy between gravity and temperature ($\pm$167K and $\pm$0.23 in $\log g$) in the best model fits to the Na line interval (see Figure 2.6 in Chapter 3). To break this degeneracy, we use spectra from the ^{12}CO line region (2.2925–2.2960 μm). The strength of the ^{12}CO bandhead is a sensitive luminosity diagnostic in late type stars (Baldwin et al. 1973; Kleinmann & Hall 1986; Ali et al. 1995; Ramirez et al. 1997), however CO is also sensitive, though less so, to changes in effective temperature. We exploit the weak gravity dependence on temperature as a function of the ratio of photospheric line strengths between the Na and CO spectral regions (Fig. 3.3). We find the best temperature and gravity by iterating between the spectral fitting routine and this line ratio technique (Chapter 2).

3.4 Results

Figure 3.4 shows the reduced spectra of all 16 sources we observed in the Na interval. Eleven of 16 sources had detectable (up to 30% below the continuum) photospheric lines (e.g. Na I, Si I, & Sc I) that we could apply our fitting technique to. The derived properties are listed in Table 3.2. One source, GSS29, showed a radial velocity offset ($\sim$20 km s^{-1}) determined from the center of its Na I absorption lines relative to the v_{LSR} of the cloud. We could not fit these lines satisfactorily

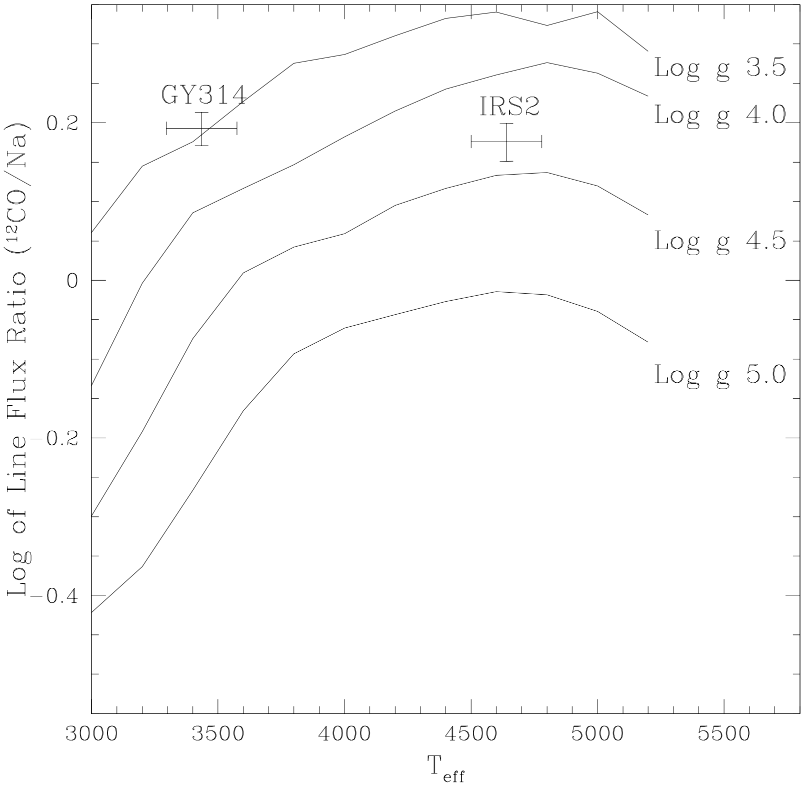

Figure 3.3 Isogravity contours are shown as a function of the ratio of ^{12}CO/Na line flux and effective temperature. Equivalent widths were computed from 2.202–2.212 μm in the Na interval and 2.2925–2.2960 μm in the ^{12}CO interval. We calculate the surface gravity of 2 Ophiuchus sources from their effective temperatures and ratio of photospheric line fluxes measured in two regions at high spectral resolution, scaled to the slope of the observed spectral energy distribution at low resolution. T_{eff} errors are dominated by systematics in fitting observed spectra to the synthesis models ($\pm$ 140K, i.e. one spectral subclass). Errors in the measured line flux ratio are dominated by the determination of the continuum level, a function of signal–to–noise. Surface gravities derived using this technique are independent of uncertainties in the line–of–sight extinction and continuum veiling that are problematic in photometric measurements.

with a single spectral template because of the presence of additional line flux from a second spectral component, marginally detected due to weaker lines from a hotter photosphere, broadened by rapid rotation (Chapter 4). For 8/10 of our sources with fitable lines, we measure cool effective temperatures that are within a narrow range (3400–3700K). The remaining two sources had significantly warmer derived temperatures by $\sim$1000K above the mean of the cooler sources. Spectral types were assigned from the derived temperatures using the Sp-$T_{\rm eff}$ conversion of de Jager & Nieuwenhuijzen (1987). In the 10 sources with good line detections, we see a broad range in stellar rotation ($v \sin i$ = 12–39 km s^{-1}) and continuum excess at K (r_K = 0.3–4.5).

For two sources (GY314 and IRS2), we employ our full fitting technique (§2.2.2) that utilizes both ^{12}CO (2.293 μm) and Na I (2.207 μm) line regions to measure the surface gravity, spectroscopically. The remaining eight sources were assumed to have surface gravities of $\log g = 3.5$, consistent with ages of several Myr in evolutionary models of cool young stars (Baraffe et al. 1998; Siess et al. 2000; Palla & Stahler 2000). Table 3.2 summarizes all the stellar parameters we measured in our Ophiuchus sample.

3.4.1 Luminosities Determined from Photometry

We derive photospheric luminosities for our sources listed in Table 3.1 using the near–IR photometry of Barsony et al. (1997). J band extinction is determined from the J–H colors using the extinction law of Martin & Whittet (1990), our measured stellar temperatures, and the color–temperature relation in Table A5

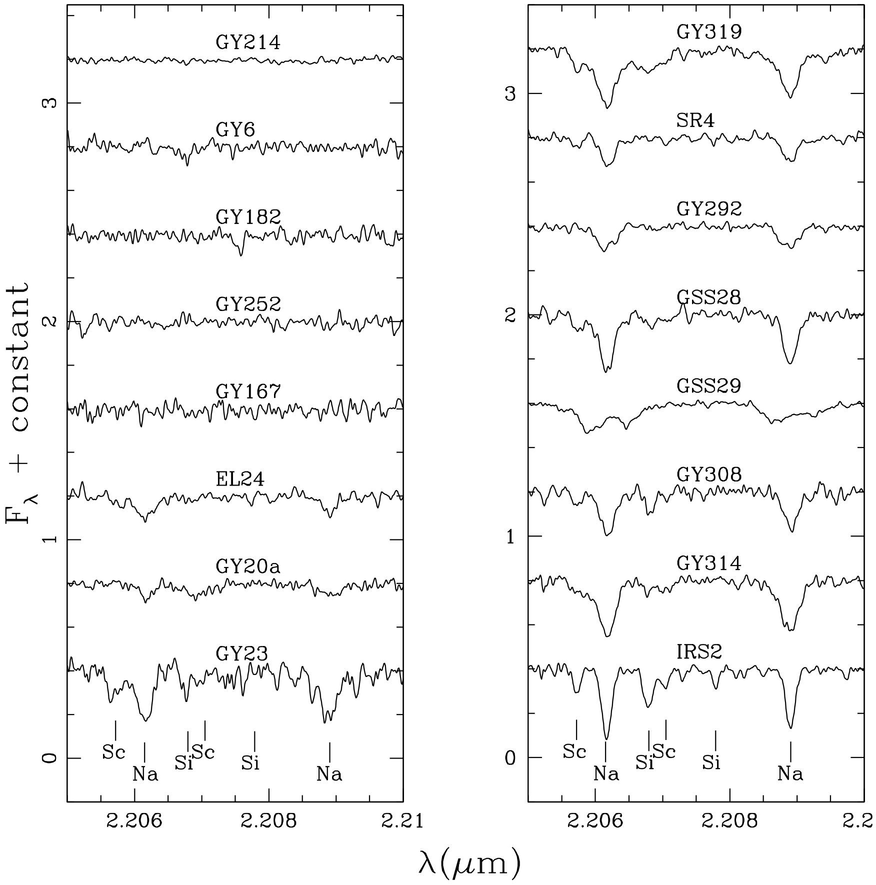

Figure 3.4 K band spectra of Ophiuchus targets observed at high spectral resolution (R=50,000) using the PHOENIX spectrometer on the Kitt Peak 4–meter. The Class I and 1.5 sources (GY214, GY6, and GY252) do not show photospheric features at a signal–to–noise of $\sim$70. GY167 (Class II) is also featureless, though at lower S/N. GY182, reported to be early spectral type (B8–A7) by Luhman & Rieke (1999), does not show evidence of photospheric lines at 2.2 μm. The two strongest absorption features are the neutral Na lines at 2.206 and 2.209 μm.

TABLE 3.2

MEASURED STELLAR PARAMETERS OF YSOS IN ρ OPHIUCHI SAMPLE

Source	$T_{\rm eff}$ (K)[a]	Sp[b]	$v \sin i$ (km s^{-1})	r_K	$L/L_\odot$[c]	$\log g$ (cm s^{-2})[d]
GY319	3410	M3	26	0.9	1.89	3.5
GY314	3435	M3	22	1.1	1.35	3.5[e]
GY23	3490	M2	20	1.2	5.5	3.5
GY292	3500	M2	28	4.0	2.59	3.5
EL24	3520	M1.5	21	4.5	6.17	3.5
SR4	3585	M1.5	14	3.7	2.29	3.5
GSS28	3610	M1	17	1.2	1.18	3.5
GY308	3715	M1	17	1.6	2.03	3.5
IRS2	4640	K4	12	0.3	2.07	4.2[e]
GY20A	4460	K5	39	1.6	11.16	3.5

[a] Errors are ±140K (Doppmann & Jaffe 2002)

[b] Adopting the spectral type–$T_{\rm eff}$ relation of de Jager & Nieuwenhuijzen (1987)

[c] Determined using J & H photometry of Barsony et al. (1997)

[d] Assumed $\log g$ = 3.5 unless otherwise noted

[e] Log g values measured using spectroscopy

of Kenyon & Hartmann (1995), assuming there is no continuum excess at J or H. Using a distance modulus of 5.81 for Ophiuchus (de Zeeuw et al. 1999), we obtain the absolute magnitude at J. We convert to bolometric luminosity using the derived effective temperature from our best model fit to the data and the bolometric correction factor from Table A5 of Kenyon & Hartmann (1995). The bolometric luminosities and effective temperatures are plotted on an HR diagram together with the Baraffe model tracks (Fig. 3.5).

3.4.2 Luminosities Determined from Spectroscopy

For IRS2 and GY314, we were able to determine $\log g$ directly from spectra (§2.2.2). Surface gravity can be used to determine luminosity if the stellar mass is known. We use four different PMS stellar evolutionary models to fit our observations of $\log g$ and $T_{\rm eff}$ to select a unique mass track. Using the relationship between gravity and mass, we can derive a luminosity (equation 3.1).

$$L = 4\pi\sigma G \frac{M T_{eff}^4}{g} \tag{3.1}$$

We convert $\log g$ values for two sources (IRS2 & GY314) into corresponding luminosities using measurements of mass derived from the best fit to four independent PMS evolutionary model tracks (see Table 3.3).

We then plot these luminosities (specific to each evolutionary model) and effective temperatures (derived from our fitting routine) on the HR diagram with the Baraffe stellar evolutionary model tracks (Fig. 3.5).

3.4.3 Notes on individual sources

GSS29: This source was observed twice during our PHOENIX run since it displayed a radial velocity shift of $\sim$ 28 km s^{-1} blue shifted relative to the cloud v_{LSR} of 2.7 $\pm$ 0.5 km s^{-1} (van Dishoeck & de Zeeuw 1984), suggesting it is a spectroscopic binary. The measured radial velocity shift over 24 hours was $\leq$ 2.5 km s^{-1} (2 pixels). This source exhibits broader lines and a bumpy spectrum likely due to the influence of a secondary component, and it was not fit well by any single stellar model spectrum. Further monitoring of this source is being carried out to identify the spectral components and constrain the orbital properties of this system (Chapter 4).

IRS2: We derive a $\log g$ of 4.25 from spectroscopy and using Figure 3.3. When deriving the temperature, rotation, and continuum excess, we use a $\log g$ of 4.0. The model spectra are binned coarsely in steps of $\Delta \log g = 0.5$. We do not interpolate between these two cases since the behavior of the line shapes at 2.2 μm is nonlinear with changes in surface gravity. Instead we select the $\log g = 4.0$ case as the best fit as it corresponds to the lowest RMS in the two $\log g$ cases.

GY182: This source is listed as spectral type B8–A7 based on Brackett line absorptions of hydrogen in the H band observed by Luhman & Rieke (1999) which is in agreement with our observations that do not show evidence of photospheric lines at 2.2 μm.

3.5 Discussion

3.5.1 Cool Derived T_{eff}s

Eight of 10 stars that we have measured temperatures for show a narrow range (σ = 100K) about the mean (3530K). Seven out of eight of these cooler temperature sources have reported temperatures from lower spectral resolution (R = 800–1200) observations of Luhman & Rieke (1999) to which we compare our results. All 7 stars have systematically cooler derived temperatures ($< \Delta T_{eff} >$ = 325K) when compared to the temperatures reported by Luhman & Rieke (1999). They also see a narrow range in their derived temperatures (σ = 50K).

The offset to higher derived temperatures from the lower spectral resolution observations is a systematic effect of degeneracy between veiling and temperature due to the absorption lines being unresolved. For example, at lower spectral resolutions, it is difficult to distinguish between elevated temperatures and reduced veiling in temperature sensitive lines since the line flux remains conserved. Indeed, the veiling measurements derived from lower resolution data (Luhman & Rieke 1999) are systematically lower compared to the values we derive at high resolution from the same sources in ρ Ophiuchi. Our own veiling and temperature determinations are more accurate since the high spectral resolution permits us to utilize the line *shapes* in determining the best fit. This allows us to break the degeneracy between temperature and veiling which persists in lower resolution fits that rely solely on equivalent width information.

3.5.2 Luminosity

Photometric Derivation – Ages from Tracks

The photometrically derived luminosities vs. measured effective temperatures of sources in our sample are shown in Figure 3.5. There is a significant range in luminosity (factor $\sim$5) among the cool temperature sources. Since these young stars are on the convective and primarily vertical portion of their evolutionary tracks, this spread in luminosity could be caused by a large spread in age. Since most of these sources are above the 1 Myr isochrone indicated by the evolutionary models, they are probably coeval to within 1 Myr. However, the location above the youngest isochrone suggests that many of the inferred luminosities are non–physical. One source in our sample (IRS2), had a significantly older measured age (extrapolated to $\sim$5 Myr) than the others suggesting that it is not coeval with the others in our sample. Luhman & Rieke (1999) report a median age of 0.3 Myr for the sources in their larger Ophiuchus sample, using the DM97 tracks (D'Antona & Mazzitelli 1997). This is in loose agreement with the ages of 9/10 of our sources (IRS2 is excluded) which are younger than 1 Myr based on the Baraffe tracks. This is also consistent with age estimates reported by Greene & Meyer (1995) based on their low resolution near IR survey of embedded Ophiuchus sources using DM94 tracks (D'Antona & Mazzitelli 1994).

We compare the luminosities determined photometrically with those determined using our ^{12}CO/Na line flux ratio technique in two of our sources (IRS2 & GY314). In both cases, the photometrically determined luminosities are systematically higher (factor of 3 for IRS2 and factor of 4 for GY314) than the mean luminosity determined by the spectroscopic method described in appendix A. This suggests that the luminosity may be over–estimated and the ages are under–estimated using the photometric method. Interestingly, the ages inferred for IRS2 & GY314 using the models and spectroscopically determined luminosities are older than the photometric ages (by > 3Myr in the case of IRS2). Further, the spectroscopic ages of these two sources are not coeval by $\sim$10 Myr.

Excess Emission in the J band

J band photometry has been used in the past to derive stellar luminosity under the assumption that the accretion luminosity is negligible at 1.2 μm (Kenyon & Hartmann 1995; Luhman & Rieke 1999). However, significant continuum excess ($r_J \sim 1.2$) has been observed in a sample of Classical T–Tauri stars at J in Taurus (Folha & Emerson 1999), causing PMS stars to appear more luminous at 1.2 μm.

To date, there hasn't been a spectroscopic study of ρ Ophiuchi that investigates excess at J and H, even though stellar fluxes and measurements of the extinction in the near–IR are affected by the presence of continuum excess. An elevated flux at J due to unaccounted veiling will drive the derived stellar luminosity up. Furthermore, differing amounts of unaccounted J band excess among sources would explain the spread in photometrically derived luminosities in a sample of low mass PMS that could be coeval.

More veiling at H than J will give the star redder colors causing overestimates in the extinction, also causing overestimates in the intrinsic flux. If the observed J–H colors are representative of the true stellar photosphere, then veiling at J and H would have to be higher ($r_J = r_H = 2.0$ and 3.0 for IRS2 and GY314, respectively) than is derived at K in order to account for the elevated photometric luminosities. Depending on the choice of evolutionary model, the J veiling values could be within a factor of 2 of the average r_J value observed in a sample of classical T Tauri stars in Taurus (Folha & Emerson 1999). There is an intrinsic dispersion ($r_J = \pm 0.45$) in these results which could account for close to half of the observed dispersion in our photometrically derived luminosities.

The origin of any excess at J is not clear. It is unlikely that any significant J excess would originate from thermal emission of dust, since the temperature of the inner edge of the disk would have to exceed the sublimation temperature of the dust ($\sim$2000K) in order to radiate at 1.2μm (Lada & Adams 1992). Instead, the presence of inner disk holes would keep the disk temperatures cool enough permitting thermal emission only at longer wavelengths (Meyer et al. 1997). Alternatively, models of excess emission at J caused by accretion shocks are an order of magnitude smaller than at optical wavelengths (Hartigan et al. 1995). In any case, the veiling at J seen in at least some CTTS (Folha & Emerson 1999) is likely tied to the accretion process in some way.

3.5.3 Dispersion in Derived Luminosities

A. Spectroscopic Luminosities

There is a spread in the derived luminosities in each source (factor of $\sim$2.5 for GY314 and $\sim$1.2 for IRS2, filled symbols in Fig. 3.5) which reflects mass differences due to differences in the input physics (i.e mixing length, model atmosphere, opacities, and initial conditions) of each evolutionary model (Siess et al. 2000; Baraffe et al. 1998; Palla & Stahler 1999; D'Antona & Mazzitelli 1994). While observational tests do not examine the validity of different methodologies or of the physical assumptions made in the models, they do at least test the ability of the models to match real data. We show the Baraffe evolutionary tracks as a reference in Figure 3.5 since our synthetic spectra are based on the NextGen stellar atmospheres, which Baraffe et al. (1998) use in computing their model tracks. Also, uncertainties in model tracks at ages less than 1 Myr are large (Baraffe et al. 2002). We display only the PMS tracks of Baraffe et al. (1998) to compare to the placement of our objects on the HR diagram so as to avoid misleading conclusions about the ages and masses of sources of the younger sources in our sample.

B. Photometric Luminosities

If the spread in derived luminosities is real, then it may be consistent with an intrinsic age dispersion in the cluster. A factor of 5 in luminosity corresponds to a factor of 11 in age (Hartmann 2001) at ∼3500K and ∼0.8 $M_\odot$. However, other effects listed below could plausibly explain the observed dispersion.

1. *Near–IR Photometric Variability–* Temporal variations in the near-IR energy output of a YSO would easily cause a dispersion in the derived luminosities. Barsony et al. (1997) see near-IR photometric variations in some Ophiuchus sources of up to $\Delta m_J = 1.2$. Luhman & Rieke (1999) also see evidence of variability in the continuum emission, though mostly at K, as well as variations in the veiling at K (r_K). In general, photometric variability is greater in the visible than at infrared

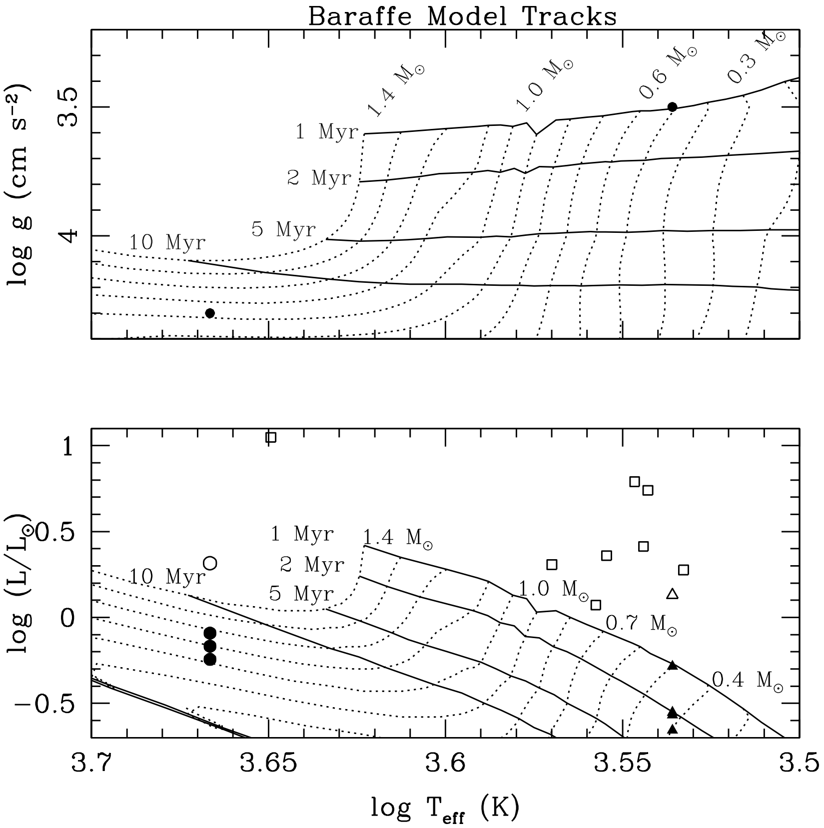

Figure 3.5 Class II PMS objects in Ophiuchus are plotted along with theoretical evolutionary tracks (Baraffe 1998) in both panels. Effective temperatures for all sources were determined using our spectral fitting routine. We measure surface gravities from line flux ratios of ^{12}CO and Na intervals (Fig. 3.3 in IRS2 & GY314 (top panel). Photometrically determined luminosities for ten sources are shown (open symbols in bottom panel) along with the two sources from the top panel with their surface gravities converted to luminosities (filled symbols) using masses derived from the best fits to theoretical evolutionary model tracks. The Baraffe model tracks show IRS2 and GY314 to differ in age by more than a factor of 10 (top panel). In the lower panel, the Baraffe models indicate that 9/10 sources are younger than 1 Myr, with the photometric luminosities systematically higher than spectroscopic luminosities for IRS2 & GY314 (circles and triangles respectively).

wavelengths. Kenyon & Hartmann (1995) find a mean variability of $\sim$0.3 magnitudes at V and $\sim$0.1 at K in a sample of PMS stars in Taurus–Auriga. For a typical class I source that has a rising continuum at 2.2 μm, a change of 0.3 magnitudes at K will induce a change of 0.25 in the derived log gravity.

2. *Unresolved Binaries*– Binaries are common in regions of star formation. In general, multiplicities ($\geq$ 50%) are a factor of $\sim$2 higher than in field stars (Ghez et al. 1993, 1997; Mathieu et al. 2000; Duquennoy & Mayor 1991). Mistaking unresolved binaries for single stars would systematically bias the photometry to higher derived luminosities (factor of $\leq$ 2), introducing some scatter along the vertical axis of the HR diagram.

3.5.4 Class I and 1.5 Sources

We did not detect photospheric lines in any of the Class 1 or 1.5 sources we observed. For the 5 stars that we did not observe absorption lines in, we set detection limits by finding the maximum veiling as a function of $v \sin i$ rotation allowed for at least a 3 sigma detection of the Na lines (see Fig. 3.6) assuming a cool temperature of 3600K. If these stars rotate $\leq$ 50 km s^{-1}, then significant veiling ($r_K \geq 2.0$ for 4/5 sources and $r_K \geq 4.5$ for the other) is needed in order to hide their photospheric lines below a 3 σ detection from the continuum. Sources with heavy veiling will appear brighter and be preferentially selected in a magnitude limited limited sample. Fig. 3.7 does not show any systematic trend of brightness with derived veiling in our sources that had photospheric lines.

One out of the five sources (GY182) was reported to be of early spectral

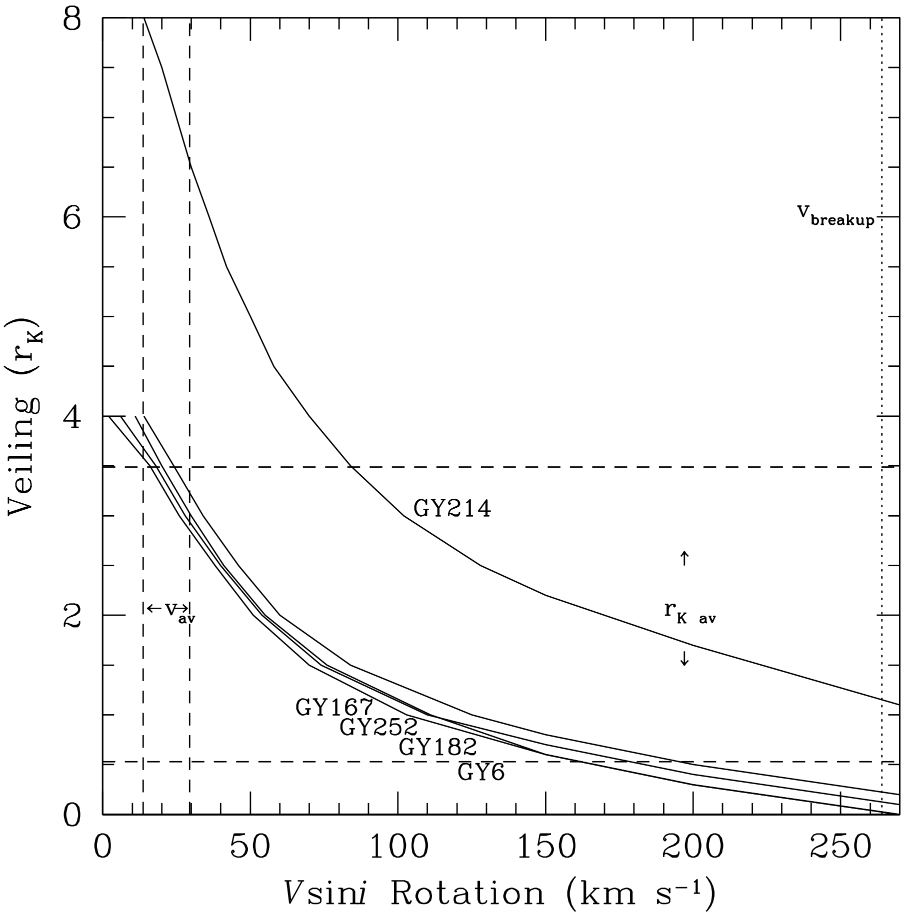

Figure 3.6 We show minimum limits of the stellar $v\sin i$ rotational broadening as a function of continuum veiling (r_K) in our PMS sources that appeared featureless at 2.2 μm. We compare our spectra to stellar synthesis models ranging in $v\sin i$ (0–270 km s^{-1}) and r_K (0–8), but fixed at T_{eff} = 3600K and $\log g$ = 4.0. We find the minimum rotation and veiling values where the RMS of the residuals to the model fits at the Na I line centers (2.2056 & 2.2084 μm) is $\leq$ 3 sigma above the noise in the continuum. We compare these lower limits to the range of measured rotations and veilings in the sources which had detectable photospheric lines that we could model. Arrows show the range ($\pm 1\ \sigma$) in derived rotation and veiling (dash lines) of the Class II sources listed in Table 3.2. The breakup velocity, (dotted line) sets an upper limit to the $v\sin i$ for these objects.

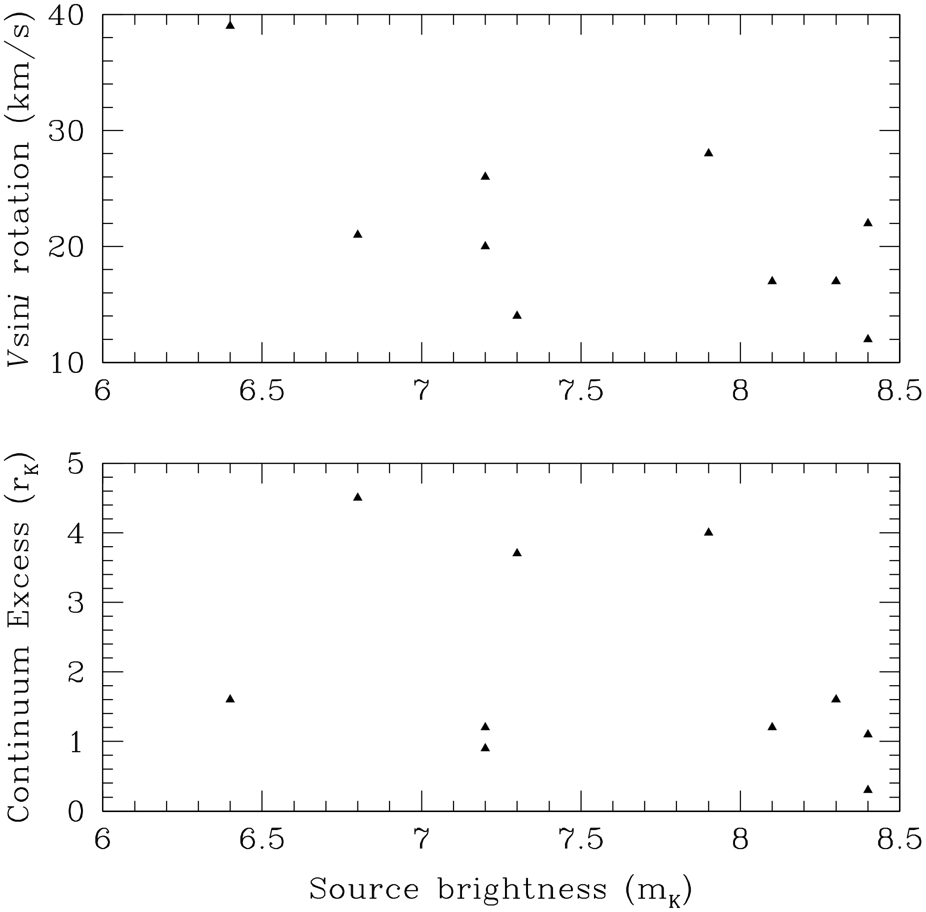

Figure 3.7 We plot the measured $v\sin i$ and veiling vs. the observed magnitude at K to search for a selection effect in the orientation of the disk/star rotation plane.

type (B8–A7), while the remaining others had no reported spectral type by Luhman & Rieke (1999). It is possible than the other sources have no observable K band lines solely because their photospheres are hot. In this case, no veiling or rotation would be required to produce a featureless K band spectrum in hot stars ($T_{\rm eff} >$ 8000K).

Limits on Non Photospheric Spectral Features

We rely on (2–0)^{12}CO equivalent width measurements to determine the surface gravity in objects for which we have high resolution observations in two wavelength intervals (2.2 and 2.3 μm). While ^{12}CO absorption is predicted to occur in the disks of T–Tauri stars (Calvet et al. 1991), only ^{12}CO disk emission has been observed in younger PMS stars (Thompson 1985; Carr et al. 1993; Najita et al. 1996; Luhman & Rieke 1999). So we must avoid using our spectroscopic method on stars that exhibit CO emission. The emission feature may be straightforward to detect, given that high spectral resolution measurements of WL16 show CO emission lines broadened by up to 400 km s^{-1} (Dent & Geballe 1991). However, Carr & Tokunaga (1992), see CO emission from an outflow in the infrared source, SVS 13 with lines that are only 40 km s^{-1} wide. $V \sin i$ broadening in CO absorption lines of some classical T–Tauri stars is consistant with stellar rotation rather than Keplerian motion in a circumstellar disk (Casali & Eiroa 1996). If the origin of CO emission and absorption at 2.2935 μm are from different velocity fields (Keplerian disk vs. stellar photosphere), then at resolving powers of R >10,000, the presence of both components would be detectable in the spectrum. **?**) find good agreement between their $v \sin i$ measurements of resolved ^{12}CO R branch lines in the K band to the rotational broadening measured in the optical. Generally, ^{12}CO emission is rare and only seems to be associated with higher luminosity objects.

Circumstellar Disk Continuum Emission

The non–photospheric emission dominates the observed K band flux for 8/10 of our sources. The derived K band excesses are larger (Δr_{K} = 1–3) compared to low resolution measurements by Luhman & Rieke (1999). We investigate any possible trends of derived veiling with spectral index, disk luminosity, Brackett γ luminosity, and bolometric luminosity (Fig. 3.8). We see a lack of correlation between K excess and mid IR luminosity suggesting that the source of the emission is not due to an infalling envelope which would generate strong mid and far IR emission. Furthermore, we don't see a correlated increase of Br γ emission with K band veiling, suggesting a different origin than the Br γ emission which is believed to come from accretion of disk material onto the stellar surface in columns (Muzerolle et al. 1998). The source of the 2.2 μm emission is likely to be the warmest parts of the disk.

3.5.5 PMS Rotation

How PMS stars interact and evolve with their disks is a controversial issue. The effect of infalling material from the protostellar disk and surrounding envelope will induce spin–up torques on the central star, while the coupling of magnetic field lines between the disk and star provides rotational braking to the star as it locks

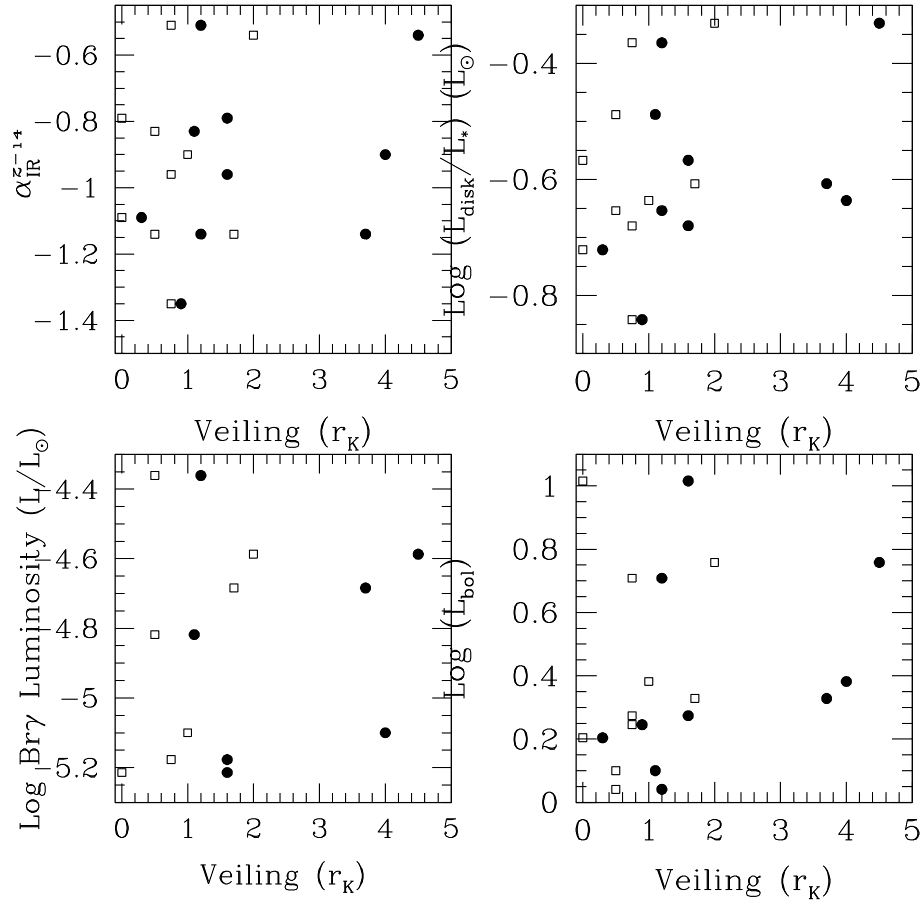

Figure 3.8 Spectral energy index ($\alpha = dlog(\lambda\ F_\lambda)/d\lambda$) derived from 2 and 14 μm photometry (Barsony et al. 1997; Bontemps et al. 2001) are plotted vs. the derived K band excess (upper left), mid IR disk luminosity (Bontemps et al. 2001) relative to stellar luminosity vs excess (upper right), Brackett γ luminosity (Luhman & Rieke 1999) vs excess (lower left), and bolometric luminosity derived from J band photometry vs excess (lower right). In all panels, we show excesses determined from our spectral fitting technique (filled circles) and for the same sources, excesses derived from the lower resolution spectra (open squares) of Luhman & Rieke (1999)

to the lower Keplerian velocity of the inner disk (Shu et al. 1994). When do these mechanisms dominate the evolution of PMS stellar rotation? Edwards et al. (1993) find the presence of a disk (as determined by J, H, K colors) correlated with rotation periods longer than 4 days, whereas stars without disks showed a wide range of rotation periods in their sample of 34 TTS in Taurus. However, no correlation between IR excess and rotation period is seen in a more extensive survey of YSOs in Orion (Stassun et al. 1999), casting doubt on whether magnetic disk locking is a dominant mechanism in angular momentum evolution. But the results of Herbst et al. (2000) maintain the importance of disks in the evolution of angular momentum as they see rotation period weakly correlated with H–K and I–K emission while also anticorrelated with Ca II equivalent width in Orion YSOs ($M > 0.25\ M_{\odot}$).

In the ten Class II sources of our sample, we measure a mean and 1 sigma $v \sin i$ rotation of 21.6 ± 7.9 km s^{-1}. We explore the connection between the physical state of the disks to the measured $v \sin i$ rotation rates of the T–Tauri stars within. In Figure 3.9, we plot our derived rotation values against the (a) bolometric luminosity (from J band photometry, Barsony et al. 1997), (b) mid–IR luminosity (Bontemps et al. 2001), (c) Br γ luminosity (Luhman & Rieke 1999), and (d) our derived K band excess.

We do not see a correlation in any of these plots, suggesting that stellar rotation may not be regulated by magnetic coupling to the disk at least during the T–Tauri evolutionary stage. Nevertheless, the fact that these objects are not rotating near breakup velocities implies that there is something regulating the angular momentum.

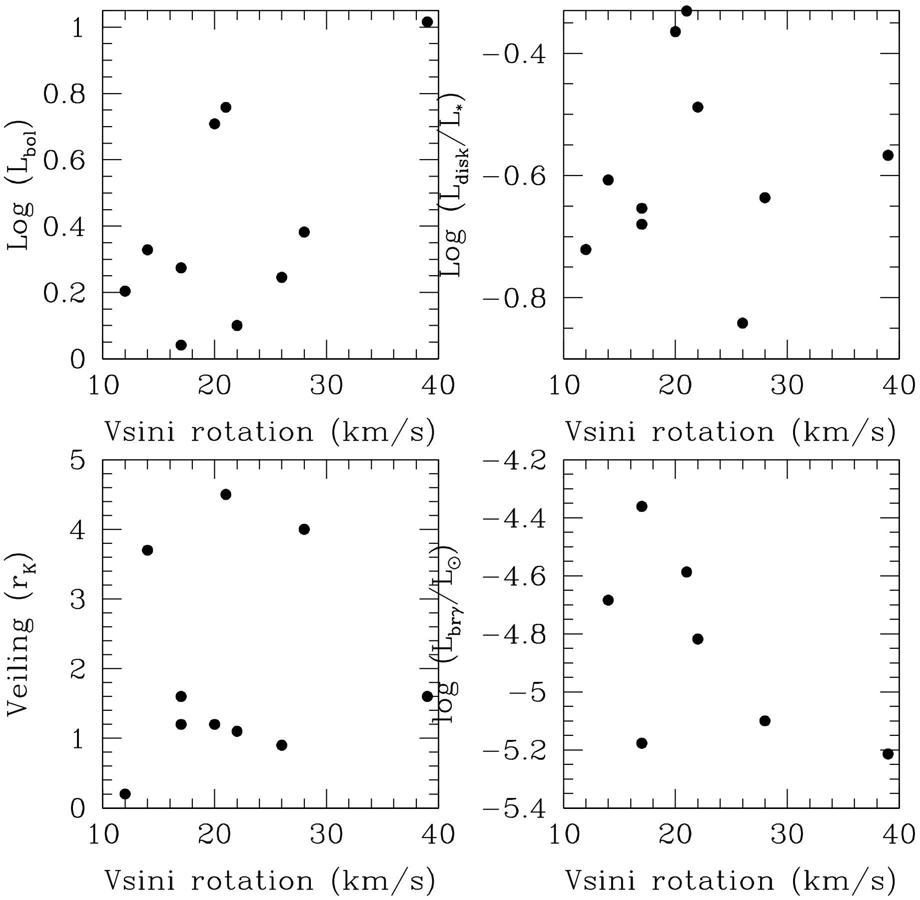

Figure 3.9 Derived $v \sin i$ rotation (1) vs. derived bolometric luminosity from J band photometry (upper right), (2) vs. derived veiling at K from our spectral fitting routine (lower left), (3) vs. the ratio of disk to stellar luminosity from mid–IR observations of Bontemps et al. 1999 (upper right), and (4) vs. Brackett γ luminosity from observations by Luhman & Rieke (1999) (lower right).

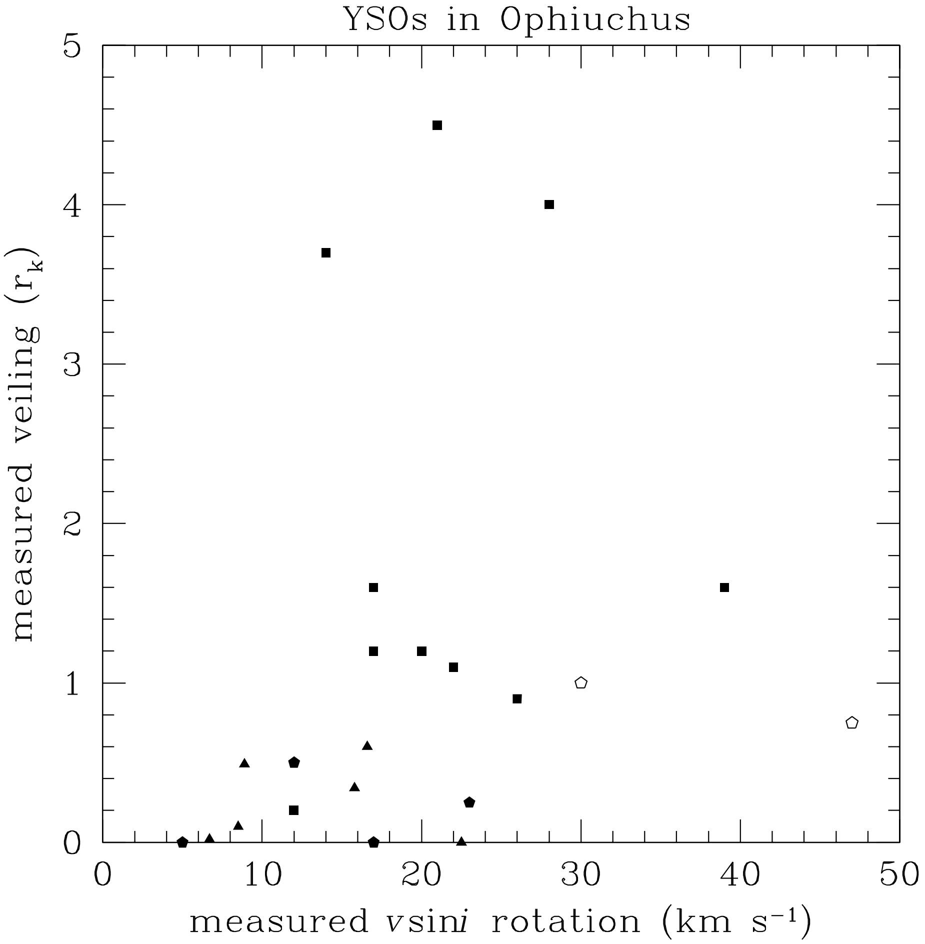

Figure 3.10 Comparison of derived rotation values of sources in ρ Oph. The class II sources from this study are filled squares. Sources from Greene & Lada (1997) are pentagons (open=flat spectrum sources and filled are class II) and r_K values from Luhman & Rieke (1999). The triangles show the measured $v \sin i$ rotation for T–Tauri sources from Bouvier et al. (1986), with corresponding r_Ks estimated from Barsony & Rydgren K photometry

We examine our derived $v \sin i$ results to see if there is a selection effect with the orientation of the rotation plane to our viewing angle. At high inclination angles, we would expect a correlation between sources with more extinction, due to more obscuration through outer disk, and higher rates of rotation. Figure 3.7 does not show any correlation to this effect.

The YSO rotation results from high resolution spectroscopy (Greene & Lada 2000, 1997) imply that embedded protostars (Class 1.5) rotate faster than ones that are older and less embedded (Class II), which suggests the presence of some mechanism that removes angular momentum during this evolution phase. But older YSOs (i.e. Class II, T–Tauri Stars) show a trend where, ones with disks tend to spin slower than ones where the disk is not present, which suggests that the coupling of the star to the disk occurs later in the overall evolution of a YSO.

More observations of photospheric lines over a broad range in PMS evolution are urgently needed to understand how and when the disk affects the stellar rotation.

3.6 Conclusions

We draw the following conclusions from our results.

1. Most of our class II sources have cool derived effective temperatures that fall within a narrow range ($< T_{\rm eff} >$ = 3530K ±100) along with large continuum excesses that exceed the stellar flux at K ($< r_K >$ = 2.3). With high resolution spectroscopy we are able to split the degeneracy between veiling and temperature

TABLE 3.3

MASSES AND AGES OF ρ OPH SOURCES WITH SPECTROSCOPICALLY MEASURED GRAVITIES

Source	BCAH[a]		SDF[b]		PS99[c]		DM98[d]	
	$M_\odot$	Myr	$M_\odot$	Myr	$M_\odot$	Myr	$M_\odot$	Myr
GY314	0.6[e]	$<$1.0	0.32	0.1	0.28	$<$0.5	0.2[e]	$<$0.7
IRS2	$>$1.4	5.0[e]	1.53	3.0	1.52	2.0	0.78	7.0

[a] Baraffe, Chabrier, Allard, & Hauschildt (1998)

[b] Siess, Dufour, & Forestini (2000)

[c] Palla & Stahler (1999)

[d] D'Antona & Mazzitelli (1997)

[e] extrapolated result

which otherwise causes a systematic offset to higher temperatures and less veiling, evident when we compare our results to low resolution fitting techniques.

2. Using a new spectroscopic technique, we derive luminosities of two sources that are significantly less luminous than their photometrically derived luminosities if Zeeman broadening by magnetic fields can be neglected. In this case, their inferred ages are older by Baraffe model tracks. Furthermore, these sources do not appear coeval from their luminosities derived by either photometry or spectroscopy.

3. Our derived $v \sin i$ rotations are substantial ($< v \sin i >$ = 21.6 km s^{-1}) but we see no significant correlations with veiling, Brackett γ luminosity, mid–IR disk luminosity, or bolometric luminosity.

4. We see no correlations between our derived K band veiling values with Brackett γ luminosity, mid–IR disk luminosity, bolometric luminosity, or spectral index.

5. We do not observe any photospheric lines in the class I or 1.5 sources (4 total) we observed at S/N $\geq$ 30, either because they have heavy veiling and/or are rotating rapidly, or have hot ($T_{\rm eff} > 8000$K) photospheres.

Chapter 4

GSS29: Detection and Characterization of a Pre–Main Sequence Binary

4.1 Introduction

The most fundamental stellar property is mass. Mass measurements of Pre–Main Sequence (PMS) stars are essential to our understanding of star formation and the early stages of stellar evolution. How PMS stars evolve toward the main sequence is uniquely determined by their mass. Changes in luminosity and effective temperature as a function of mass and age have been compiled in theoretical stellar PMS evolutionary model tracks. Since these models are largely untested against objects of known mass, independent mass measurements from observations of PMS binaries are essential for validating these theoretical models. In turn, validated models will be able to provide masses and ages for PMS stars based only on observations of their luminosity and effective temperature. The first step requires independent measurements of PMS masses.

Direct measurements of mass can be obtained by observations of stars in binary systems. The amount of mass information in a binary system that is accessible to us depends on the orbital properties that we can observe. Observations of double–line spectroscopic binaries (SB2s) allow us to measure the mass ratio

(M_2/M_1) from the ratio of the orbital velocities relative to the center of mass of the system. If the orbit is eclipsing, then the inclination is known to be edge–on ($i = 90^\circ$) and the individual masses can be determined. In single–line spectroscopic binaries (SB1s), less information is available since the mass of each component (M_1 and M_2) and the inclination angle of the orbit (i) are all inseparable without additional information. If the binary system is resolvable by imaging, then the orbit can be traced along the plane of the sky over time, giving the projected separation of the two components along with the period leading to the sum of their masses by Kepler's 3rd law. Individual masses in binary systems can be measured in cases where the velocity ratio (from SB2s) and maximum separation (from imaging) are observable without knowing the inclination angle. Lower limits to the mass sum are found from observations of SB1s.

4.1.1 Tests of Theoretical Evolutionary Models

The scatter among the different stellar evolutionary models (Siess et al. 2000; Palla & Stahler 1999; Baraffe et al. 1998; D'Antona & Mazzitelli 1997) of PMS stars is because of differences in the input physics. The need to resolve the differences in these models is clear before they can be reliably used to predict masses and ages of PMS stars. Some tests of different model tracks have been carried out using observations of binary systems. For example, observations of the GG–Tau quadruple system (White et al. 1999) has resulted in masses and coeval ages (1.5 Myr) that are best fit by the Baraffe evolutionary models. Analysis of the eclipsing binary, RXJ 0529.4+0041 (Covino et al. 2000), are also best fit by the Baraffe models with these masses (1.25 $M_\odot$ and 0.91 $M_\odot$) at coeval ages. Similarly, the age and component masses have been measured for HD 98800, a young quadruple system, also using the Baraffe models (Prato et al. 2002). Direct measurements of masses in the Taurus binary system, NTT 045251+3016, were made from combined spectroscopic and astrometric observations (Steffen et al. 2001). No inconsistency was found in any of the four sets of stellar evolutionary model tracks when compared to the measured masses and assumed coevality of this system.

4.1.2 Advantages in the Near–IR

A search for binary systems at infrared wavelengths offers the advantage of being more sensitive to heavily embedded young stars. In cluster cores, like ρ Ophiuchi, the extinction is high ($A_V = 40 \pm 10.9$ magnitudes, Luhman & Rieke 1999), making many of the stars invisible or extremely faint in the optical. With less extinction in the K band ($A_K \sim 1/12\ A_V$), more systems will be detectable at 2.2 μm than at shorter wavelengths. Observations of stars within the cores of star forming clusters allows us to probe regions where stars are still forming, enabling measurements of the physical conditions of young stars in dense environments.

Another advantage of the near–IR is that the detectability of SB2s is higher. Brightness ratios ($f_{\mathrm{secondary}}/f_{\mathrm{primary}}$) of binaries at 2.2 μm are closer to unity than in the optical (0.5μm), increasing the chances for detecting the secondary component if the primary is detected. Secondary components in binary systems will be cooler if they have less mass than the primary, assuming the components are coeval (e.g. Baraffe et al. 1998). At temperatures between 3000K and 5000K, the infrared emission from both stars occurs on the Rayleigh–Jeans side of the blackbody curve, whereas at optical wavelengths, the emission from the cooler star is substantially less compared to the primary because of the flux is dropping exponentially on the Wien side of the blackbody curve (Fig. 4.1).

4.1.3 Frequency of Binaries

The dominant stellar population in many star forming regions (SFRs) is in binary or multiple systems. The measured companion star fraction (CSF) is $\geq$ 0.50 based on surveys of low mass PMS stars in Taurus, Ophiuchus, Chamaeleon, Lupus, and Corona Australis, covering a separation range of 15–1800 AU (Ghez et al. 1997; Simon & Prato 1995; Ghez et al. 1993; Richichi et al. 1994; Leinert et al. 1993). Taurus, a site of more distributed star formation, has the highest companion star fraction (0.58 $\pm$0.08, Ghez et al. 1997) of all SFRs surveyed to date. Even though Taurus is the best studied SFR for low mass stars (T–associations), it is not clear whether Taurus is typical with respect to the formation of binaries. The question of how much the environment (clusters vs. loose associations) affects the production of binary systems remains unanswered.

Interestingly, the observed CSF in SFRs mentioned above is about a factor of two higher than in nearby solar type stars (CSF$= 0.26 \pm 0.04$, Duquennoy & Mayor 1991). In contrast, the binary fraction of PMS stars in the Orion Trapezium Cluster is found to be equal or deficient compared to the solar neighborhood (Prosser et al. 1994; McCaughrean 2001). A comparable binary frequency to the solar neighborhood is also observed in studies of other clusters (IC348 and Pleiades,

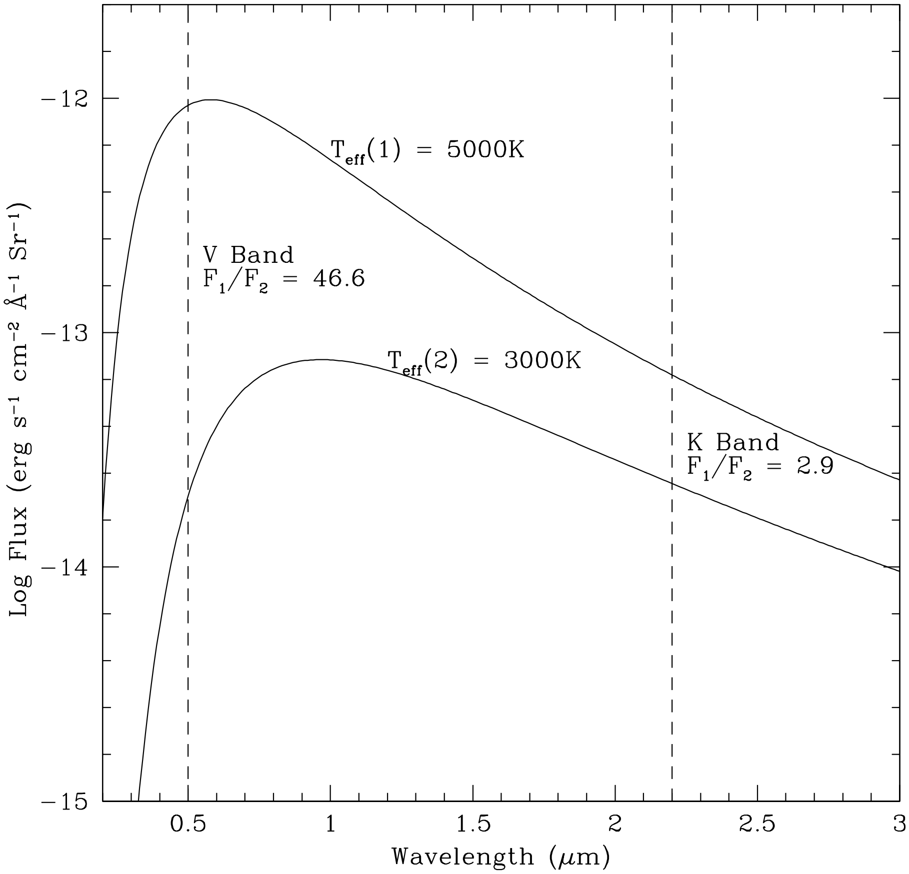

Figure 4.1 Blackbody curves of a primary (modeled at T_{eff} = 5000K) and secondary (modeled at T_{eff} = 3000K). At optical wavelengths (λ = 0.5 μm), the flux ratio is substantially higher compared with observations made at 2.2 μm (K band). Flux ratios that are closer to unity in the near–IR aid in the detection of faint secondary companions that are close to their brighter primaries. Also, the absolute flux is greater at 2.2 μm than 0.5 μm for cool secondaries ($T_{eff} \leq$ 3000K)

Duchêne et al. 1999; Bouvier et al. 1997).

Orbital Eccentricities

Intrinsic orbital properties, such as the eccentricities in nearby open clusters have been examined in a study of 33 solar mass, main sequence spectroscopic binaries. Mayor & Mermilliod (1984), found a critical period below which all binaries had circular orbits. At periods above the cutoff value, a gaussian distribution of eccentricities was observed. The observed cutoff is explained by a tidal circularization theory (Lecar, Wheeler, & McKee 1976) that predicts eccentric short period binary orbits will circularize over time. The relation between binary period, eccentricity, and age has been employed to determine the age in older clusters (i.e Hyades, Praesepe, and M67, Mathieu & Mazeh 1988). In younger clusters, only very tight binaries will have had time to circularize, and resolution of such binaries demands spatial resolution that surpasses our capability. Therefore, little is known about the eccentricity vs. period in short period binaries.

Binary Separations

In a large survey of binary systems in the solar neighborhood, Duquennoy & Mayor (1991) found the distribution peaked at orbital separations of $\sim$30 AU. Even at the distance to the closest SFRs ($\sim$145 pc), direct imaging techniques cannot resolve separations closer than $\sim$70 AU (with $0.''5$ seeing). However, speckle imaging can detect binaries with angular separations down to the telescope diffraction limit (Ghez et al. 1997), or $\sim$10 AU at 145 pc on a 10–m telescope at 2.2 μm. Currently, the highest angular resolutions are achievable by lunar occultations (Simon et al. 1992), and can reach $\sim 0.\!''005$ at 2.2μm, which is $\sim$0.7 AU at the distance to Taurus (Elias 1978b) and Ophiuchus (de Zeeuw et al. 1999). Both speckle and lunar occultation imaging techniques are able to overlap with spectroscopic techniques in detecting and characterizing PMS binaries in some of the closest SFRs, making possible precise determinations of protostellar masses.

At present, the absolute ages of PMS stars can only be measured by comparing their temperature and luminosity values to theoretical evolutionary models. Previous estimates using photometry to obtain the stellar luminosity in Taurus have been biased toward higher luminosities from the combined light in unresolved binary systems, resulting in a bias toward younger ages inferred by model tracks (Simon et al. 1992). For a flux ratio of 2, a star will appear 1.5 times more luminous, which corresponds to a decrease of $\sim$1 Myr in age (from 2 Myr) for 3800K and 1 $L_\odot$ PMS stars (Baraffe et al. 1998). The peak of binary separations in Taurus and Ophiuchus ($\sim 0.\!''3$) causes many close binary systems to go undetected in direct imaging surveys. Speckle and lunar occultation imaging techniques are required to remove this bias toward younger ages inferred from photometry.

The median age of PMS stars observed in the ρ Ophiuchi dark cloud is 0.3 Myr based on a near–IR spectroscopy survey (Greene & Meyer 1995). Models of the luminosity function in Ophiuchus based on a larger spectroscopic sample are in close agreement showing a peak at 0.4 Myr (Luhman & Rieke 1999). The younger median age in Ophiuchus based on these surveys (compared to Taurus YSOs) is less that the average disk survival timescale of 3 Myr (Strom et al. 1988), implying that most of the Ophiuchus YSOs should have circumstellar disks.

Mathieu et al. (1989) reports the discovery of six spectroscopic binaries in Taurus in a sample of Naked T–Tauri Stars (NTTS) at optical wavelengths (5000 Å). More recent work by Prato et al. (2002) has used high resolution near infrared spectroscopy to search for fainter secondary components in previously identified single line binary systems (SB1s). The smallest mass ratio ($M_2/M_1 = 0.18$) PMS binary to date has been identified by this search (Prato et al. 2002) using a cross correlation search technique with spectral template standards (Prato 1998; Mazeh et al. 2002).

4.2 Observations

4.2.1 Experimental Design

Our observational goal is to discover more short period binaries in SFRs and determine relative masses from their double–line spectra or set limits on the masses of the primaries from single–line observations. While all of the sources in our magnitude limited sample do not have companions ($m_K < 14$) with large separations ($\geq$ 400 AU), resolvable by the Barsony et al. (1997) survey, they could be in short period binary systems detectable only by spectroscopic techniques. Though many of our sources have been studied with low to moderate resolution spectroscopy (Luhman & Rieke 1999; Greene & Lada 1996), there has not yet been a search for binaries at high spectral resolution in the Ophiuchus cloud in the near–IR. With precision radial velocity measurements at 2.2 μm, we can detect systems that have separations $<$ 1 AU at distances to Taurus and Ophiuchus, which can not be resolved by imaging even with lunar occultation techniques.

Not only will our high spectral resolution survey permit detections of SB2s, but will also give us statistical information on the frequency of close binaries in a single epoch.

4.2.2 Ophiuchus Survey

We obtained near infrared spectra (2.2 μm) at high resolution ($\lambda/\Delta\lambda$ = 50,000) of 16 PMS stars in the ρ Ophiuchi dark cloud using the PHOENIX spectrometer (Hinkle et al. 1998) on the Kitt Peak 4 meter. The 2.2 μm spectral region was chosen due to the presence of several strong photospheric lines in late type stars (Kleinmann & Hall 1986) that can reveal small ($\geq$ 2 km s^{-1}) radial velocity shifts. Eleven of 16 sources we observed displayed stellar absorption lines that we could use to determine radial velocities. The PHOENIX detector is an Aladdin II InSb detector (1024 $\times$ 256) with a pixel dispersion of $\Delta\lambda$ = 0.09Å = 1.25 km s^{-1}.

4.2.3 Selection of Sample

We chose as a sample all sources with ($m_K < 8.4$) within the A_V = 50 cloud core of ρ Ophiuchi (Wilking & Lada 1983), selected in the following way: (1) Only PMS stars classified as Class I, 1.5, or II by Luhman & Rieke (1999) or Greene & Lada (1996) based on the 2.2–10 μm spectral index using photometry of Greene et al. (1994), and (2) Bright enough to reach $S/N > 20$ within one hour. Two sources in the sample were excluded because there were no nearby optical stars required for guiding on the KPNO 4–meter.

4.3 Results

4.3.1 Discovering PMS Binaries in a Single Epoch

Since the formation of stars takes place within dense molecular clouds, we would expect YSOs in clusters that are embedded within such clouds to be kinematically associated with the gas there. A typical molecular cloud has narrow molecular lines (2–4 km s^{-1}), indicating that the cloud is bound given its typical mass (2–3 $\times$ 10^5 $M_\odot$) and size (50–100 pc) (Lada 1999). It is not surprising that the young stars within these clouds display relatively small velocity dispersions. For example, Hartmann et al. (1986) find low radial velocity dispersions ($\lesssim$ 1.5 km s^{-1}) in their sample of T–Tauri stars relative to the associated molecular gas in Taurus and Orion.

Our spectra were wavelength calibrated using telluric H_2O and CH_4 absorptions present in this 2.2 μm spectral window. These topocentric radial velocities were converted to heliocentric velocities and then to the velocity frame of the local standard of rest. All of the sources in our sample except for one (GSS29) showed small deviations about the mean radial velocity (v_{LSR} = 3.87 km s^{-1}), which was determined from all our May 2000 sources excluding GSS29. The 1 σ_{rv} dispersion about the radial velocity mean was 1.66 km s^{-1}, aiding our search for binary systems in the ρ Ophiuchi dark cloud. (Table 4.1). As a result, the discrepant radial velocity of GSS29 (-24.49 km s^{-1}) made it easily identifiable as a binary system in this first epoch.

The random errors in our radial velocity measurements are small (σ_{err} = 0.48 km s^{-1}) compared to the observed velocity dispersion we measure in the Ophiuchus sample. The random errors were estimated using a synthetic spectrum with $T_{\rm eff}$ = 3600K, $\log g$ = 4.0, $v \sin i$ = 25 km s^{-1}, and r_K=1.0 with Gaussian noise added (S/N = 45 per R=50,000 bin). The best velocity shift of this noisy spectrum was measured using our standard fitting technique (see Chapter 2). The procedure was repeated for many (∼100) noise seeds to establish the error in the best fits to the data. The mean S/N of the objects in Table 4.1 was S/N = 44. Cross correlating a noiseless synthethic spectrum with a model spectrum that had Gaussian noise (S/N = 45) gave comparable random errors to the fitting technique we use for measuring radial velocities.

Excluding GSS29, the largest deviation from the mean is GY23 (2.3 $\sigma_{\rm rv}$). This source had the lowest S/N of all the targets observed in our sample (S/N = 25) causing it to have a slightly higher uncertainty in its radial velocity determination ($1\sigma_{\rm err} \approx 1$ km s^{-1}) as compared to others in our sample.

4.3.2 Multiple Epochs

This experiment was designed to detect binaries in a single epoch, with follow–up observations at later epochs. We carried out follow–up observations of GSS29 since its radial velocity offset of ∼20 km s^{-1} relative to the mean velocity of the other stars within the ρ Ophiuchi dark cloud revealed its binary nature in the first epoch (21 & 22 May 2000). Observations at four more epochs have been made to place constraints on the orbit and characterize the properties of both components (Table 4.3).

TABLE 4.1

MEASURED RADIAL VELOCITIES IN ρ OPHIUCHI

PMS Star	UT Date	UT Time	v_{topo}[a] (km s^{-1})	v_{LSR} (km s^{-1})	v_{LSR}[b] (km s^{-1})
GY20A	20 May 2000	06:40	-9.0	6.4	3.3
EL24	20 May 2000	07:30	-11.5	3.8	3.7
GY23	22 May 2000	09:45	-13.9	0.1	…
GY319	20 May 2000	08:25	-11.5	3.8	…
SR4	21 May 2000	07:40	-9.0	5.7	3.8
GY292	21 May 2000	06:00	-12.3	2.8	4.1
GSS28	21 May 2000	06:50	-10.6	4.2	3.3
GY308	21 May 2000	09:25	-10.6	4.1	3.8
GY314	21 May 2000	10:20	-10.6	4.0	…
IRS2	22 May 2000	06:35	-10.6	4.2	2.9
GSS29	21 May 2000	08:10	-39.2	-24.5	2.7
GSS29	22 May 2000	08:35	-40.0	-25.9	2.7

[a] Our uncertainties are ±0.5 km s^{-1} based on random errors in the observed spectra (typically S/N ∼30)

[b] (3–2) HCO^+ gas measurements made from the CSO on 29 June 2000 toward the corresponding stars (Marsh, private communication).

TABLE 4.2
SINGLE EPOCH DETECTION PROBABILITY FOR SPECTROSCOPIC ORBITS

(M_2/M_1)	AU	(mas)	$v \sin i_{\max}$ (km s^{-1})	Detectability
1	0.62	4.34	16.8	95.0%
0.67	0.58	4.06	12.6	91.8%
0.5	0.56	3.92	16.8	90.4%
0.4	0.51	3.57	8.5	81.9%

NOTE.—Values are calculated assuming an orbital period of 200 days, an inclination angle of 60°, and a minimum mass for the primary (M_1) of 0.6 $M_\odot$.

4.3.3 Limits set by Single Epoch Observations

Single epoch observations cannot distinguish between single stars and binary systems that happen to be at a low radial velocity orbital phase. Table 4.2 shows the likelihood of detecting binary systems as a function of orbital phase. For orbital periods of 200 days, the likelihood that the phase is such that the primary has a radial velocity of $>$5 km s^{-1} ($>$3 σ_{rv} of the measured velocity dispersion in ρ Ophiuchi) is listed in the last column. Assuming an orbital inclination of 60° and a minimum primary mass of 0.6 $M_\odot$, there is a greater than 80% probability that binaries with mass ratios greater than 0.4 will be detectable in a single epoch.

Additional epochs may be required to rule out the possibility of binarity in the other stars listed Table 4.1 if they have mass ratios (q) $<$ 0.33.

4.3.4 Systemic Velocity of ρ Ophiuchi

The mean radial velocity of the stars in Table 4.1 (3.87 km s^{-1}), excluding GSS29, is consistent with the radial velocity of dense gas in the ρ Ophiuchi dark cloud. Martin-Pintado et al. (1983) measure the radial velocity of high density molecular gas in the ρ Ophiuchi cloud and find a mean $v_{LSR} = 3.6 \pm 0.1$ km s^{-1} from H_2CO and NH_3 lines at cm wavelengths. Marsh (2000, private communication) took HCO^+ J=3–2 spectra toward many of our targets and found a mean $v_{LSR} = 3.4 \pm 0.5$ km s^{-1} (see Table 4.1), consistent with the earlier gas measurements and our stellar radial velocities (except for GSS29). We adopt $v_{LSR} = 3.5$ km s^{-1} as the systemic velocity of the ρ Ophiuchi dark cloud.

4.3.5 Constraining the Orbit

The binary nature of GSS29 is unmistakable by the radial velocity shifts of the dominant spectral line component. We have detections of the dominant component of GSS29 at 5 distinct epochs. We measure the topocentric velocities by fitting spectral synthesis models to each observation using telluric lines for calibrating the observations to the topocentric frame of reference. Corrections to the heliocentric frame were made using the IRAF routine `rvcorrect`.

Converting to the local standard of rest for this region of the sky, we obtain velocities in Table 4.3. We fit a velocity curve to these 6 data points using a reduced chi squared algorithm (McArthur, private communication). Solutions converged when the eccentricity and systemic velocity were fixed at 0 (circular) and 3.5 km s^{-1}, respectively. We determine the best fit orbital velocity amplitude ($v_2 \sin i =$

TABLE 4.3

MEASURED RADIAL VELOCITIES FOR GSS29

Epoch (UT)	MJD (UT)	v_{topo} (km s^{-1})	v_{LSR} (km s^{-1})	error (km s^{-1})
21 May 2000	51685.3333	-39.2	-24.5	3
22 May 2000	51686.35764	-40.0	-25.9	3
12 Jul 2000	51737.1875	9.7	0.4	7
01 Feb 2001	51941.5313	-29.6	7.8	5
13 Jun 2001	52073.375	5.1	8.6	4
10 Jul 2001	52100.2368	2.1	-6.1	4

29.0 km s^{-1}) of the dominant spectral component and the orbital period (P = 145d) of the system (See Fig. 4.2).

4.3.6 Characterizing the Binary System

GSS29 is detected as an SB1 in all epochs. Using Kepler's third law, and the information from the radial velocity shifts of the single line component we are able to set a lower limit on the mass sum.

$$(M_1 + M_2) = \frac{a^3}{P^2 sin^3 i} \tag{4.1}$$

The masses are in solar units, a is the orbital separation in AU, P is the period in years, and i is the inclination of the orbit. The velocity amplitude of one orbital component sets a minimum to the orbital separation, if it is the more massive component:

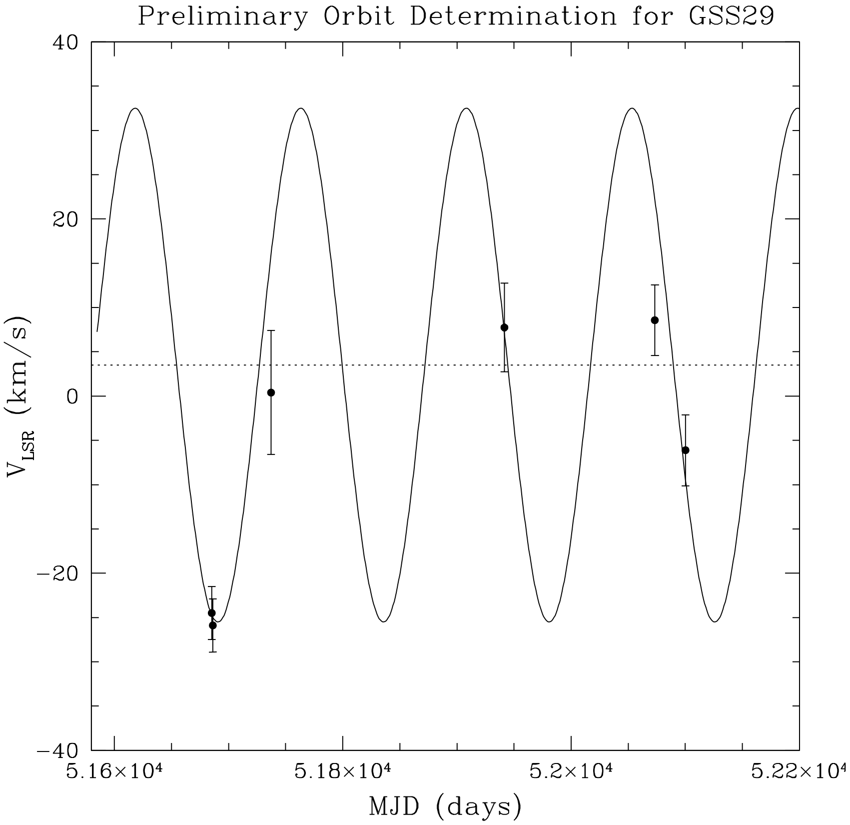

Figure 4.2 The best fit orbit to the radial velocity shifts in the photospheric lines at 2.2 μm measured in 5 different epochs. There are 2 data points in May 2000 separated by 24 hours in time. The derived period is 145 days with a circular orbit. The amplitude of the velocity relative to the orbit center of mass is 29 km s^{-1}. The horizontal dotted line shows the systemic velocity of the cloud (v_{cloud} = 3.5 km s^{-1}) based on the mean radial velocities of the single systems observed in ρ Ophiuchi, which is in agreement with the radial velocities of the dense gas. The center of mass of the GSS29 orbit is assumed to be at the systemic velocity of the cloud (V_{cloud}).

$$a = \frac{Pv_1 \sin\, i}{2\pi}(1 + \frac{1}{q}) \tag{4.2}$$

$$q = \frac{M_2}{M_1} \tag{4.3}$$

If the SB1 is the less massive component, then the derived separation (a) is a *maximum* for a given inclination angle:

$$a = \frac{Pv_2 \sin\, i}{2\pi}(1 + q) \tag{4.4}$$

In the first case (eqn. 4.2), the minimum mass sum occurs when the two individual masses are of equal value (i.e. q=1) and the orbit is exactly edge on (inclination angle = 90°). For GSS29, this lower limit case gives an orbital separation of 0.77 AU and a mass sum of 2.9 $M_\odot$. Since this corresponds to a minimum mass of 1.45 $M_\odot$ for the primary, we can conclude that the dominant spectral component in the observed GSS29 spectrum must be less massive than the other component because of the presence of late type stellar absorption features indicating a cooler effective temperature ($T_{\rm eff} < 6000$K, Fig. 4.3). In particular, the Na I lines are stronger than the Si line at 2.2063 μm in all epochs (Fig. 4.4). We refer to the dominant spectral component observed in GSS29, hereafter, as the secondary since it must have less mass that the hotter component. Consequently, we use eqn. 4.4 to constrain the orbital properties of the GSS29 system.

Using the derived period and radial velocity amplitude of the secondary, we derive the mass function of the orbital system. Substituting eqn. 4.4 into eqn. 4.1,

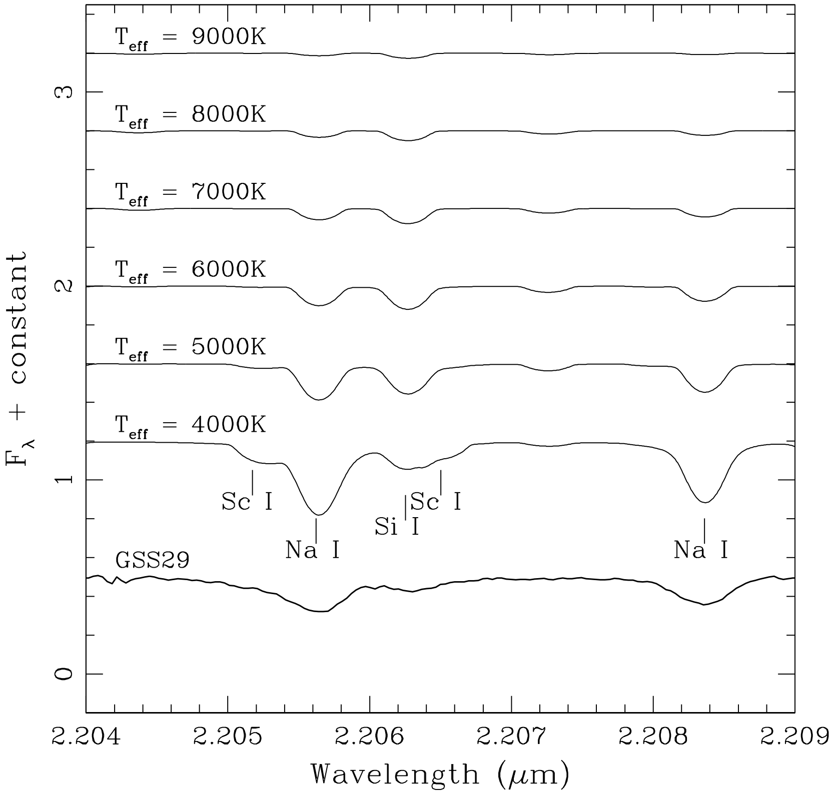

Figure 4.3 Sequence of K band photospheric absorption lines at 2.2 μm with effective temperature. These synthetic spectra all have $\log g$ = 4.0 and have been smoothed to R = 50,000 with $v \sin i$ rotation added (30 km s^{-1}). The absorbers in this spectral window are solely neutral atomic species with the strongest 5 lines labeled. In general, as the photospheric temperature increases, the line flux diminishes to zero as the rate of ionization increases. At cooler temperatures ($<$ 6000K) the Na lines are the strongest and the Sc lines are present. Above 6000K, the Si line becomes the dominant absorber, as all lines fade into a featureless continuum. The spectrum of GSS29 is dominated by sodium lines in all five epochs, implying that the dominant spectral component is cooler than 6000K.

gives an expression of the stellar mass of GSS29 (left hand side) in terms of the observable quantities (right hand side).

$$\frac{M_1^3}{(M_1+M_2)^2} = \frac{P}{\sin^3 i}\frac{(v_2 \sin\ i)^3}{(2\pi)^3} \tag{4.5}$$

The subscripts 1 and 2 refer to the primary and secondary stars, respectively. The masses (M) are in solar units, the orbital period (P) is in years, and the velocity (v) is in AU yr^{-1}.

4.3.7 Modeling a 2 Component Spectroscopic Binary

Spectral synthesis models were generated by MOOG (Sneden 1973) using the NextGen (Hauschildt et al. 1999) stellar atmosphere models (see Chapter 2). The secondary (cooler) component was fit with models ranging in temperature between 3000–5000K, $v \sin i$ = 0–60 km s^{-1}, but with no continuum excess (veiling). The absorption lines of the secondary will be diluted by the additional continuum flux from the hotter (and mostly featureless) primary, which will have a similar effect as the addition of continuum excess caused by thermal emission from a circumstellar disk.

4.4 Discussion

GSS29 was observed at 2.2 μm by Simon et al. (1995) during a lunar occultation, with no detection of its binary companion down to $0.''0058$. The binary separation we derive for GSS29 is 0.58 AU = $0.''0041$, which lies below the detec-

TABLE 4.4

DERIVED PROPERTIES OF THE GSS29 BINARY SYSTEM

	Period = 145 days[a]		Separation = 0.57 AU[b]		
Component	$T_{\rm eff}$ (K)	$\mathrm{flux}_{2.2\mu\mathrm{m}}$[c]	$v \sin i$ (km s^{-1})	r_K	$M/M_\odot$[d]
Primary	5600	3.6×10^{-13}	60	0	1.05
Secondary	4000	2.2×10^{-13}	40	0	0.7

[a] Determined from the best fit orbital solution based on radial velocity shifts of the secondary in 5 epochs (Fig. 4.2)

[b] Determined by the measured period using equation 4.4 and assuming q = 0.7 and i = 60°

[c] Continuum fluxes derived from NextGen (Hauschildt et al. 1999) synthesis models based on our measured T_{eff}s

[d] Masses constrained by eqn. 4.5 assuming inclination angle = 60° and q = 0.7 are in agreement with PMS stellar evolutionary models of Palla & Stahler (1999) using temperatures of best fit synthesis models and assuming $\log g$ = 4.2

tion limit for lunar occultation imaging techniques. Using precision radial velocity measurements, we can detect short period (P $\lesssim$ 200 days) binary systems ($M_{total} \gtrsim$ 0.8 $M_\odot$) in a single epoch at least 80% of the time (see Table 4.2).

4.4.1 GSS29 Two Component Model Fit

The second (primary) component of GSS29 is marginally detected only in the 21 May 2000 epoch where the two components would be well separated spectally near the velocity maximum. In this epoch, the depression of the flux below the continuum at 2.2085 μm must be due to the primary, since there are no other lines in the K band at this wavelength and temperature that could be part of the spectrum of the secondary. The very broad absorption feature here indicates rapid rotation. A 5600K model for the primary with $v\sin\ i$ = 60 km s^{-1} fits this sub–region well, but introduces residual absorption at 2.2062 μm that is not observed.

The absence of absorption at 2.2062 μm is puzzling, where the strongest Si line would be present in the primary. There is a telluric absorption line at this wavelength, but mis–cancellation wouldn't cause an increase in flux over a 5Å span given the intrinsic width of the telluric line ($<$ 20 km s^{-1}). Absorption at 2.2062 μm comes about as the temperature of the primary increases, though hotter models for the primary cause too much ”veiling” in the secondary lines due to an increase in the flux ratio. Temperatures below 5000K for the primary are ruled out since there is no detectable feature where the Si line ought to be.

Veiling and Brγ

GSS29 shows a lack of accretion activity based on the absence of any significant Brγ emission from lower resolution observations of Luhman & Rieke (1999). This is confirmed by our best–fit model of this binary system. The relative depths of the Na and Si lines constrain the temperature of the secondary to < 5000K (Fig. 4.3), independent of continuum veiling. Our best two component model fit for the GSS29 system (Fig. 4.4) suggests that there is no significant veiling due to disk emission. Instead, the flux ratio of 1.6 (see Table 4.4) results in a decrease of equivalent widths in the secondary lines due to additional continuum flux from the hotter primary.

If the primary is warm (5600K = G8V Kenyon & Hartmann 1995), then Brackett γ absorption in the stellar photosphere is starting to get strong in the spectrum (Kleinmann & Hall 1986). But, if the star is rapidly rotating then the presence of this line (at 2.166 μm) is diminished as the feature is broadened. No Br γ absorption was detected in GSS29 by Luhman & Rieke (1999) at a velocity resolution of 250 km s^{-1}. Observations at higher spectral resolution are needed to detect Br γ absorption, and measure the $v \sin i$ broadening.

Near–IR Colors

A consistency check can be made from the observed near–IR colors of GSS29 (Barsony et al. 1997). Using the extinction law of Martin & Whittet (1990) and the intrinsic J–H and H–K colors for a G8 ($T_{\rm eff}$ = 5600K) dwarf (Table A5 of Kenyon & Hartmann 1995), we derive the extinction in the J and K bands, assuming

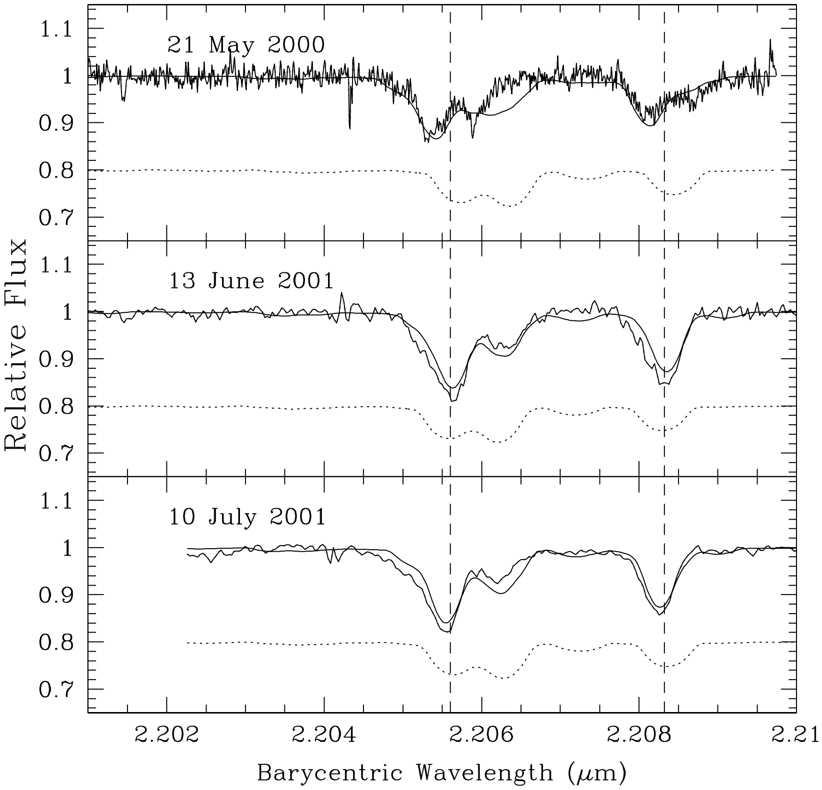

Figure 4.4 Two component synthesis model fits to the PMS spectroscopic binary GSS29. In each of the three epochs the preliminary best fit is plotted along with the observed spectrum (vertical panels). The best–fit primary spectrum is shown below in each panel (dotted line). In all epochs, the spectrum is dominated by absorption lines from the cooler secondary component, modeled by an effective temperature of 4000 K rotating at 40 km s^{-1} ($v\sin i$). The primary component has weaker lines because it is hotter ($T_{\rm eff}$ = 5600 K) and rotating faster ($v\sin i = 60$ km s^{-1}), even though it contributes 70% more flux at 2.2 μm than the secondary. With an assumed gravity of $\log g$ = 4.0, we use the Palla & Stahler PMS evolutionary models to estimate the masses of each component ($M_1 \approx 1.05 M_\odot$, $M_2 \approx 0.7 M_\odot$) to constrain the radial velocity of the primary component at each epoch relative to the systemic velocity (dashed vertical lines) of the cloud.

that significant near–IR continuum excess is confined to the K band only (Luhman & Rieke 1999). Then, by comparing the derived near–IR extinction values (A_J = 3.74, A_K = 1.32) to the observed colors, any excess flux at K would likely be due to non–stellar continuum emission (veiling) from a circumprimary disk. The derived veiling is r_K = 0.06, consistent with the best model fit of r_K = 0 in table 4.4.

Repeating this exercise using intrinsic colors based on just the cooler secondary (T_{eff} = 4000K), gives a veiling value of r_K = 0.15 from the J and K extinction (A_J = 3.06, A_K = 1.08). Since the secondary is 0.6 times as bright as the primary, based on NextGen spectra (Hauschildt et al. 1999) for sources at 4000K and 5600K, the intrinsic near–IR colors will be dominated by the primary star, but influenced by the secondary. Therefore, the derived K band veiling will be slightly more than r_K = 0.06, still consistent with the derived properties of both components listed in Table 4.4.

Luminosity

Using the near–IR photometry from Barsony et al. (1997), the luminosity of GSS29 is computed by correcting for the extinction (calculated above), and using a bolometric correction factor listed in Table A5 of Kenyon & Hartmann (1995). The stellar properties of GSS29 are dominated by the hotter component, since it is the dominant source of luminosity in the system. Based on the photometry, the derived luminosity is 7.2 $L_\odot$, making GSS29 the second most luminous source in our sample (Fig. 4.5). An elevated luminosity would be consistant with GSS29 being a binary system. The large scatter in the derived luminosities in the sources could be partly due to the presence of infrared excess at J that has been assumed to be negligible in the calculation of luminosities in 4.5.

4.5 Summary

We have detected a spectroscopic binary system in our Ophiuchus survey of PMS stars. Through subsequent observations at later epochs, we have measured the period and velocity amplitude of the orbit based on precision radial velocity measurements of the dominant spectral line component. Minimum mass constraints set by the orbit led us to conclude that the dominant spectral line component arises from the cooler and less massive star. The spectrum of the cooler star is modeled by a 4000K photosphere, rotating at 40 km s^{-1}. The spectrum due to the hotter (and brighter) star is modeled and appears nearly featureless because of weak photospheric lines at 5600K that are broadened by rotation. The best fit model has no continuum veiling that would be due to presence of warm dust in a disk.

To set better constraints on the temperature, rate of rotation, and the amount of non–stellar continuum excess in both componets of GSS29, we need to obtain a high resolution spectrum at an epoch where the radial velocities of the components are near their maximum along our line–of–sight.

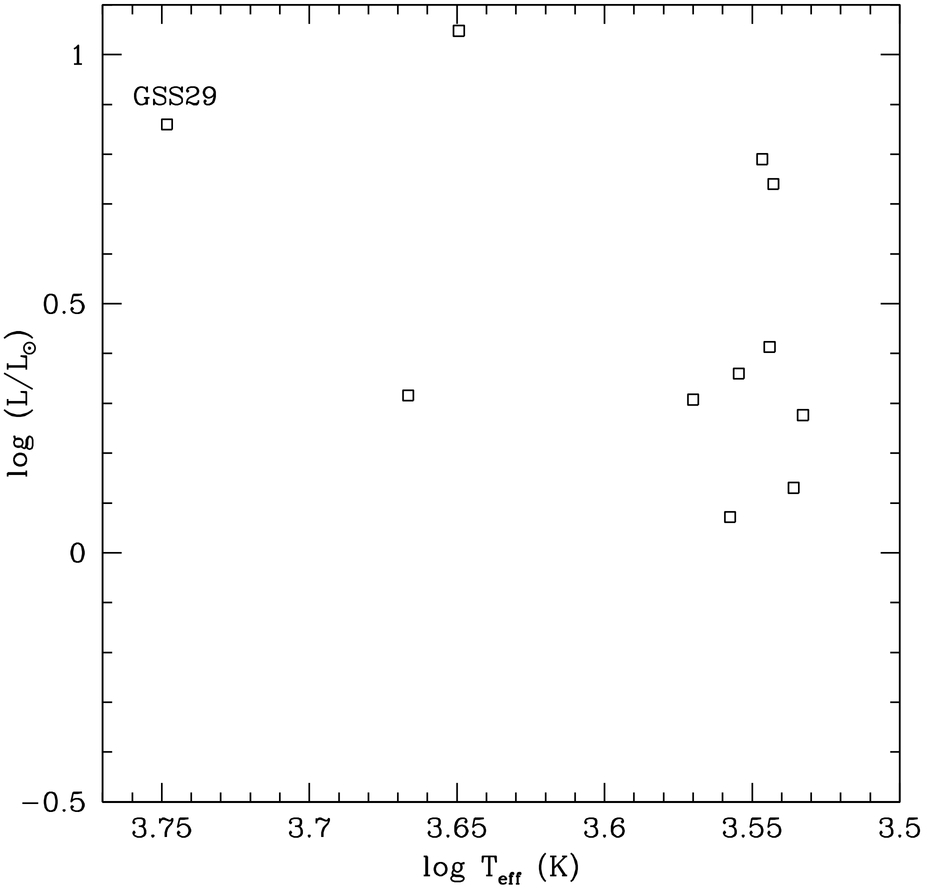

Figure 4.5 The derived luminosities and temperatures of the sources in the ρ Ophiuchi sample are plotted based on near–IR photometry of Barsony et al. (1997) and the best fits to spectral synthesis models. The derived luminosity ($L = 7.24\ L_\odot$) is based on intrinsic colors corresponding to a warm primary estimated at 5600 K from a best two component spectral synthesis model fit. This elevated luminosity compared to the mean of the sample is consistent with the presence of extra flux due to the secondary component.

Appendix A

Surface Gravity Diagnostics

The ratio of photospheric equivalent widths from the Na doublet at 2.2 μm and the (2–0) ^{12}CO bandhead at 2.3 μm is sensitive to changes in surface gravity. Figure 2.5 shows that this sensitivity spans the range in effective temperature and surface gravity relevant to the study of low mass pre–main sequence (PMS) stars. In that figure, the photospheric equivalent widths in both the Na interval and the ^{12}CO interval were calculated from model spectra synthesized from the NextGen stellar atmosphere models for $\log g = 3.5$–5.0 and $T_{\rm eff} = 3000$–5000 K.

The problem in studying YSOs is that they suffer both from significant extinction and reddening and often from the presence of excess continuum emission that can be larger than the emission from the photospheres themselves. As a result, the measured equivalent width ratios do not accurately reflect the ratio of photospheric equivalent widths that would be relevant for comparison with Figure 2.5. What we would like to be able to do is to take the observed equivalent widths and, using as little additional data as possible and in a way as insensitive as possible to the effects of reddening and infrared excess, correct the observed equivalent width ratio to the photospheric equivalent width ratio. We outline here a procedure that uses near–IR photometry to correct for differential reddening between 2.2 μm and

2.3 μm and low resolution spectroscopic data (if necessary) to correct for throughput differences between the high resolution spectra in the Na and ^{12}CO intervals. In both cases, the corrections are usually quite small. In order to utilize this as a diagnostic for surface gravity, the expressions below are geared to observable quantities.

Starting with an absorption spectrum at high resolution, we define the measured equivalent width (MEW) in terms of the flux (F_λ) relative to the continuum (c_λ):

$$\mathrm{MEW} = \int \frac{c_\lambda - F_\lambda}{c_\lambda} \, d\lambda \tag{A.1}$$

We define the photospheric equivalent width (PEW) to be the equivalent width of an photospheric absorption line without its value being altered by the presence of continuum veiling (r_λ=(F_{source}-F_{phot})/F_{phot}) originating from outside of the stellar photosphere. We define, then, photospheric equivalent widths for the regions around the sodium features at 2.2 μm (PEW$_{Na}$) and the shortest wavelength part of the ^{12}CO 2–0 R branch at 2.3 μm (PEW$_{CO}$).

$$\mathrm{PEW_{Na}} = \int_{2.202\mu\mathrm{m}}^{2.212\mu\mathrm{m}} \frac{c_{2.2\mu\mathrm{m}} - F(\lambda)}{c_{2.2\mu\mathrm{m}}} (1 + r_{2.2\mu\mathrm{m}}) \, d\lambda \tag{A.2}$$

$$\mathrm{PEW_{CO}} = \int_{2.2925\mu\mathrm{m}}^{2.3000\mu\mathrm{m}} \frac{c_{2.3\mu\mathrm{m}} - F(\lambda)}{c_{2.3\mu\mathrm{m}}} (1 + r_{2.3\mu\mathrm{m}}) \, d\lambda \tag{A.3}$$

The photospheric continuum p_λ is altered by infrared excess $(1 + r_\lambda)$, probably due to thermal emission from a warm surrounding disk, and extinction (A_λ)

along the line–of–sight. The corresponding expressions for the measured continuum (c_λ) in the two wavelength regions of interest are:

$$c_{2.2\mu\mathrm{m}} = p_{2.2\mu\mathrm{m}}(1+r_{2.2\mu\mathrm{m}})10^{-0.4A_{2.2\mu\mathrm{m}}} \text{ erg s}^{-1}\text{ cm}^{-2}\ \mu\mathrm{m}^{-1} \tag{A.4}$$

$$c_{2.3\mu\mathrm{m}} = p_{2.3\mu\mathrm{m}}(1+r_{2.3\mu\mathrm{m}})10^{-0.4A_{2.3\mu\mathrm{m}}} \text{ erg s}^{-1}\text{ cm}^{-2}\ \mu\mathrm{m}^{-1} \tag{A.5}$$

Knowing the effective temperature (T_{eff}) allows us to relate the photospheric continua to each other by assuming a blackbody dependence ($B(T,\lambda)$). Spectra from the NextGen models that we use closely resemble that of a blackbody.

$$\chi(T_{\mathrm{eff}}) = \frac{p_{2.3\mu\mathrm{m}}}{p_{2.2\mu\mathrm{m}}} = \frac{B(T_{\mathrm{eff}}, 2.3\mu\mathrm{m})}{B_\lambda(T_{\mathrm{eff}}, 2.2\mu\mathrm{m})} \tag{A.6}$$

By taking the ratio of equations A.4 & A.5 and substitutition of equation A.6, we arrive at an expression for a quantity we can measure with low resolution spectra, the ratio of measured continua at two different wavelengths.

$$\frac{c_{2.2\mu\mathrm{m}}}{c_{2.3\mu\mathrm{m}}} = \frac{(1+r_{2.2\mu\mathrm{m}})10^{-0.4A_{2.2\mu\mathrm{m}}}}{\chi(T_{\mathrm{eff}})(1+r_{2.3\mu\mathrm{m}})10^{-0.4A_{2.3\mu\mathrm{m}}}} \tag{A.7}$$

Re–arranging equation A.7 in terms of the infrared excess at 2.3 μm and substituting into the ratio of equations A.2 & A.3 removes the dependence on any infrared excess (veiling):

$$\frac{\mathrm{PEW}_{\mathrm{Na}}}{\mathrm{PEW}_{\mathrm{CO}}} = \frac{\mathrm{MEW}_{\mathrm{Na}}}{\mathrm{MEW}_{\mathrm{CO}}} \frac{c_{2.2\mu\mathrm{m}}}{c_{2.3\mu\mathrm{m}}} \chi(T_{\mathrm{eff}}) 10^{-0.4(A_{2.3\mu\mathrm{m}} - A_{2.2\mu\mathrm{m}})} \tag{A.8}$$

This expression provides terms on the right hand side that we can measure with spectroscopy and photometry allowing us to utilize the surface gravity dependence on photospheric equivalent ratios in models as illustrated in Figure 2.5.

Bibliography

Adams, F. C. & Shu, F. H. 1986, ApJ, 308, 836.

Adams, F.C., Lada, C.J., & Shu, F.H. 1987, ApJ, 312, 788.

Ali, B., Carr, J.S., DePoy, D.L., Frogel, J.A., & Sellgren, K. 1995, AJ, 110, 2415.

Allen, C. W. 2000, *Allen’s Astrophyical Quantities* (New York, Springer-Verlag).

Allen, L. E., Myers, P. C., Di Francesco, J., Mathieu, R., Chen, H., & Young, E. 2002, ApJ, 566, 993.

Alonso, A., Arribas, S., & Martinez-Roger, C. 1996, A&A, 313, 873.

Balachandran, S. & Carr, J. 1994, in 8th Cambridge Workshop on Cool Stars, Stellar Systems and the Sun, Caillaut, J.P. ed. ASP Conf. Ser. 64, 264.

Baldwin, J.R., Frogel, J.A., & Persson, S.E. 1973, ApJ, 184, 427.

Baraffe, I., Chabrier, G., Allard, F., & Hauschildt, P. H. 1998, A&A, 337, 403.

Baraffe, I., Chabrier, G., Allard, F., & Hauschildt, P. H. A&A, astro-ph 0111385.

Barsony, M., Carlstrom, J. E., Burton, M. G., Russell, A. P. G., & Garden, R. 1989, ApJ, 346, L93.

Barsony, M., Kenyon, S.J., Lada, E.A., & Teuben P.J. 1997, ApJS, 112, 109.

Basri, G. & Batalha, C. 1990, ApJ, 363, 654.

Bontemps, S. et al. 2001, A&A, 372, 173.

Bouvier, J., Bertout, C., Benz, W., & Mayor, M. 1986, A&A, 165, 110.

Bouvier, J., Rigaut, F., & Nadeau, D. 1997, A&A, 323, 139.

Calvet, N., Patino, A., Magris, G. C., & D'Alessio, P. 1991, ApJ, 380, 617

Carr, J. S. & Tokunaga, A. T. 1992, ApJ, 393, L67

Carr, J. S., Tokunaga, A. T., Najita, J., Shu, F. H., & Glassgold, A. E. 1993, ApJ, 411, L37.

Carr, J. S. 1989, ApJ, 345, 522.

Casali, M. M. & Eiroa, C. 1996, A&A, 306, 427.

Casali, M. M. & Matthews, H. E. 1992, MNRAS, 258, 399.

Cohen, M. & Kuhi, L. V. 1979, ApJS, 41, 743.

Comeron, F., Rieke, G. H., Burrows, A., & Rieke, M. J. 1993, ApJ, 416, 185.

Covino, E. et al. 2000, A&A, 361, L49.

D'Antona, F. & Mazzitelli, I. 1994, ApJS, 90, 467.

D'Antona, F. & Mazzitelli, I. 1997, Mem. Soc. Astron. Italiana, 68, 823.

de Geus, E. J., Bronfman, L., & Thaddeus, P. 1990, A&A, 231, 137.

de Jager, C. & Nieuwenhuijzen, H. 1987, A&A, 177, 217.

de Medeiros, J. R. & Mayor, M. 1999, VizieR Online Data Catalog, 413, 990433.

de Zeeuw, P. T., Hoogerwerf, R., de Bruijne, J. H. J., Brown, A. G. A., & Blaauw, A. 1999, AJ, 117, 354.

Delfosse, X., Forveille, T., Perrier, C., & Mayor, M. 1998, A&A, 331, 581.

Dent, W. R. F. & Geballe, T. R. 1991, A&A, 252, 775.

Dolidze, M. V. & Arakelyan, M. A. 1959, Soviet Astronomy, 3, 434.

Doppmann, G. W. & Jaffe, D. T. 2002, ApJ, in preparation.

Doppmann, G.W., Jaffe, D.T., White, R.W. 2002, AJ, in preparation.

Duchêne, G., Bouvier, J., & Simon, T. 1999, A&A, 343, 831.

Duquennoy, A. & Mayor, M. 1988, A&A, 200, 135.

Duquennoy, A. & Mayor, M. 1991, A&A, 248, 485.

Edvardsson, B., Andersen, J., Gustafsson, B., Lambert, D. L., Nissen, P. E., & Tomkin, J. 1993, A&A, 275, 101.

Edwards, S. et al. 1993, AJ, 106, 372.

Elias, J. H. 1978, ApJ, 224, 453.

Elias, J. H. 1978, ApJ, 224, 857.

Evans, N. J. 1999, ARA&A, 37, 311.

Fazio, G. G., Low, F. J., Wright, E. L., & Zeilik, M. 1976, ApJ, 206, L165.

Fekel, F.C. 1997, PASP, 109, 514.

Folha, D. F. M. & Emerson, J. P. 1999, A&A, 352, 517.

Ghez, A. M., Neugebauer, G., & Matthews, K. 1993, AJ, 106, 2005.

Ghez, A. M., McCarthy, D. W., Patience, J. L., & Beck, T. L. 1997, ApJ, 481, 378.

Glebocki, R. & Stawikowski, A. 2000, Acta Astronomica, 50, 509.

Goorvitch, D. & Chackerian, C. Jr. 1994, ApJS, 91, 483.

Grasdalen, G. L., Strom, K. M., & Strom, S. E. 1973, ApJ, 184, L53.

Gray, D. F. 1992, The Observation and Analysis of Stellar Photospheres, (New York, Cambridge Univ. Press).

Greene, T. P. & Lada, C. J. 1997, ApJ, 114, 2157.

Greene, T. P. & Lada, C. J. 2000, ApJ, 120, 430.

Greene, T. P. & Meyer, M. R. 1995, ApJ, 450, 233.

Greene, T. P., Tokunaga, A. T., Toomey, D. W., & Carr, J. B. 1993, Proc. SPIE, 1946, 313.

Greene, T. P., Wilking, B. A., Andre, P., Young, E. T., & Lada, C. J. 1994, ApJ, 434, 614.

Greene, T. P. & Lada, C. J. 1996, AJ, 112, 2184.

Greene, T.P., & Young, E.T. 1992, ApJ, 395, 516.

Guilloteau, S. & Dutrey, A. 1998, A&A, 339, 467.

Gullbring, E., Calvet, N., Muzerolle, J., & Hartmann, L. 2000, ApJ, 544, 927.

Haro, G. 1949, AJ, 54, 188.

Hartigan, P., Strom, K. M., & Strom, S. E. 1994, ApJ, 427, 961.

Hartigan, P., Edwards, S., & Ghandour, L. 1995, ApJ, 452, 736.

Hartmann, L., Hewett, R., Stahler, S., & Mathieu, R. D. 1986, ApJ, 309, 275.

Hartmann, L., Cassen, P., & Kenyon, S. J. 1997, ApJ, 475, 770.

Hartmann, L. 1998, *Accretion Processes in Star Formation* (New York, Cambridge University Press).

Hartmann, L. 2001, AJ, 121, 1030.

Hauschildt P. H., Allard, F. & Baron, E. 1999, ApJ, 512, 377.

Hearnshaw, J. B. 1974, A&A, 34, 263.

Hearnshaw, J. B. 1974, A&A, 36, 191.

Henry, T. J. & McCarthy, D. W. 1993, AJ, 106, 773.

Herbig, G. H. & Goodrich, R. W. 1986, ApJ, 309, 294.

Herbig, G. H., Vrba, F. J., & Rydgren, A. E. 1986, AJ, 91, 575.

Herbst, W., Herbst, D. K., Grossman, E. J., & Weinstein, D. 1994, AJ, 108, 1906.

Herbst, W., Rhode, K. L., Hillenbrand, L. A., & Curran, G. 2000, AJ, 119, 261.

Hinkle, K. H., Cuberly, R. W., Gaughan, N. A., Heynssens, J. B., Joyce, R. R., Ridgway, S. T., Schmitt, P., & Simmons, J. E. 1998, Proc. SPIE, 3354, 810.

Johns-Krull, C. M. & Valenti, J. A. 2001, ApJ, 561, 1060.

Johns-Krull, C. M., Valenti, J. A., Piskunov, N. E., Saar, S. H., & Hatzes, A. P. 2001, Magnetic Fields Across the Hertzsprung-Russell Diagram, ASP Conference Proceedings Vol. 248. Edited by G. Mathys, S. K. Solanki, and D. T. Wickramasinghe. ISBN: 1-58381-088-9. San Francisco: Astronomical Society of the Pacific, 2001., p.527, 527.

Johns-Krull, C. M., Valenti, J. A., & Koresko, C. 1999, ApJ, 516, 900.

Keenan, P. C. & McNeil, R. C. 1989, ApJS, 71, 245.

Kenyon, S. J. & Hartmann, L. W. 1990, ApJ, 349, 197.

Kenyon, S. J. & Hartmann, L. 1995, ApJS, 101, 117.

Kenyon, S. J., Brown, D. I., Tout, C. A., & Berlind, P. 1998, ApJ, 115, 2491.

Kirkpatrick, J. D., Henry, T. J., & McCarthy, D. W. 1991, ApJS, 77, 417.

Kirkpatrick, J.D., Kelly, D.M., Rieke, G.H., Liebert, J. Allard, F., & Wehrse, R. 1993, ApJ, 402, 643.

Kleinmann, S. G., & Hall, D. N. B. 1986, ApJS, 62, 501.

Kurucz, R. L. 1992, Rev. Mexicana Astron. Astrofis., 23, 181.

Kurucz, R. L. 1994, Atomic Data for Opacity Calculations, Kurucz CD-ROM No. 1.

Lada, C. J. & Adams, F. C. 1992, ApJ, 393, 278.

Lada, E. A. & Lada, C. J. 1995, AJ, 109, 1682.

Lada, C. J. & Wilking, B. A. 1984, ApJ, 287, 610.

Lada, E. A., Evans, N. J., Depoy, D. L., & Gatley, I. 1991, ApJ, 371, 171.

Lada, C. J. 1999, NATO ASIC Proc. 540: The Origin of Stars and Planetary Systems, 143.

Lancon, A., & Rocca-Volmerange, B. 1992, A&AS, 96, 593.

Lecar, M., Wheeler, J. C., & McKee, C. F. 1976, ApJ, 205, 556.

Leggett, S.K., Allard, F., Berriman, G., Dahn, C.C., and Hauschildt, P.H. 1996, ApJS, 104, 117.

Leinert, C., Zinnecker, H., Weitzel, N., Christou, J., Ridgway, S. T., Jameson, R., Haas, M., & Lenzen, R. 1993, A&A, 278, 129.

Livingston, W. & Wallace L. 1991 An Atlas of the Solar Spectrum in the Infrared from 1850 to 9000 cm-1 (1.1 to 5.4 microns), N.S.O. Technical Report #91-001, July 1991.

Luhman. K. L. & Rieke, G. H. 1998, ApJ, 497, 354.

Luhman. K. L. & Rieke, G. H. 1999, ApJ, 525, 440.

Luhman. K. L., Rieke, G. H., Lada, C. J., & Lada, E. A. 1998, ApJ, 508, 347.

Marsakov, V. A. & Shevelev, Y. G. 1988, Bulletin d'Information du Centre de Donnees Stellaires, 35, 129.

Martin, P. G. & Whittet, D. C. B. 1990,ApJ, 357, 113.

Martin-Pintado, J., Wilson, T. L., Gardner, F. F., & Henkel, C. 1983, A&A, 117, 145.

Mathieu, R. D. & Mazeh, T. 1988, ApJ, 326, 256.

Mathieu, R. D., Walter, F. M., & Myers, P. C. 1989, AJ, 98, 987.

Mathieu, R. D., Ghez, A. M., Jensen, E. L. N., & Simon, M. 2000, in Protostars and Planets IV, ed. V. Mannings, A. P. Boss, & S. S. Russell (Tucson: Univ. Arizona

Mathieu, R. D. 1994, ARA&A, 32, 465.

Mayor, M. & Mermilliod, J. C. 1984, IAU Symp. 105: Observational Tests of the Stellar Evolution Theory, 105, 411.

Mazeh, T., Prato, L., Simon, M., Goldberg, E., Norman, D., & Zucker, S. 2002, ApJ, 564, 1007.

McCaughrean, M. J. 2001, IAU Symposium, 200, 169.

McLean, I. S., Becklin, E. E., Figer, D. F., Larson, S., Liu, T., & Graham, J. 1995, Proc. SPIE, 2475, 350.

McWilliam, A. 1990, ApJS, 74, 1075.

Merrill, K.M., & Ridgway, S.T. 1979, ARA&A, 17, 9.

Meyer, M. R., Calvet, N., & Hillenbrand, L. A. 1997, AJ, 114, 288.

Meyer, M. R., Edwards, S., Hinkle, K. H., & Strom, S. E. 1998, ApJ, 508, 397.

Montmerle, T., Grosso, N., Tsuboi, Y., & Koyama, K. 2000, ApJ, 532, 1097.

Mountain, C.M., Robertson, D.J., Lee, T.J., & Wade, R. 1990, in Instrumentation in Astronomy, Proc. SPIE, p. 25.

Muzerolle, J., Calvet, N., & Hartmann, L. 1998, ApJ, 492, 743.

Najita, J., Carr, J. S., Glassgold, A. E., Shu, F. H., & Tokunaga, A. T. 1996, ApJ, 462, 919.

Padgett, D. L. 1996, ApJ, 471, 847.

Palla, F. & Stahler, S. W. 1999, ApJ, 525, 772.

Palla, F. & Stahler, S. W. 2000, ApJ, 540, 255.

Patience, J., Ghez, A. M., Reid, I. N., Weinberger, A. J., & Matthews, K. 1998, AJ, 115, 1972.

Prato, L., Simon, M., Mazeh, T., McLean, I., Norman, D., & Zucker, S. 2002, ApJin press.

Prato, L. A. 1998, Ph.D. Thesis, 16.

Prosser, C. F., Stauffer, J. R., Hartmann, L., Soderblom, D. R., Jones, B. F., Werner, M. W., & McCaughrean, M. J. 1994, ApJ, 421, 517.

Ramirez, S.V., DePoy, D.L., Frogel, J.A., Sellgren, K., & Blum, R.D. 1997, AJ, 113, 1411.

Richichi, A., Leinert, C., Jameson, R., & Zinnecker, H. 1994, A&A, 287, 145.

Rieke, G. H., Ashok, N. M., & Boyle, R. P. 1989, ApJ, 339, L71.

Shu, F. H., Adams, F. C., & Lizano, S. 1987, ARA&A, 25, 23.

Shu, F., Najita, J., Ostriker, E., Wilkin, F., Ruden, S., & Lizano, S. 1994, ApJ, 429, 781.

Siess, L., Dufour, E., & Forestini, M. 2000, å, 358, 593.

Simon, M. & Prato, L. 1995, ApJ, 450, 824.

Simon, M., Chen, W. P., Howell, R. R., Benson, J. A., & Slowik, D. 1992, ApJ, 384, 212.

Simon, M., Ghez, A. M., & Leinert, C. 1993, ApJ, 408, L33.

Simon, M. et al. 1995, ApJ, 443, 625.

Simon, M., Dutrey, A., & Guilloteau, S. 2000, ApJ, 545, 1034.

Sneden, C. 1973 PhD Thesis, University of Texas at Austin.

Soubiran, C., Katz, D., & Cayrel, R. 1998 A&AS, 133, 221.

Stassun, K. G., Mathieu, R. D., Mazeh, T., & Vrba, F. J. 1999, AJ, 117, 2941.

Steffen, A. T. et al. 2001, AJ, 122, 997.

Strassmeier, K. W. A., Granzer, T., Scheck, M., & Weber, M. 2000, A&AS, 142, 275.

Strom, K. M. & Strom, S. E. 1994, ApJ, 424, 237.

Strom, K. M., Strom, S. E., Kenyon, S. J., & Hartmann, L. 1988, AJ, 95, 534.

Strom, K. M., Strom, S. E., Edwards, S., Cabrit, S., & Skrutskie, M. F. 1989, AJ, 97, 1451.

Strom, K. M., Kepner, J., & Strom, S. E. 1995, ApJ, 438, 813.

Struve, O. & Rudkjøbing, M. 1949, ApJ, 109, 92.

Taylor, B. J. 1995, PASP, 107, 734.

Thompson, R. I. 1985, ApJ, 299, L41.

van Dishoeck, E. F. & de Zeeuw, T. 1984, MNRAS, 206, 383.

Vogt, S. S., Penrod, G. D., & Soderblom, D. R. 1983, ApJ, 269, 250.

Vrba, F. J., Strom, K. M., Strom, S. E., & Grasdalen, G. L. 1975, ApJ, 197, 77.

Wallace, L., & Hinkle, K. 1996, ApJS, 107, 312.

Webb, R. A., Zuckerman, B., Platais, I., Patience, J., White, R. J., Schwartz, M. J., & McCarthy, C. 1999, ApJ, 512, L63.

White, R. J. & Ghez, A. M. 2001, ApJ, 556, 265.

White, R. J., Ghez, A. M., Reid, I. N., & Schultz, G. 1999, ApJ, 520, 811.

Whittet, D. C. B. 1974, MNRAS, 168, 371.

Wilking, B. A., Schwartz, R. D., & Blackwell, J. H. 1987, AJ, 94, 106.

Wilking, B. A., Lada, C. J., & Young, E. T. 1989, ApJ, 340, 823.

Wilking, B. A., Harvey, P. M., & Joy, M. 1984, AJ, 89, 496.

Wilking, B.A., & Lada, C.J. 1983, ApJ, 274, 698.

Wright, G. S., Mountain, C. M., Bridger, A., Daly, P. N., Griffin, J. L., & Ramsay Howat, S. K. 1993, Proc. SPIE, 1946, 547.

Vita

Gregory William Doppmann was born in Cedar Rapids, Iowa on March 24, 1966, the son of Willa S. and William G. Doppmann. Growing up in the Pacific Northwest, he was active in theater throughout Junior High and High School. In 1986 he moved to New York City to pursue a career in the performing arts at New York University. Returning to Washington State 2 years later, he was drawn to the San Juan Islands. Inspired by the starry skies on Orcas Island, he became very interested in astronomy. Lured to Austin by the astronomy program with its observing opportunities for students at McDonald Observatory, he began his studies at the University of Texas in 1990, receiving a Bachelor of Arts in 1994, and a Master of Arts in 1997. He was member of the Adjunct Faculty at Austin Community College in 1998. The following year, he became a doctoral candidate at UT. Upon completion of this Ph.D., he will move to the Bay Area in California to continue research on pre–main sequence stars at NASA Ames Research Center as a National Research Council Associate working with Thomas P. Greene.

Permanent address: 1606-B Linscomb Ave.
Austin, Texas 78704

This dissertation was typeset with LaTeX[†] by the author.

[†] LaTeX is a document preparation system developed by Leslie Lamport as a special version of Donald Knuth's TeX Program.